Hybrid Silicon-Vanadium Dioxide Photonic Devices for Optical Modulation

by

Kevin J. Miller

Dissertation

Submitted to the Faculty of the
Graduate School of Vanderbilt University
in partial fulfillment of the requirements
for the degree of

DOCTOR OF PHILOSOPHY

in

Interdisciplinary Materials Science

May 11, 2018
Nashville, Tennessee

Approved:

Sharon M. Weiss, Ph.D.

Richard F. Haglund, Ph.D.

Daniel M. Fleetwood, Ph.D.

Jason Valentine, Ph.D.

Yaqiong Xu, Ph.D

To my parents and grandparents,

in thanks for and admiration of their work ethic and selflessness.

ACKNOWLEDGMENTS

I would first like to thank my advisor, Professor Sharon Weiss. I am very grateful for your mentorship throughout my time as a PhD student. Thank you for giving me the opportunity to do a research rotation and ultimately join your research group. Thank you for playing an active role in my scientific development and constantly being available and willing to provide research advice. I am also deeply thankful for the additional career development opportunities you have provided, giving me the chance to speak on campus for multiple events and coordinating my visit to Centre College to meet with their professors and give a seminar to their physics and astronomy students. Most importantly, I want to thank you for your willingness to get to know me as a person and inviting me into your home for holiday and group celebrations. I will always be grateful for your mentorship and friendship.

I would also like to thank the other members of my committee: Professor Richard Haglund, Professor Daniel Fleetwood, Professor Jason Valentine, and Professor Yaqiong Xu. Thank you all for your willingness to serve on my committee and provide guidance throughout this process. In particular, thank you Professor Haglund for serving as my co-advisor and for treating me as a member of your own group.

I have had the pleasure of sharing time with many incredible people here at Vanderbilt. It is not possible for me to mention everyone who has impacted my life during these five years, but I highlight a large number here. In particular, I want to thank all members of the Weiss group. Dr. Shuren Hu, Dr. Petr Markov, and Dr. Gilbert Rodriguez, thank you for your mentorship getting me up to speed on simulation, fabrication, and characterization of silicon photonic devices, at both the Center for Nanophase Materials Sciences (CNMS) at Oak Ridge National Laboratory (ORNL) and the Vanderbilt Institute of Nanoscale Science & Engineering (VINSE). Dr. Jeremy

Mares, Dr. Shweta Bhandaru, Dr. Girija Gaur, Dr. Yiliang Zhao, Dr. Kelsey Beavers, Kun Qin, VJ Parsi sreenivas, Balakrishnan Melkote Badrinath, and Suruj Deka, it has been my pleasure work alongside each and every one of you. To the current members of the Weiss group, Josh Fain, Tengfei Cao, Francis Afzal, Sami Halimi, Landen Ryder, and Moinul Haque Choudhury, thank you for your friendship, and continue the good work. Thank you to the two undergraduates, Bradley Bark and Bao Nguyen, who worked alongside me. I am excited to see what the future holds for both of you. To the members of my class of the Interdisciplinary Graduate Program in Materials Science, Keith Share, Dr. Alice Leach, Bradly Baer, and Matt Gerboth, thank you for your friendship, and I wish the best for each of you. To Dr. Robert Marvel and Kent Hallman, thank you for your expertise and help relating to VO_2. To Dr. Roderick Davidson and Dr. William Erwin, thank you for your mentorship during my research rotations. Dr. Stanley Lo and Dr. Chanse Hungerford, thank you for your help with simulations and understanding the fiber coupled setup. I also want to thank Dr. Zack Coppens, Dr. Wei Li, and Zhihua Zhu for their friendship and willingness to discuss research ideas. Outside of the laboratory, Adam Cohn and Keith Share, thank you for two well spent years at 61B. I will always look fondly upon those times. Matt Knowe, Dr. Dhiraj Prasai, Professor Gabriel LeBlanc, Dr. Samantha Sarrett, and Adam Cohn, thank you for some of the best pickup soccer games that will ever be played on Vanderbilt's intramural fields. I owe deep gratitude to members of the Vanderbilt IT team in Featheringill Hall (Andy Richter, Phil VerMeulen, Jared Kupidra, and Jay Hollingsworth) for their help with our servers and computers. I also owe a special thank you to Sarah Ross and Alisha McCord. In addition, thank you Pat Tellinghuisen for your help with outreach projects, both on and off campus.

Thank you to the tool owners and scientists at CNMS and VINSE for providing technical expertise for the fabrication and characterization of the devices presented in this thesis. At CNMS, thank you to Dr. Scott Retterer, Dr. Ivan Kravchenko, Dr. Bernadeta Srijanto, Dayrl Briggs, Kevin Lester, and Dale Hensley. At VINSE, thank you to Dr. Anthony Hmelo, Dr. Benjamin Schmidt, Dr. Bo Choi, Dr. Dmitry Koktysh, Kurt Heinrich, Dr. Alice Leach, and Dr. Bill Martinez.

Thank you Professor Shirvel Stanislaus for your encouragement and mentorship during my time at Valparaiso University. I am very thankful you suggested I change my major to physics, and I am sure you continue to mold the minds of undergraduate students, inspiring with your curiosity and work ethic.

Most importantly, I would like to thank my family. Thank you to my parents, Scott, Becca, and Kevin, for your unending support and love. I am such a proud son, brother, and brother-in-law, and I will always do my best to reciprocate all the support and kindness you have provided throughout my life and during my time here at Vanderbilt. To Sarah, my fiancée, I am the luckiest to have you in my life, and I can't wait for what the future has in store for us. Thank you for your enduring love and support, and let's get some Thai Tom when I get to Seattle.

Lastly, thank you Abby for liking my pumpkin muffins, for when I questioned my value as a Weiss group member, I had to look no further than your smile!

This dissertation is a result of work funded in part by the United States National Science Foundation (ECCS1509740) and the Vanderbilt Institute of Nanoscale Science and Engineering.

TABLE OF CONTENTS

Page

DEDICATION ii

ACKNOWLEDGMENTS iii

LIST OF TABLES ix

LIST OF FIGURES x

1. Introduction 1

1.1 History of optical communication 1

1.2 Silicon photonics 3

1.2.1 Optical modulators 4

1.2.2 Polarization in silicon photonic waveguides 10

1.2.3 Ring resonator theory 11

1.3 Optical phase change materials 13

1.3.1 Vanadium dioxide 14

1.4 Si/VO_2 Photonic Devices 18

1.4.1 Thermo-optic Si/VO_2 photonic devices 19

1.4.2 Electro-optic Si/VO_2 photonic devices 21

1.4.3 All-optical Si/VO_2 photonic devices 25

1.5 Objectives and dissertation overview 26

2. Platforms for Si/VO_2 electro-optic modulation 28

2.1 Introduction 28

2.2 Si/VO_2 electro-optic ring resonator modulator 29

2.2.1 Si/VO_2 ring resonator fabrication 29

2.2.2 Characterization of VO_2 34

2.2.3 Experimental setup 36

2.2.4 Results and discussion 39

2.3 Transverse magnetic mode Si/VO_2 electro-absorption modulator 47

2.4 Conclusions 50

3. Platforms for Si/VO_2 all-optical modulation 52

3.1 Introduction 52

3.2 VO_2 embedded silicon waveguide 52

3.2.2 Device Fabrication 56

3.2.3 Device characterization 60

3.2.4 Experimental setup 62

3.2.5 Results and discussion 65

3.2.6 Considerations of fabrication imperfections 70

3.2.7 Comparison of VO_2 placement location 72

3.2.8 Proposed implementation as all-optical modulator with in-plane excitation 73

3.3 Transverse magnetic mode Si/VO_2 ring resonator 75

3.3.1 Proposed implementation as all-optical modulator with out-of-plane excitation 77

3.4 Conclusions 78

4. Perspectives on Si/VO_2 optical modulators 80

4.1 Introduction 80

4.2 Si/VO_2 electro-optic modulators 80

4.2.2 Si/VO_2 electro-optic modulator embedded design 81

4.3 Si/VO_2 all-optical modulators with in-plane excitation 86

4.3.1 Calculation of energy consumption 87

4.3.2 Comparison to state-of-the-art all-optical modulators 87

4.3.3 Design considerations for polarization independent operation 89

4.4 Conclusions 99

5. Conclusions and future avenues 100
5.1 Conclusions 100
5.2 Future Avenues 101
Appendix 104
A.1 Polarization in fiber-coupled optical setup 104
REFERENCES 111

LIST OF TABLES

Table Page

1. All-optical modulator performance metrics (device footprint, insertion loss, incident switching energy, operation speed, optical bandwidth, and extinction ratio) experimentally measured for modulators in Refs. [23, 35, 36, 81, 82] and theoretically expected for our proposed Si/VO_2 all-optical modulator. 88

LIST OF FIGURES

Figure Page

1.1. (a) Portion of the first telegraphic message sent from Washington D.C. to Baltimore by Samuel F. B. Morse. The full message reads, "What hath God wrought?" Figure adapted from [1]. (b) Global map showing currently active submarine fiber optic cables. Figure taken from [3]. 2

1.2. Examples of (a) refraction-based and (c) absorption-based optical modulators, including their corresponding optical performance in (b) and (d), respectively. (a) Silicon refraction-based ring resonator electro-optic modulator, whereby a resonant feature, shown in (b) can be shifted by modifying *n* to actively control transmission of light through the device. Figures reprinted with permission from [13]. © 2005 NPG. (c) Si/Ge electro-optic modulator, whereby *κ* of Ge, and therefore absorption in Ge, is controlled electrically and determines the optical transmission, presented as extinction ratio in (d) for various applied voltages. Figures reprinted with permission from [12, 14]. © 2010 AIP. © 2012 OSA. 6

1.3. Examples of monolithic (silicon only) electro-optic and all-optical modulators. (a) Optical microscopy image of silicon ring resonator for implementation as an electro-optic modulator. Figure reprinted with permission from [20]. © 2012 IEEE. (b) Scanning electron microscopy (SEM) image of silicon PhC nanocavity for implementation as an all-optical modulator. Figure reprinted with permission from [23]. © 2005 AIP. 8

1.4. Examples of hybrid silicon electro-optic and all-optical modulators. (a) Top view SEM image of a Si/Au plasmonic Mach-Zehnder interferometer electro-optic modulator. Figure reprinted with permission from [24]. © 2015 NPG. (b) Cross-sectional SEM images of Si/polymer slot waveguide used for all-optical modulation. Figure reprinted with permission from [35]. © 2009 NPG. 10

1.5. Electric field intensity profiles for the fundamental TE (a) and TM (b) optical mode. Both field intensity profiles are taken at 1.55 µm for a silicon waveguide geometry of 500 nm (width) × 220 nm (height) using Lumerical Mode Solutions. 11

1.6. (a) Schematic of an all-pass ring resonator. Figure reprinted with permission from [37]. © 2012 Wiley. (b) Example of optical spectrum of ring resonator, showing a distinct resonance and its defining features (resonant wavelength, FWHM, and resonance depth). 12

1.7. (a) Selected transition metal oxide O-PCMs and the temperatures at which they demonstrate a change in their optical properties. Figure reprinted with permission from [40]. © 2011 Annual Reviews. (b) Ternary phase diagram for Te, Ge, and Sb, showing selected chalcogen-based O-PCMs. Figure reprinted with permission from [41]. © 2008 NPG. 14

1.8. Optical properties and atomic structures of VO_2. (a,c) Three-dimensional schematics of the (a) low temperature (T < 68°C), monoclinic and (c) high temperature (T > 68°C), rutile (top right) crystal structures. Vanadium atoms are shown in light blue. The orange shadows highlight

the V-V dimers exhibited in the monoclinic crystal structure. Oxygen atoms are not shown. Figures are adapted and reprinted with permission from [44]. © 2012 APS. The monoclinic and rutile phases of VO_2 are labeled VO_2:M and semiconducting VO_2 and VO_2: R and metallic VO_2, respectively. (b) Optical properties (n and κ) of VO_2. Dashed lines represent the VO_2:M phase (semiconducting VO_2) and solid lines represent the VO_2:R phase (metallic VO_2). Optical properties were taken and repotted from [43]. 16

1.9. (a) Relative change in electron diffraction intensity and IR transmissivity for a VO_2 thin film. The 302 diffraction peak is only allowed in the VO_2:R phase, while the 220 diffraction peak is allowed in both the VO_2:R and VO_2:M phase. The hatched region represents fluences for which no SPT is observed. However, the inset demonstrates for these fluences, there is modulation of the IR optical properties, demonstrating the SMT is taking place. Figure is reprinted with permission from [49]. © 2014 AAAS. (b) Differential transmission (centered at 3.1 μm) of a VO_2 thin film on a-cut sapphire for varying incident pump fluences. Pump wavelength is centered at 825 nm. Differential transmission demonstrates ultrafast (~ 10 ps) recovery dynamics for low fluences. Figure is reprinted with permission from [51]. © 2016 IOP. 17

1.10. (a) Schematic of VO_2 device used for probing electrical dynamics. (b) Current density response of a VO_2 device in response to a voltage pulse, showing 90% of maximum change in conductivity after $\tau = 1.9$ ns. Figures reprinted with permission from [53]. © 2013 IEEE.......... 18

1.11. (a) Schematic and SEM images of VO_2 coated silicon ring resonator. Figure reprinted with permission from [54]. © 2010 OSA. (b) Temperature-dependent transmission of Si/VO_2 ring resonator in (a), demonstrating the change in optical response as VO_2 undergoes its SMT. Data reprinted with permission from [54]. © 2010 OSA. (c) Optical transmission of 1.5 μm radius Si/VO_2 ring resonator (SEM inset top left with VO_2 false colored maroon). At the selected wavelength (dashed line), optical transmission is low with no laser-induced photothermal heating (“laser off” inset) while transmission is high with laser induced photothermal heating (“laser on” inset) due to the resonance shift induced by the SMT. Small scale bar in SEM image inset is 250 nm. Figure and data reprinted with permission from [56]. © 2012 OSA. (d) Proposed 2×2 Si/VO_2 microring switch. Figure reprinted with permission from [57]. © 2016 IEEE. (e) Demonstration of pass polarizer using VO_2 on a designed silicon waveguide (blue). Purple and gray blocks represent VO_2:M and VO_2:R, respectively. TE and TM light are represented by blue and red arrows, respectively. Figure reprinted with permission from [58]. © 2015 OSA. 21

1.12. (a) SEM image of Si/VO_2 electro-optic waveguide device. VO_2 and Au are false colored purple and gold, respectively. Figure reprinted with permission from [52]. © 2015 ACS. (b) Optical microscope image of Si/VO_2 electro-optic waveguide device which delocalizes the optical mode to increase interaction with VO_2:R. Figure reprinted with permission from [59]. © 2015 OSA. 23

1.13. (a) Proposed Si/VO_2 electro-optic modulator design based on directional coupler theory. Figure reprinted with permission from [60]. © 2014 OSA. (b) Proposed Si/VO_2 hybrid plasmonic electro-optic waveguide modulator. Figure reprinted with permission from [61]. © 2015 IEEE. (c) Proposed Si/VO_2 electro-optic design including a vertically embedded VO_2

section within the silicon waveguide. Figure reprinted with permission from [62]. © 2017 IEEE. (d) Proposed Si/Au/VO_2 electro-optic modulator design based on near field plasmonic coupling. Figure reprinted with permission from [63]. © 2015 OSA. 24

1.14. (a) Transient response of Si/VO_2 ring resonator for increasing pump fluence. Fluences range from 0.45-4.74 mJ/cm^2 and are increasing from blue to red. SEM image of Si/VO_2 ring resonator in top right (VO_2 is false colored maroon). Small scale bar in SEM image inset is 250 nm. Figures taken and adopted with permission from [56, 64]. © 2012 OSA, © 2013 OSA. (b) Schematic for proposed Si/Au/VO_2 all-optical modulator. Figure reprinted with permission from [65]. © 2018 IEEE. 26

2.1. Multilayer lithography patterning of Si/VO_2 electro-optic ring resonator modulator. Throughout the figures, Si, SiO_2, VO_2, Cr/Au, and the resist are light gray, dark gray, green, gold, and red, respectively. (a) Patterning and development of resist in preparation of etching of silicon photonic ring resonator. (b) Silicon photonic ring resonator after etching and subsequent liftoff of resist. (c,d) Silicon photonic ring resonator after resist patterning, deposition of VO_2 (c) and Cr/Au (d), and subsequent liftoff of resist. 31

2.2. (a) SEM image of fully fabricated Si/VO_2 ring resonator modulator, including gold contact pads (100 µm × 100 µm) for electrical access. (b) Zoomed-in SEM image to show detail of Si/VO_2 ring resonator. (c) Zoomed-in SEM image showing patterned VO_2 and Au on silicon ring resonator structure. Patterned VO_2 patches are of variable lengths (L_{VO_2}). The VO_2 patch shown in this image has L_{VO_2} = 1 µm. In both images, VO_2 and Au are false colored green and yellow, respectively. 33

2.3. (a) Temperature-dependent reflectometry of a thin film VO_2 witness sample on silicon, demonstrating T_{SMT} ~ 65 °C. (b) Typical IV curve from voltage sweep applied to a Si/VO_2 ring resonator device. Schematic of electrical measurement is shown in inset. The in-series resistor is 3 kΩ for the measurement shown. Discontinuity in current is indicative of the SMT of VO_2. Figures reprinted with permission from [67]. © 2016 SPIE. 35

2.4. Fiber-coupled optical setup for passive characterization of integrated silicon photonic devices. Polarization of tunable laser input from Santec TSL-510 is determined with variable orientation of a linear polarizer and half-wave plate, shown in the bottom right. Optical input is coupled into and out of the device with lensed tapered fibers. This is achieved with visual aid from a live monitor image, using a Mitutoyo M Plan Apo NIR 20X microscope objective. Outcoupling signals are received by a power meter (Newport 2936-C). 37

2.5. Electro-optic experimental setup. (a) Sample holder including a mounted device. For electro-optic characterization, electrical connection to the sample holder was made with electrical cables. Electrical connection to the device was achieved via wire bonding from the electrical strips to the patterend contact pads on the device. (b) Electro-optic sample holder integrated into fiber-coupled, optical setup. Optical input and output coupling are achieved using lensed tapered fibers, and the electrical signal is supplied via connection to the right and left SMA ports of the sample holder. The left port is connected to the electrical supply and the right port is grouded through an in-series resistor. 38

2.6. Thermo-optic experimental setup. (a) Si/VO_2 ring resonator sampled mounted on Physitemp TS-4MP thermal stage, showing optical input and output coupling using lensed tapered fibers. (b) Physitemp PTU-3 pump and tank unit for controlling the sample temperature. Here, the sample temperature is set to 60°C. 39

2.7. (a) Steady-state and (b) high-speed electro-optic measurements for a Si/VO_2 ring resonator device with L_{VO_2} = 3 μm. (c) Steady-state and (d) high-speed electro-optic measurements for a similar device with L_{VO_2} = 1 μm. In (a) and (c), the dashed vertical lines represent the wavelength at which the high-speed measurement was taken in (b) and (d), respectively. The yellow block in (b) and (d) highlights the time duration when the square voltage pulse is on. Figures reprinted with permission from [67]. © 2016 SPIE. 40

2.8. (a) Measured resonance shift as a function of temperature for the L_{VO_2} = 3 μm device presented in Figure 2.7(a,b). (b) Transmission spectra for an additional L_{VO_2} = 3 μm device at various voltages (10 kΩ in-series resistor). (c) Three-dimensional FDTD calculations of the resonance shift of an L_{VO_2} = 3 μm Si/VO_2 ring resonator device where the portion of VO_2 in the VO_2:R phase is varied. (d) Measured resonance shift as a function of I^2 for the L_{VO_2} = 3 μm device presented in (b). Figures reprinted with permission from [67]. © 2016 SPIE. 44

2.9. (a) SEM image of Si/VO_2 ring resonator electro-optic modulator with L_{VO_2} = 3 μm. (b) Zoomed-in SEM image of coupling area, shown in black box in (a), between the bus waveguide and ring resonator, showing the physical coupling connection between the two. The length of this coupling connection is labeled $L_{coupling}$. 46

2.10. (a) Induced optical loss when VO_2 undergoes the SMT for four waveguide geometry/polarization combinations. Inset is a schematic of the simulated device design. Dark gray is SiO_2, light gray is Si, and green is VO_2. (b-e) Electric field intensity cross-sections for varying waveguide geometries, polarizations, and VO_2 phase (VO_2:M or VO_2:R). White and green lines give the outline for the Si/VO_2 structure. VO_2 is represented by the green rectangle, Si is under the VO_2, SiO_2 is the substrate, and air is cladding. 48

2.11. (a) SEM image of fully fabricated Si/VO_2 TM mode electro-absorption waveguide modulator. Si, SiO_2, VO_2, and Au are light gray, dark gray, green (false colored), and gold (false colored), respectively. (b) For TE and TM polarizations, difference in optical transmission with no voltage applied (VO_2:M) and a voltage greater than the switching voltage applied (VO_2:R), plotted as extinction ratio. 49

3.1. Electric field intensity optical mode profiles (Lumerical MODE Solutions) for the TE mode propogating through (a) a silicon waveguide coated with a patch of VO_2 and (b) a waveguide where the guiding material is VO_2. In both cases, VO_2 is outlined in green, and the enhanced interaction with the optical mode for (b) is clearly demonstrated. 53

3.2. (a) Schematic for simulation of VO_2 embedded silicon waveguide shown in gray (silicon) and green (VO_2) on a silicon dioxide (dark gray) substrate. The purple arrow surrounded by the

gray box and yellow box represent the optical source and monitor, respectively. For the fundamental TE mode, (b) simulated transmission as a function of L_{VO_2} through VO_2 embedded silicon waveguide with VO_2 in its semiconducting (blue circles) and metallic (red squares). Optical properties of VO_2 are taken from [43]. (c) Insertion loss and (d) extinction ratio of VO_2 embedded silicon waveguide as a function of L_{VO_2}, calculated from transmission data shown in (b). With the exception of the semiconducting VO_2 curve fit in (b) which is a single exponential fit, the corresponding curve fits in (b), (c), and (d) serve as guides to the eye. Figures reprinted with permission from [74]. © 2017 OSA. 56

3.3. Multilayer lithography patterning of VO_2 embedded silicon waveguide. In each schematic, Si, SiO_2, VO_2, and the resist are light gray, dark gray, green, and red, respectively. (a) Patterning and development of resist in preparation of etching of silicon photonic structure. (b) Silicon waveguide with trench after etching and subsequent liftoff of resist. (c,d) VO_2 embedded silicon waveguide resist patterning and (c) first and (d) second deposition of VO_2, including liftoff of resist after each deposition. 58

3.4. SEM image of bifurcated silicon waveguides (false colored navy) and integrated heaters (false colored gold). In the center of the figure, the small boxes highlight VO_2 embedded silicon waveguides (orange) and control waveguides (light blue). The left inset with orange outline shows an SEM image of the VO_2 embedded silicon waveguide. For clarity, VO_2 is false colored green. The right inset outlined in light blue shows the control silicon waveguide. Figure adapted and reprinted with permission from [74]. © 2017 OSA 59

3.5. SEM image of the integrated resistive heaters. The metallic components are false colored gold. Any gold coloring appearing on the waveguide surfaces is an artifact of the false coloring method used for image processing. The right inset shows a zoomed-in SEM of a unit cell of the integrated heater. The gold wire width, gold wire length, and gap between gold wires are labeled w_{Au}, L_{Au}, and w_{gap}, respectively. The white scale bar in the bottom left of the inset is 20 μm. ... 60

3.6. a) Tilted SEM images of VO_2 embedded silicon waveguides with L_{VO_2} = 300, 600, and 900 nm. VO_2 is shown in false colored green. (b) AFM image of VO_2 embedded silicon waveguide with L_{VO_2} = 1000 nm. Vertical profile of line cut (black line outlined in white) is presented in (c), showing a VO_2 thickness of ~ 180 nm within the trench. (d) Temperature-dependent transmission measurements on a thin film VO_2 witness sample on a glass substrate. The red and blue curves show transmission with increasing and decreasing temperature, respectively. Figures reprinted with permission from [74]. © 2017 OSA. 61

3.7. Fiber-coupled optical setup, including integrated electrical probe station, for active characterization of VO_2 embedded silicon waveguides. (a) Image of entire experimental setup, showing optical input/output, polarization control, and components for electrical probing of photonic devices. (b) Zoomed-in image on the sample, showing optical coupling to and from the pohotonic device via optical fiber in addition to electrical connections from the two electrical probes. (c) Image taken from a monitor reading an image from a Sensors Unlimited SU320M camera through a Mitutoyo M Plan Apo NIR 20X microscope objective. This image shows the left electrical probe just above one of the contact pads of the resistive heaters. The horizontal lines represent the VO_2 embedded silicon waveguides. 64

3.8. (a) Raw (thin lines) and smoothed (thick lines) data for transmitted power through a VO_2 embedded silicon waveguide with L_{VO_2} = 600 nm. Blue curves correspond to 0 W applied electrical power (*i.e.*, VO_2 in semiconducting state) and red curves correspond to 1.41 W applied electrical power (*i.e.*, VO_2 in metallic state). (b) Extinction ratio of same sample for various applied electrical powers, calculated from the smoothed spectra. Figures reprinted with permission from [74]. © 2017 OSA. 66

3.9. Measured transmission through VO_2 embedded silicon waveguide as a function of L_{VO_2}, normalized to transmission through a reference silicon waveguide, for VO_2 in its (a) semiconducting and (b) metallic state. Calculated (c) insertion loss and (d) extinction ratio of VO_2 embedded silicon waveguide as a function of L_{VO_2} based on measured data in (a) and (b). The solid curves present Lumerical simulation results (VO_2 optical properties from [43]) that assume partial VO_2 filling of the silicon trench, as described in Section 3.2.5.1. Figures reprinted with permission from [74]. © 2017 OSA. 68

3.10. (a) Transmission through a VO_2 embedded silicon waveguide with L_{VO_2} = 500 nm in a non-bifurcated device geometry for semiconducting (blue) and metallic (orange) VO_2. (b) Measured extinction ratio corresponding to the data in (a), without any data averaging. 69

3.11. (a) Transmission, absorption, and reflection for VO_2 embedded silicon waveguide with the embedded VO_2 in the semiconducting (blue) and metallic (orange) state as a function of VO_2 thickness. (b,c) Electric field intensity profile of optical mode at the center of the modulator (*i.e.*, cutting through the VO_2 section), considering (b) semiconducting and (c) metallic VO_2 for h_{VO_2} = 40, 100, 160, and 220 nm. The transparent purple section represents the VO_2. (d) Insertion loss and extinction ratio for the Si/VO_2 all-optical modulator as a function of VO_2 thickness. Figures reprinted with permission from [75]. © 2017 SPIE. 71

3.12. Measured extinction ratio for Si/VO_2 waveguides with VO_2 on top of (red data points and upper right SEM image) and embedded within (blue data points and lower right SEM image) the silicon waveguide. Figure adapted and reprinted with permission from [74]. © 2017 OSA. 73

3.13. Schematic of proposed operation of VO_2 embedded silicon waveguide geometry as an all-optical modulator with in-plane excitation. (a) VO_2 embedded silicon waveguide in its passive state, showing transmission of radiation (light blue) through silicon (gray) and semiconducting VO_2 (green). (b) VO_2 embedded silicon waveguide showing optical modulation. Ultrafast pulses (purple) induce the SMT of VO_2, switching the VO_2 to its metallic state (shown in red), resulting in modulation of the incident radiation at the output of the waveguide. 74

3.14. (a) SEM image of 10 μm radius TM mode Si/VO_2 ring resonator. The VO_2 patch (false colored green) is 350 nm long and is shown in the inset. The white scale bar in the inset is 200 nm. (b) Raw data from thermo-optic measurement of resonance in Si/VO_2 ring resonator. (c,d) Thermo-optic measurement of resonance in (c) Si/VO_2 and (d) Si ring resonator with the thermo-optic effect of silicon subtracted out to clearly demonstrate the effect of the SMT of VO_2. 76

3.15. Schematic of proposed operation of TM mode Si/VO_2 ring resonator an all-optical modulator with out-of-plane excitation. (a) For semiconducting VO_2 (shown in green), the input wavelength is resonant and there is no optical transmission. (b) Ultrafast optical pulses (shown in orange) induce the SMT of VO_2, switching the VO_2 to its metallic state (shown in red). This results in modification of the resonant condition, resulting in optical transmission through the device that mimics the sequence of the incident optical pulses. 78

4.1. Multiple lithography steps for proposed Si/VO_2 embedded electro-optic design. Resist, Si, SiO_2, VO_2, and Au are shown in red, light gray, dark gray, purple, and gold. (a-c) First step of lithography, showing (a) resist spun on the silicon substrate, (b) patterning and development of the resist, and (c) etching of rib waveguide and void in the center of the waveguide. (d) Final device structure after two additional lithography steps (resist patterning and deposition of VO_2; resist patterning and deposition of Au). 83

4.2. (a) Perspective view of Si/VO_2 embedded electro-optic modulator design, showing the silicon waveguide width (labeled w_{wg}) which is swept during the simulations. Si, SiO_2, VO_2, and Au are shown in light gray, dark gray, purple, and gold. (b) Extinction ratio as a function of silicon waveguide width from 1500 nm - 1630 nm. (c) Insertion loss and extinction ratio at 1550 nm as a function of w_{wg}. 85

4.3. (a) Electric field intensity mode profiles of the fundamental TE (top) and fundamental TM (bottom) optical modes in a silicon waveguide of dimensions 700 nm (width) × 220 nm (height), generated using Lumerical MODE Solutions. Reduced confinement in the silicon is observed for the fundamental TM mode and is demonstrated in the reduced effective refractive index, n_{eff}. (b) Insertion loss and extinction ratio for both the fundamental TE and TM optical inputs for varying L_{VO_2} [device geometry is shown in Figure 3.2(a)], showing a saturation in extinction ratio for the fundamental TM mode for $L_{VO_2} \geq 100$ nm. 90

4.4. (a) Transmission through Si/VO_2 waveguide for both fundamental TE and TM optical inputs for varying L_{VO_2}, considering both semiconducting VO_2 (blue) and metallic VO_2 (orange). The waveguide dimensions are 700 nm (width) × 220 nm (height). The fundamental TE mode is represented by circles while the fundamental TM mode is represented by squares. Single exponential fits (dashed line for fundamental TE mode; solid line for fundamental TM mode) are shown for both semiconducting VO_2 curves. (b) Electric field intensity mode profiles of the fundamental TE (top) and fundamental TM (bottom) optical modes in a 700 nm (width) × 220 nm (height) waveguide composed entirely of semiconducting VO_2, generated using Lumerical MODE Solutions.. 92

4.5. (a) Schematic of Si/VO_2 waveguide. VO_2, Si, and SiO_2 are green, light gray, and dark gray, respectively. (b,c) Cross sectional electric field intensity profiles of propagating optical mode (Lumerical FDTD Solutions) at different propagation distances in the VO_2 block, for both the fundamental TE (b) and TM (c) modes. 93

4.6. (a) Electric field intensity mode profiles of the fundamental TE (top) and fundamental TM (bottom) optical modes in a silicon waveguide of dimensions 500 nm (width) × 270 nm (height), generated using Lumerical MODE Solutions. (b) Insertion loss and extinction ratio for both the

fundamental TE and TM optical inputs for varying L_{VO_2}. Increasing the n_{eff} of the fundamental TM mode by modifiying the waveguide geometry gives increased extinction ratio, but a saturation for $L_{VO_2} \geq 100$ nm is still observed. 95

4.7. Cross sectional electric field intensity profiles of the fundamental TM optical mode (Lumerical FDTD Solutions) before (a) and 50 nm (b), 100 nm (c), 500 nm (d), 1 µm (e), and 2 µm (f) after interaction with a 100 nm long patch of metallic VO_2. After 2 µm, the fundamental TM mode has returned to its original electric field distribution. 96

4.8. (a,b) Schematics of Si/VO_2 waveguide devices with (a) a single VO_2 embedded block of a given length and (b) multiple 100 nm long embedded VO_2 blocks spaced by 2 µm. VO_2, Si, and SiO_2 are green, light gray, and dark gray, respectively. (c,d) Insertion loss and extinction ratio comparison for waveguide geometries in (a) and (b) for the fundamental (c) TE and (d) TM optical modes. 98

5.1. Proposed Si/VO_2 photonic device with potential implementation as an all-optical transistor, showing an embedded patch of VO_2 within a silicon ring resonator. (a) There is no incident pump on the VO_2 patch, leaving it in the semiconducting state (shown in green), and blue probe light is resonant, giving no transmission through the bus waveguide. (b) Pump light is incident, switching the VO_2 to its metallic state (shown in purple), and the blue probe light is no longer resonant, giving transmission through the bus waveguide. 102

A.1. Image of fiber-coupled optical setup showing components used for polarization control and characterization. 105

A.2. Image showing free-space polarization control using a linear polarizer and half-wave plate. The top right inset shows the full fiber-coupled system, highlighting the region in this image with a blue box. 106

A.3. Image of lensed tapered fiber adjacent to the polarization beam splitter cube. The fiber rotator shown controls the orientation of the fiber and therefore the polarization incident on a photonic sample during measurement. The top left inset shows the full fiber-coupled system, highlighting the region in this image with an orange box. 108

A.4. Images of the fiber-coupled setup with the germanium detector in locations for TE (parallel to the direction of the optical fiber, shown in the left image) and TM (90° to the direction of the optical fiber, shown in the right image) polarizations. TE and TM polarizations are shown in red and yellow, respectively. 110

Chapter 1

1. Introduction

1.1 History of optical communication

In the last two centuries, our civilization has made incredible advances in the ways we send, receive, and process information, putting us in the midst of the Information Age. Specifically considering information transfer, light (optics) has historically played a vital role. Use of fire, reflecting optical signals off mirrors, and more advanced "opto-mechanical" communication systems (*e.g.*, Chappe telegraph system whereby the physical orientation of a shutter on a tower was used to represent a message) were used until the nineteenth century. In the early 1800s, electricity began to gain traction as an effective medium for information transfer. On May 24, 1844, Samuel F. B. Morse sent the first official telegram, a section of which is shown in Figure 1.1(a), from Washington D.C. to Baltimore using his newly invented electric telegraph [1]. In Morse's system, a human operator encoded and decoded messages via electrical currents in a metal wire. Although fairly slow, Morse's system and successful transmission of this brief message laid the foundation for modern telecommunications. Over a century later, Charles Kao initiated a resurgence of optically dominated information transfer with his theoretical work suggesting high purity silica fibers could have relatively low optical attenuation (20 dB km^{-1}) [2]. This, in addition to the development of the laser and erbium doped fiber amplifier, enabled the possibility of sending information over long distances with light via optical fiber in place of electricity via metal wires. In 1988, the first transatlantic optical fiber was laid between the United States and Europe. Since then, hundreds of submarine fiber optic cables have been laid and form the backbone of our modern, Internet-based, global connectivity. Figure 1.1(b) shows a 2018 map of current submarine fiber optic cable systems. While optics has dominated

information transfer over long distances (*i.e.*, several hundreds of kilometers) for more than two decades, more recently, optics is being utilized for increasingly shorter haul communications. Companies like Google, AT&T, and Verizon now offer fiber-to-the-home technology, where the last several kilometers of Internet connection to the home is routed with optical fiber instead of copper wire.

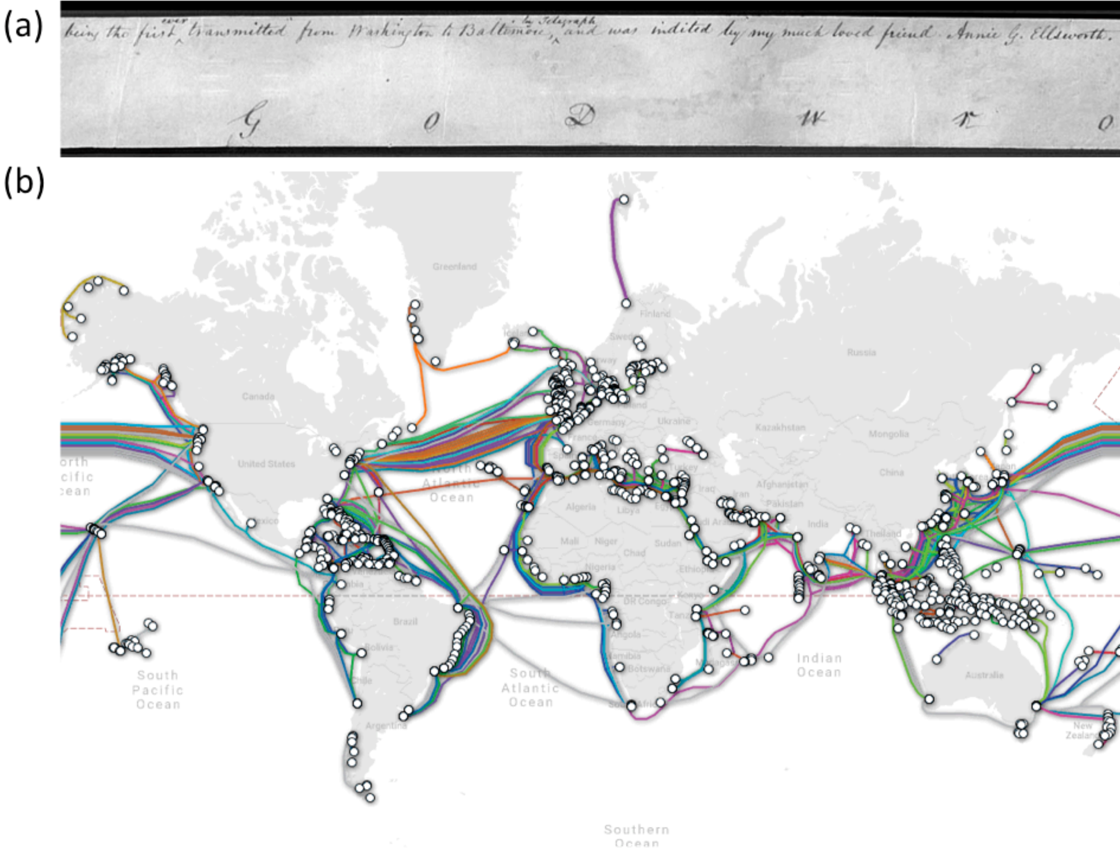

Figure 1.1. (a) Portion of the first telegraphic message sent from Washington D.C. to Baltimore by Samuel F. B. Morse. The full message reads, “What hath God wrought?” Figure adapted from [1]. (b) Global map showing currently active submarine fiber optic cables. Figure taken from [3].

1.2 Silicon photonics

Similar to the previously mentioned long distance applications, the use of light as an information carrier for increasingly short distances is directly related to its information carrying capacity and power consumption metrics compared to electronics. Optical fibers and transceivers are currently being implemented within data centers to send information between individual server racks and server boards, while cutting-edge research efforts focus on integrating optical components between chips (interchip) and within chips (intrachip). Realization of optical data transfer and encoding for both interchip and intrachip applications requires the development of light sources, modulators, detectors, and splitters that meet energy consumption, operation speed, device footprint, and cost requirements [4]. While many architectures for optical information transfer and processing consider hybrid systems with the coexistence of electronic and optical (photonic) components, recently, there has been an emerging discussion of the extent to which photonic technologies can replace their electronic counterparts in entirety for information processing [5] and storage [6, 7]. Realization and implementation of these interchip and intrachip electronic-photonic and all-photonic systems is a non-trivial endeavor and is actively being pursued by a variety of academic and industry teams.

While other material platforms, such as InP, have been used for photonic integrated circuits for fiber-optic communication, silicon photonic components are the most promising option for integration with chip-based systems due to the ubiquity of silicon in the semiconductor electronics industry. However, while silicon provides a platform for low-loss optical transmission in nanoscale silicon waveguides [8], efficient light emission and manipulation have been difficult to achieve due to silicon's indirect band gap and relatively weak electro-optic properties. For these reasons, in addition to monolithic silicon only devices, there is active

research in the area of hybrid silicon-based devices that employ an additional material beyond silicon for their optical functionality. Such hybrid devices are being pursued for silicon-based interchip and intrachip lasing [9], modulation [10], and photodetection [11, 12]. In the following subsections, first, optical modulation, the primary target application of the work comprising this thesis, is described, and then additional details are provided on monolithic and hybrid silicon-based electro-optic and all-optical modulator platforms.

1.2.1 Optical modulators

Modulators are devices that use an external stimulus to manipulate a specific parameter of an information carrier, which in the case of optical modulators is light. The external stimulus can be mechanical, acoustic, thermal, electrical, magnetic, or optical. This thesis focuses on electo-optic (*i.e.*, electrical stimulus) and all-optical (*i.e.*, optical stimulus) modulators, which are best suited to meet the speed requirements of interchip and intrachip optical communications. In order to modulate the amplitude or phase of light, modification of the real, imaginary, linear, and non-linear components of the complex refractive index of material through which the light propagates must be performed. To first order, the complex refractive index is given by:

$$\tilde{n} = n + i\kappa \quad (1)$$

where n (termed refractive index) and κ (often termed extinction coefficient) are the real and imaginary components of the complex refractive index. Modulators that rely primarily on changes in n are termed refraction-based modulators while modulators that rely primarily on changes in κ are termed absorption-based modulators. Figure 1.2 shows examples of both refraction-based and absorption-based modulators. Figure 1.2(a) shows a schematic of a refraction-based modulator, in this case a ring resonator (a photonic device structure discussed in

Section 1.2.3), which demonstrates a resonant feature, shown as a decrease in optical transmission in Figure 1.2(b). By changing n of the modulator, the resonant feature is shifted, leading to a change in transmission intensity at both the former and new wavelengths of the resonant feature. Operation at either of these wavelengths provides the optical modulation. For the case of an absorption-based modulator, κ is directly proportional to the absorption coefficient (α) in the material and can therefore be tuned to control transmission through the modulator. Generally, the change in κ is a broadband effect, so absorption-based modulators typically exhibit broadband operation. A schematic of an example electro-absorption modulator is shown in Figure 1.2(c) where germanium (Ge) is integrated on a silicon waveguide. In this example, broadband transmission through the device is controlled by actively changing the absorption in Ge via application of an electrical voltage. Figure 1.2(d) shows the extinction ratio, which is a measure of the change in optical transmission, for this Si/Ge modulator, demonstrating its modulation performance over a broadband wavelength range.

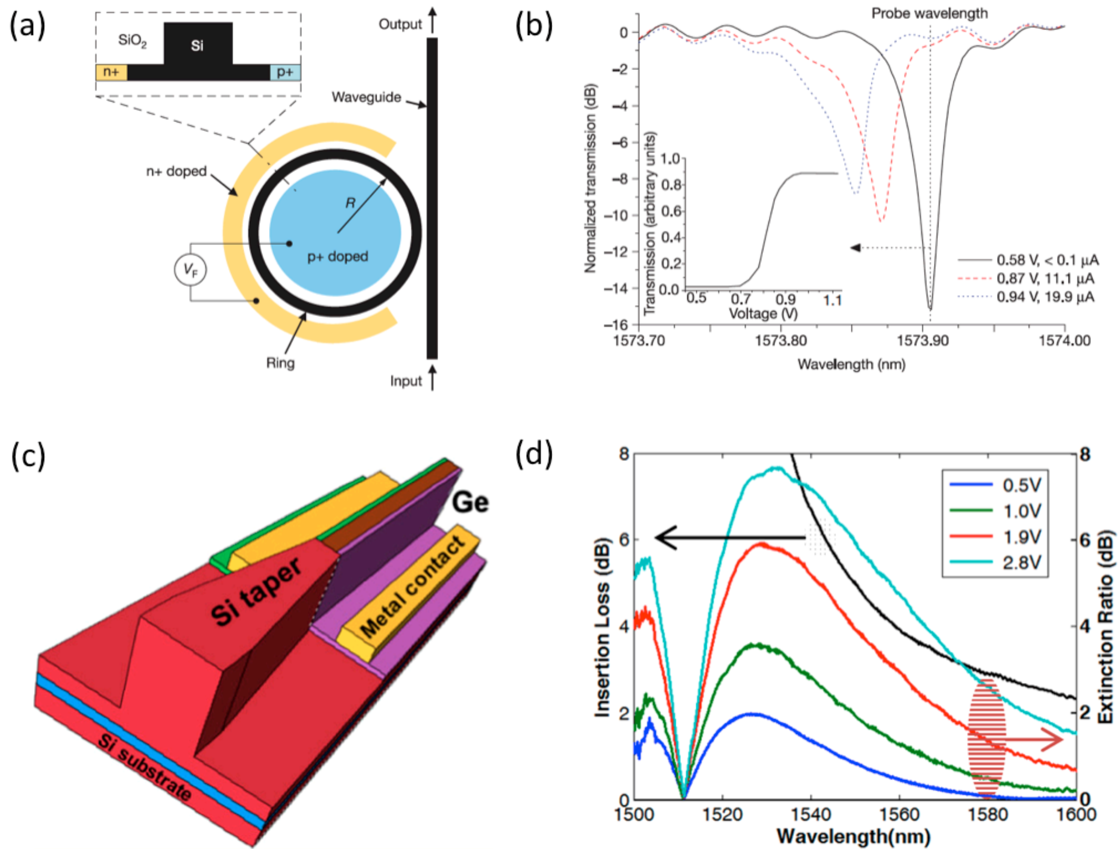

Figure 1.2. Examples of (a) refraction-based and (c) absorption-based optical modulators, including their corresponding optical performance in (b) and (d), respectively. (a) Silicon refraction-based ring resonator electro-optic modulator, whereby a resonant feature, shown in (b) can be shifted by modifying n to actively control transmission of light through the device. Figures reprinted with permission from [13]. © 2005 NPG. (c) Si/Ge electro-optic modulator, whereby κ of Ge, and therefore absorption in Ge, is controlled electrically and determines the optical transmission, presented as extinction ratio in (d) for various applied voltages. Figures reprinted with permission from [12, 14]. © 2010 AIP. © 2012 OSA.

When designing and fabricating an optical modulator, optimization of certain performance metrics must be taken into consideration. These metrics include modulation speed, extinction ratio (or modulation depth), optical bandwidth, insertion loss, device footprint, and energy/power consumption (or operating voltage) [10]. Modulation speed relates to how fast light can be manipulated to encode data. Extinction ratio, often reported in units of dB, is the ratio between

the maximum and minimum transmission of the modulator. Optical bandwidth determines the wavelength range for which the modulator functions. Insertion loss, device footprint, and energy/power consumption are measures of the amount of signal that is lost by adding the modulator into a given optical path, the physical size of the modulator, and the total energy/power necessary to operate the modulator, respectively. The optimal modulator will simultaneously maximize modulation speed, extinction ratio, and optical bandwidth while minimizing insertion loss, device footprint, and energy consumption. However, in practice, achieving all of these goals often proves to be difficult. For example, a modulator that utilizes a resonator geometry is able to minimize device footprint, but this comes at a cost to its optical bandwidth, as is shown in Figure 1.2(b) for the ring resonator modulator.

1.2.1.1 Monolithic silicon optical modulators

Both electro-optic and all-optical modulators have been realized in silicon-only nanophotonic structures. In an effort to overcome silicon's weak refractive index response to free carrier concentration [15], these structures have primarily utilized compact resonant geometries such as ring resonators or large footprint (generally, millimeter scale) non-resonant geometries such as Mach Zehnder interferometers (MZIs). In the early 2000s, electro-optic silicon ring resonator [13] and MZI modulator [16] designs showed the first Gb/s operation, and efforts have continued to improve device performance. The first demonstration of a silicon-only all-optical modulator was also shown in the early 2000s in a 5 μm radius ring resonator, exhibiting ~ 12 dB extinction in < 500 ns at an operation energy of 25 pJ. For silicon electro-optic modulators, modulation speed performance improvement has been primarily due to operation using carrier depletion [17], which is intrinsically faster than carrier injection. For example, for both ring resonators and

MZI geometries, > 30 Gb/s operation has been demonstrated [18-20]. Figure 1.3(a) shows an all-silicon electro-optic 10 μm radius ring resonator from which showed operation at 44 Gb/s at an operating voltage of 3 V [20]. Improvements with respect to device footprint and operating voltage have also been demonstrated. For example, by using a photonic crystal (PhC) waveguide, the device length of an MZI was reduced to 80 μm [21], and in a ring resonator geometry, low voltage operation of 0.5 V was demonstrated [22]. Regarding all-silicon, all-optical modulators, performance improvements have relied on enhancement of nonlinear processes in high Q/V photonic structures. For example, an all-silicon PhC nanocavity, shown in Figure 1.3(b), operating via two photon absorption (TPA), achieved all-optical ~ 10 dB extinction at a speed of 50 ps and energy consumption of 100 fJ [23].

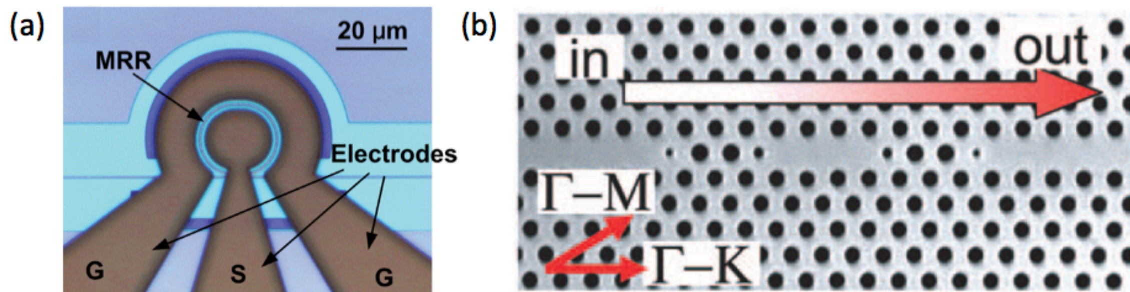

Figure 1.3. Examples of monolithic (silicon only) electro-optic and all-optical modulators. (a) Optical microscopy image of silicon ring resonator for implementation as an electro-optic modulator. Figure reprinted with permission from [20]. © 2012 IEEE. (b) Scanning electron microscopy (SEM) image of silicon PhC nanocavity for implementation as an all-optical modulator. Figure reprinted with permission from [23]. © 2005 AIP.

1.2.1.2 Hybrid silicon optical modulators

In an effort to further improve the performance metrics of silicon-based electro-optic and all-optical modulators, additional active materials have been incorporated into the silicon photonic

platform. This hybrid integration approach allows for the continued use of the silicon platform for guiding light while utilizing a second material whose optical properties and carrier dynamics are superior to those of silicon. In particular, many hybrid silicon optical modulators are being investigated for their potential to increase modulation speed, reduce power consumption, and/or reduce device footprint. Implementation of a plasmonic/silicon hybrid structure, shown in Figure 1.4(a), within an MZI geometry, reduced the device footprint (10 μm × 1 μm) and showed improved operation speed of > 70 GHz at 3 V, but this was demonstrated at a relatively high insertion loss of 8 dB [24]. Integration of nonlinear polymers has demonstrated speeds up to 100 GHz [25], but these modulators still generally require large device footprints [26, 27]. Additional hybrid platforms that have recently received significant interest include the use of Ge [14, 28, 29] and graphene [30-34]. Integration of Ge has demonstrated promise for low-power, high-speed, large extinction operation in relatively small device footprints, but Ge/Si devices often exhibit relatively high absorption losses due to direct bandgap absorption in Ge. Of the modulators that integrate graphene, the most promising are likely from Ref. [30] and Ref. [31], whereby 5.9 GHz operation at a drive voltage of 2.5 V in a 50 μm x 10 μm linear geometry [30] and 30 GHz operation in a ring resonator geometry [31] were shown. However, in both cases, the modulation speed was not superior to silicon-only modulators and for the ring resonator geometry, operation was shown with a relatively large operation voltage of 7.5 V. Additionally, there has been interesting work integrating transparent conducting oxides (*e.g.* indium tin oxide) for use in silicon electro-optic modulators, but to date, high-speed operation has not been shown [33]. For all-optical modulators, integration of nonlinear polymers within silicon waveguides has resulted in faster signal processing, up to 170.8 Gb/s [35]. A cross section of this device is shown in Figure 1.4(b). However, this was in a device of length 4 mm. With the exception of this

demonstration, there has been little work for hybrid integration of silicon-based on-chip geometries. To date, the most successful route to improving performance metrics has been to replace the silicon PhC structure in Ref. [23] with InGaAsP, utilizing its strong carrier induced nonlinearity [36]. This geometry demonstrated 10 dB, 0.66 fJ modulation at approximately 30 ps. However, this is incompatible with silicon processing.

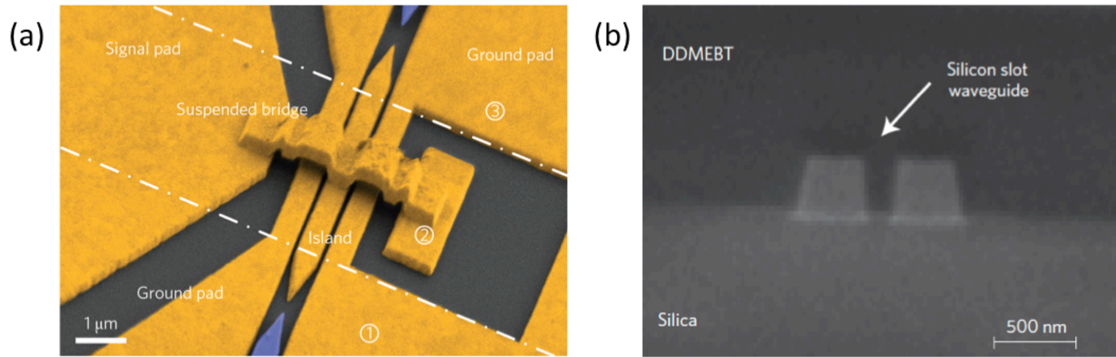

Figure 1.4. Examples of hybrid silicon electro-optic and all-optical modulators. (a) Top view SEM image of a Si/Au plasmonic Mach-Zehnder interferometer electro-optic modulator. Figure reprinted with permission from [24]. © 2015 NPG. (b) Cross-sectional SEM images of Si/polymer slot waveguide used for all-optical modulation. Figure reprinted with permission from [35]. © 2009 NPG.

1.2.2 Polarization in silicon photonic waveguides

Throughout this thesis, device operation for both transverse electric (TE) and transverse magnetic (TM) optical modes will be discussed. Optical modes for which the electric field is primarily oscillating parallel to the top surface of the waveguide are considered to have TE polarization, while optical modes for which the electric field is primarily oscillating orthogonal to the top surface of the waveguide are considered to have TM polarization. Figure 1.5 presents the electric field intensity profiles at a wavelength of 1.55 μm for both the fundamental TE (a) and TM (b) modes, respectively, for a silicon waveguide of cross-sectional dimensions 500 nm

(width) × 220 nm (height). The importance of polarization selection on the performance of optical modulators is discussed in more detail in subsequent sections of the thesis where applicable.

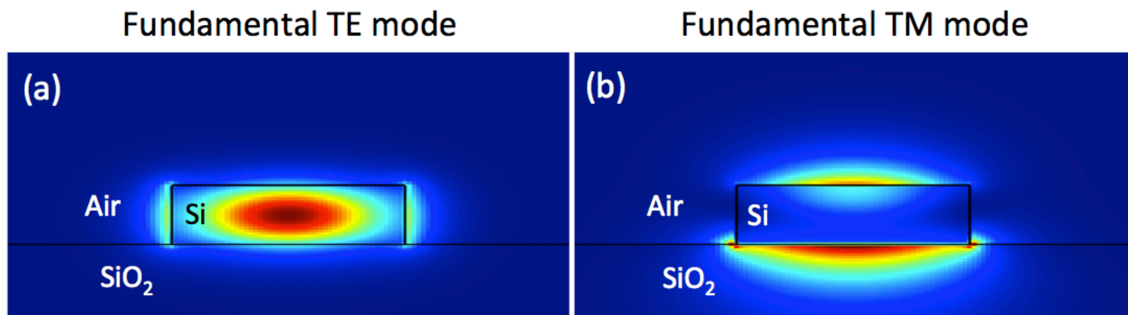

Figure 1.5. Electric field intensity profiles for the fundamental TE (a) and TM (b) optical mode. Both field intensity profiles are taken at 1.55 μm for a silicon waveguide geometry of 500 nm (width) × 220 nm (height) using Lumerical Mode Solutions.

1.2.3 Ring resonator theory

With guidance from Ref. [37], this section provides a brief theoretical background to silicon ring resonators, as they will be discussed throughout the thesis.

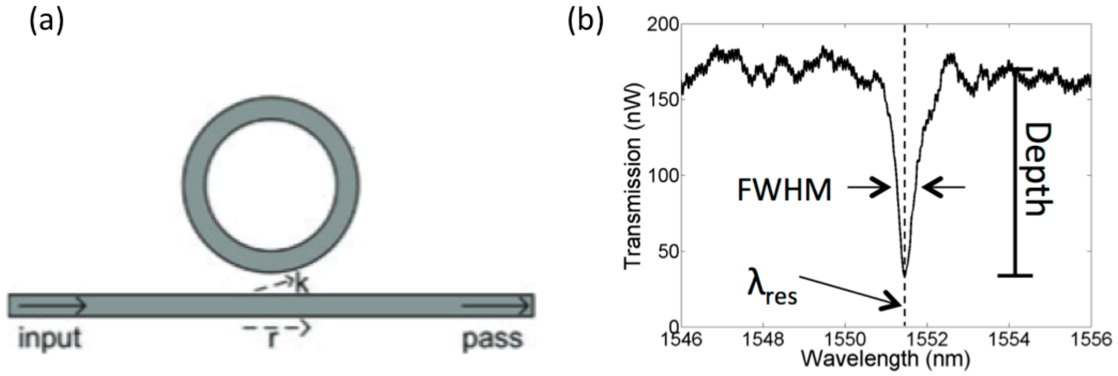

Figure 1.6. (a) Schematic of an all-pass ring resonator. Figure reprinted with permission from [37]. © 2012 Wiley. (b) Example of optical spectrum of ring resonator, showing a distinct resonance and its defining features (resonant wavelength, FWHM, and resonance depth).

The all-pass ring resonator, shown in Figure 1.6(a) along with a corresponding typical spectra in Figure 1.6(b), is the ring resonator geometry used in this work and consists of a linear bus waveguide and a circular ring waveguide. Radiation is coupled into the bus waveguide at the input. This radiation evanescently interacts with the adjacent circular waveguide. For radiation that couples into the resonator, wavelengths that constructively interfere are considered resonant. Resonant wavelengths, λ_{res}, are given by:

$$\lambda_{res} = \frac{n_{eff}L}{m} \tag{2}$$

where n_{eff} is the effective refractive index, L is the geometric path length, and m is a positive integer. Therefore, the resonance wavelength is defined by the geometry of the ring and the refractive indices (n) of the materials composing the ring. The quality factor (Q) describes the width of the resonance and is directly proportional to the lifetime of a photon (τ_{ph}) in the resonator. Q is given by:

$$Q = \frac{\lambda_{res}}{FWHM} = 2\pi v \tau_{ph} \quad (3)$$

where *FWHM* is the full width half maximum of the resonance, v is the optical frequency, and t_{ph} is the photon lifetime in the cavity. Therefore, the width of the resonance provides information about losses in the resonator, induced either by waveguide geometry (*e.g.*, bending losses, scattering due to side wall imperfections) or the extinction coefficients (κ) of the materials composing the ring. The depth of the resonance (often given in units of dB) is dependent upon the coupling condition between the bus and ring waveguides (*i.e.*, light coupling from the bus waveguide to the ring waveguide, and vice versa) and material absorption loss. Therefore, inducing losses in the ring will modify the coupling condition, and as a result, the depth of the resonance. Consequently, the distance between the bus and ring waveguides, waveguide geometry (*e.g.*, bending losses, scattering due to side wall imperfections), and κ of the materials composing the ring dictate the resonance depth.

1.3 Optical phase change materials

Optical phase change materials (O-PCMs) have emerged as a unique class of materials that demonstrate large changes in their optical properties ($\Delta n > 1$, $\Delta\kappa \sim$ order of magnitude) in response to an external stimulus (*e.g.*, temperature, applied voltage, ultrafast optical excitation). These materials generally fall within classification as transition metal oxides or chalcogen-based alloys. Transition metal oxide O-PCMs, some of which are shown in Figure 1.7(a), generally undergo crystalline-crystalline transitions while chalcogen-based O-PCMs, shown in Figure 1.7(b), undergo amorphous-crystalline transitions. There has been and continues to be extensive work investigating the nature of these transitions. For detailed theoretical analysis of these transitions, the reader is referred to [38] and [39] for transition metal oxide and chalcogen-based

O-PCMs, respectively. This thesis focuses on the utilization of the unique properties of a transition metal oxide O-PCM, vanadium dioxide (VO_2), within silicon photonic devices for optical modulation applications. Details of VO_2 are presented in the following subsection.

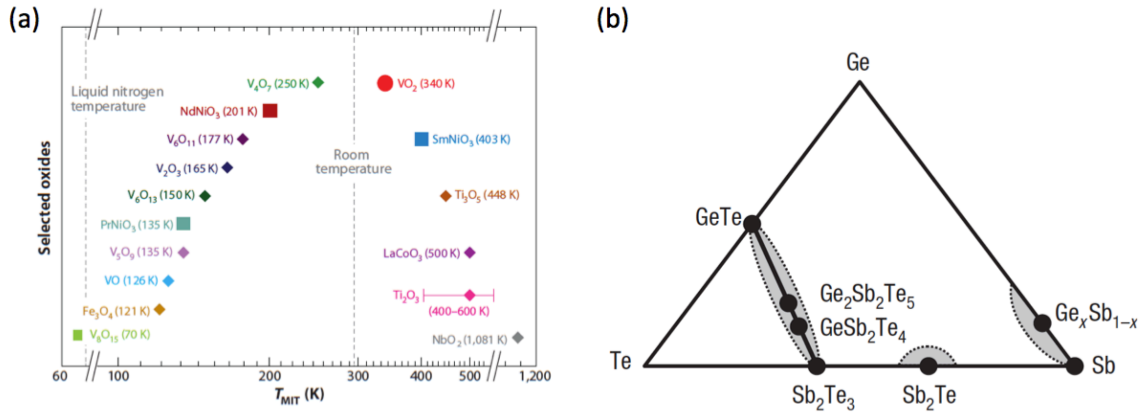

Figure 1.7. (a) Selected transition metal oxide O-PCMs and the temperatures at which they demonstrate a change in their optical properties. Figure reprinted with permission from [40]. © 2011 Annual Reviews. (b) Ternary phase diagram for Te, Ge, and Sb, showing selected chalcogen-based O-PCMs. Figure reprinted with permission from [41]. © 2008 NPG.

1.3.1 Vanadium dioxide

In 1959, F. J. Morin demonstrated a discontinuity in electrical conductivity of approximately three orders of magnitude in VO_2 single crystals near 340 K [42]. In subsequent work, substantive changes in the optical properties of VO_2 (at 1550 nm, n and κ go from 3.3 and 0.3 to 1.8 and 3.3, respectively) [43] were shown. A breadth of research has elucidated some of the fundamental physics responsible for these interesting properties, pointing to the existence of a structural phase transition (SPT) from a low temperature, semiconducting, monoclinic (VO_2:M) phase to a high temperature, metallic, rutile (VO_2:R) phase. The VO_2:R phase is achieved via

breaking of the V-V dimers exhibited in the VO_2:M phase and the straightening of the V atoms along the c axis, shrinking the unit cell twofold.

Figure 1.8 shows the crystal structures of the VO_2:M and VO_2:R phases in addition to the optical properties of VO_2 in both phases from 1450 – 1600 nm. Throughout the body of the text, VO_2:M and VO_2:R are used interchangeably with semiconducting and metallic VO_2, respectively, to refer to the optical properties exhibited in the two phases of VO_2. In addition, transitions from the optically transmissive, electrically resistive VO_2:M phase to the optically opaque, electrically conductive VO_2:R phase and from the optically opaque, electrically conductive VO_2:R phase to the optically transmissive, electrically resistive VO_2:M phase are labeled as the semiconductor-metal transition (SMT) and metal-semiconductor transition (MST), respectively.

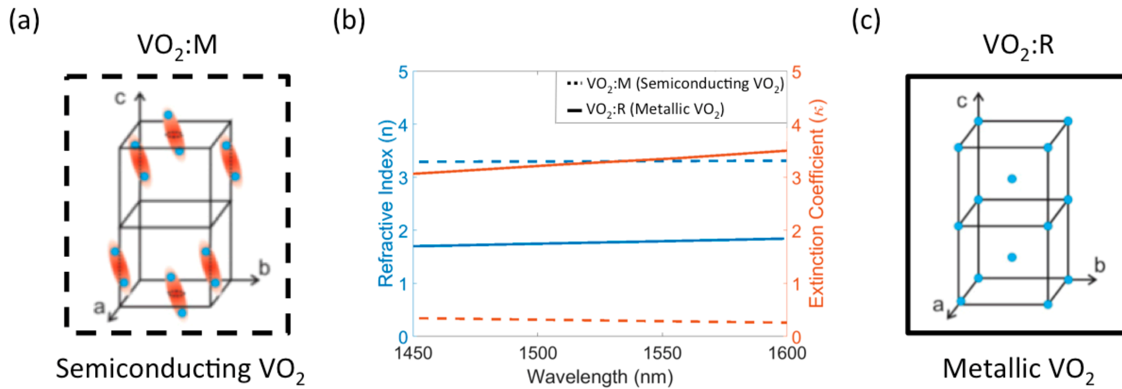

Figure 1.8. Optical properties and atomic structures of VO_2. (a,c) Three-dimensional schematics of the (a) low temperature (T < 68°C), monoclinic and (c) high temperature (T > 68°C), rutile (top right) crystal structures. Vanadium atoms are shown in light blue. The orange shadows highlight the V-V dimers exhibited in the monoclinic crystal structure. Oxygen atoms are not shown. Figures are adapted and reprinted with permission from [44]. © 2012 APS. The monoclinic and rutile phases of VO_2 are labeled VO_2:M and semiconducting VO_2 and VO_2: R and metallic VO_2, respectively. (b) Optical properties (n and κ) of VO_2. Dashed lines represent the VO_2:M phase (semiconducting VO_2) and solid lines represent the VO_2:R phase (metallic VO_2). Optical properties were taken and repotted from [43].

For optical modulation applications, the focus of this thesis, the dynamic change of the optical properties of VO_2 is of the most importance. Recently, numerous ultrafast optical studies on VO_2 thin films have revealed unique ultrafast dynamics [44-51]. These studies, of which some explore the decoupling of atomic structural changes and the change in optical properties, demonstrate the change in optical properties of VO_2 can be accessed on ~ femtosecond ("on") and ~ 1-10 picosecond ("off") times. Two examples of optically induced ultrafast dynamics are shown in Figure 1.9. In Ref. [49], the authors clearly demonstrate the decoupling of the optical properties and the SPT. Shown in Figure 1.9(a), for incident fluences below ~ 9 mJ/cm^2, electron diffraction reveals no atomic structural change. However, the inset clearly demonstrates changes in IR transmissivity for fluences below 9 mJ/cm^2, showing MST times on the order of a

picosecond for the lowest fluences. Although the atomic structure is not transiently monitored, similar optical behavior (~ 10 ps MST times) is observed for low fluences in Ref. [51], shown in Figure 1.9(b).

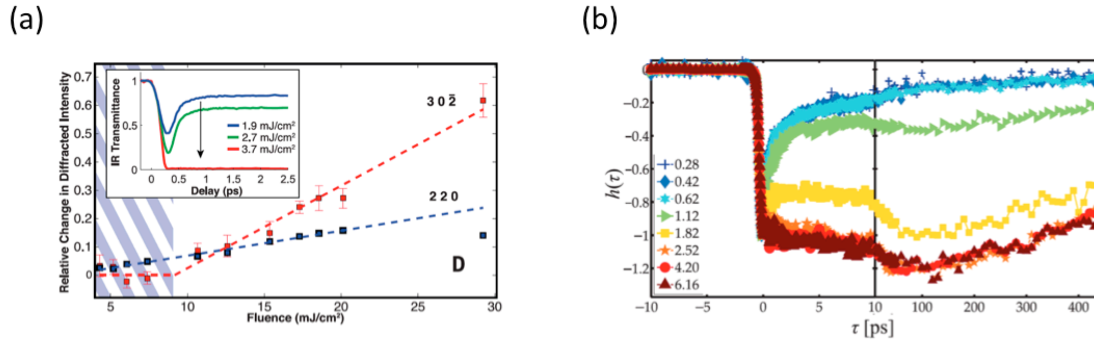

Figure 1.9. (a) Relative change in electron diffraction intensity and IR transmissivity for a VO_2 thin film. The 302 diffraction peak is only allowed in the VO_2:R phase, while the 220 diffraction peak is allowed in both the VO_2:R and VO_2:M phase. The hatched region represents fluences for which no SPT is observed. However, the inset demonstrates for these fluences, there is modulation of the IR optical properties, demonstrating the SMT is taking place. Figure is reprinted with permission from [49]. © 2014 AAAS. (b) Differential transmission (centered at 3.1 μm) of a VO_2 thin film on a-cut sapphire for varying incident pump fluences. Pump wavelength is centered at 825 nm. Differential transmission demonstrates ultrafast (~ 10 ps) recovery dynamics for low fluences. Figure is reprinted with permission from [51]. © 2016 IOP.

While these ultrafast dynamics have been demonstrated for all-optical excitation, the ultimate temporal dynamics in response to an electrical pulse remain to be determined. However, in purely electrical measurements, the SMT and MST transitions have been shown to be no more than 2 [52, 53] and 3 ns [52]. Specifically for the SMT, in Ref. [53], the authors perform electrical measurements through a 400 nm film of VO_2. The device geometry is shown in Figure 1.10(a). In their measurements, the switching time (τ) is defined as the time it takes for the VO_2 to change its electrical resistivity by 90% in log scale and is measured to be ~ 1.9 ns, shown in Figure 1.10(b). Assuming the change in optical properties occurs simultaneously with the change

in electrical conductivity, this suggests electrically induced optical changes in VO_2 can occur on similar time scales. It is expected operation in this regime of fractional optical and electrical (here, 90%) change in VO_2 will provide a faster pathway to the VO_2:M phase, giving faster MST times in device geometries. In addition, as seen in Figure 1.10(b), in the electrical measurement, the current density appears to increase linearly from the start of the voltage pulse until τ, demonstrating that the SMT, although of a lesser magnitude (measured by electrical conductivity), is taking place on time scales faster than 1.9 ns. This suggests even faster device operation, albeit with potentially reduced optical properties, can be potentially be achieved.

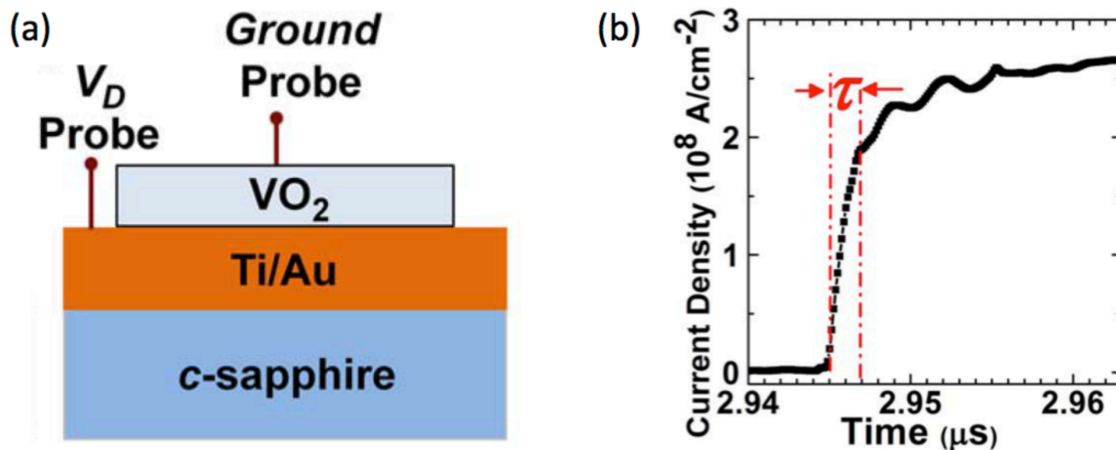

Figure 1.10. (a) Schematic of VO_2 device used for probing electrical dynamics. (b) Current density response of a VO_2 device in response to a voltage pulse, showing 90% of maximum change in conductivity after τ = 1.9 ns. Figures reprinted with permission from [53]. © 2013 IEEE.

1.4 Si/VO_2 Photonic Devices

Due to its unique optical properties and intrinsically ultrafast dynamics presented in Section 1.3.1, VO_2 has been both proposed and realized in a variety of silicon-based photonic devices. In

this section, resonant and non-resonant silicon photonic devices, both in simulation and experiment, which utilize integration of VO_2 for their active functionality, are presented. An emphasis is placed on Si/VO_2 device platforms with potential implementation as electro-optic or all-optical modulators. The presented devices are classified by the mechanism (thermal, electrical, or optical) used to induce the SMT. Devices using continuous wave photothermal heating are classified under thermo-optic functionality (Section 1.4.1) while those which use optical pulses to induce the SMT are classified under all-optical functionality (Section 1.4.3). Devices which use resistive heating through the VO_2 are classified under electro-optic functionality (Section 1.4.2). Simulation based devices are categorized under what is deemed to be the most plausible experimentally realized mechanism to actuate the SMT.

1.4.1 Thermo-optic Si/VO_2 photonic devices

Due to the relatively low temperature (~ 68°C) required to initiate the SMT, active tunability of hybrid Si/VO_2 waveguide and resonant based devices has been experimentally demonstrated through thermal mechanisms including external substrate heating [54, 55] and photothermal heating [56]. In Ref. [54], the authors integrated a 2 μm long VO_2 patch on a 400 μm diameter silicon ring resonator [Figure 1.11(a)]. Using an external substrate heater, the temperature dependent optical response was measured [Figure 1.11(b)] and used to extract the induced absorptive optical loss resulting from the SMT. Specifically, for a 2 μm long, 65 nm thick VO_2 patch atop a linear rib waveguide, the authors calculate induced losses of 2 and 9 dB when VO_2 is in its VO_2:M and VO_2:R phases, giving expected insertion loss and extinction ratio of 2 dB and 7 dB, respectively. Subsequent work drastically reduced the device footprint, integrating VO_2 on ultracompact silicon ring resonators [56]. For a 500 nm long VO_2 patch on a TE mode

ring resonator of radius of 1.5 μm, the authors demonstrated > 10 dB extinction ratio by photothermally inducing the SMT and utilizing the resulting changes in both refraction and absorption [Figure 1.11(c)]. Although these experimental demonstrations are slow due to their thermal actuation of the SMT, they demonstrate a platform for high extinction ratio (~10 dB), low loss (~1-2 dB) operation. With the demonstrated ultrafast dynamics of VO_2 [44-51], it is expected these Si/VO_2 hybrid ring resonators can be directly leveraged to realize high-speed optical modulation with out-of-plane ultrafast excitation. Additionally, for slower speed routing of light, [57] suggests a design for a 2×2 optical switch using a Si/VO_2 hybrid ring resonator, shown in Figure 1.11(d). The authors in Ref. [58] propose modification of the silicon waveguide dimensions, VO_2 location and dimensions, and silica spacer thickness to achieve selective interaction with the TE and TM modes. While the proposed application is for efficient pass polarization [proposed device design in Figure 1.11(e)], this waveguide optimization can also be implemented for modulation applications to maximize extinction ratio.

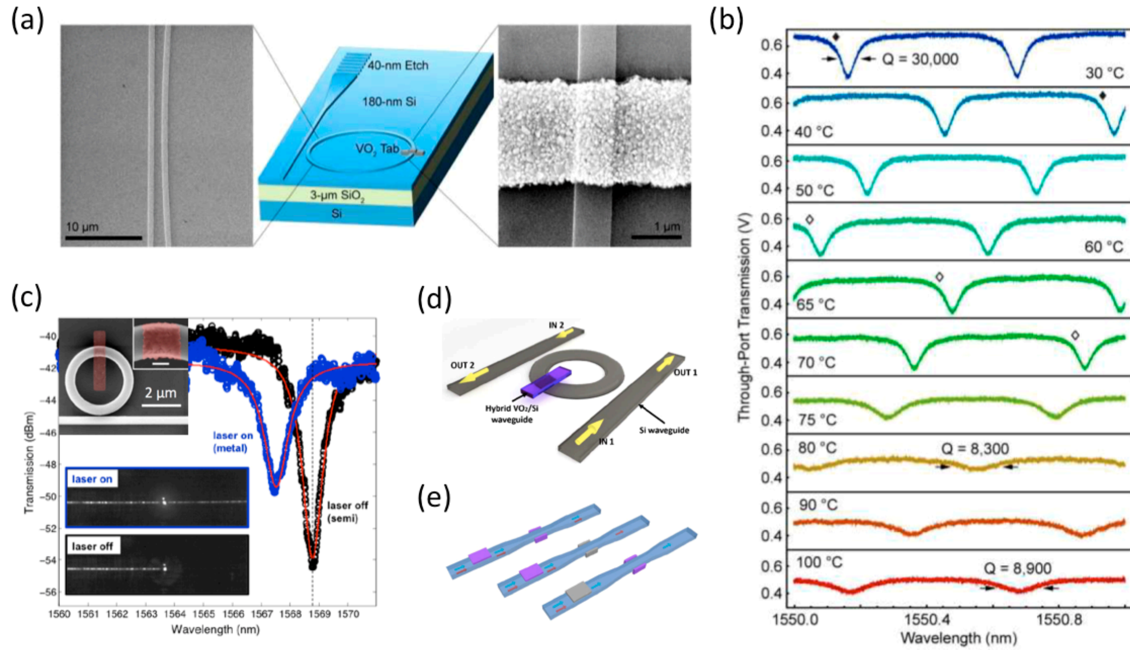

Figure 1.11. (a) Schematic and SEM images of VO_2 coated silicon ring resonator. Figure reprinted with permission from [54]. © 2010 OSA. (b) Temperature-dependent transmission of Si/VO_2 ring resonator in (a), demonstrating the change in optical response as VO_2 undergoes its SMT. Data reprinted with permission from [54]. © 2010 OSA. (c) Optical transmission of 1.5 μm radius Si/VO_2 ring resonator (SEM inset top left with VO_2 false colored maroon). At the selected wavelength (dashed line), optical transmission is low with no laser-induced photothermal heating ("laser off" inset) while transmission is high with laser induced photothermal heating ("laser on" inset) due to the resonance shift induced by the SMT. Small scale bar in SEM image inset is 250 nm. Figure and data reprinted with permission from [56]. © 2012 OSA. (d) Proposed 2×2 Si/VO_2 microring switch. Figure reprinted with permission from [57]. © 2016 IEEE. (e) Demonstration of pass polarizer using VO_2 on a designed silicon waveguide (blue). Purple and gray blocks represent VO_2:M and VO_2:R, respectively. TE and TM light are represented by blue and red arrows, respectively. Figure reprinted with permission from [58]. © 2015 OSA.

1.4.2 Electro-optic Si/VO_2 photonic devices

Vanadium dioxide has been proposed and realized for integration in electro-optic silicon photonic devices. Experimentally, electrical actuation of the SMT of a VO_2 patch coating a silicon waveguide has been demonstrated [52, 59]. In Ref. [52], for a Si/VO_2 device geometry

shown in Figure 1.12(a), the authors provide experimental evidence Poole-Frenkel emission is responsible for electrically inducing the SMT. In addition, they suggest metallic VO_2 filaments initially form between the electrical contacts and additional portions of VO_2 outside of the metal contacts can undergo the SMT via Joule heating. The time dynamics for switching the VO_2 domains outside the contacts is slower than switching the VO_2 domains between the contacts, and this is demonstrated in the device performance. By applying longer voltage pulses, the amount of VO_2 undergoing the SMT is increased giving increased extinction ratio. However, this comes with longer response times. In the geometry presented, the authors demonstrate modulation approaching 1 dB in response to a 10 ns voltage pulse. In Ref. [59], the authors explore shrinking the silicon waveguide width to 300 nm to delocalize the mode and therefore force increased optical interaction with VO_2:R. An optical microscope image of the sample using this design is shown in Figure 1.12(b). With this optimized design, increased optical contrast is demonstrated, giving 12 dB extinction ratio with a 1 μm long VO_2 patch. In this work, response times of > 1 μs are shown. This device is also characterized as a photodetector, giving a responsivity > 10 A/W.

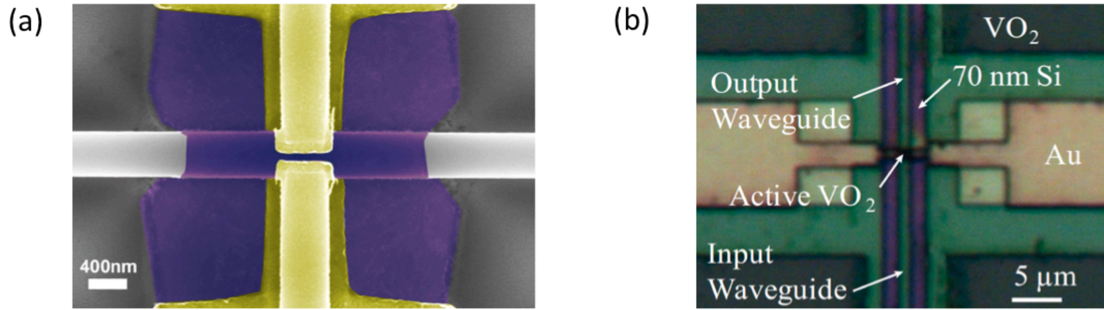

Figure 1.12. (a) SEM image of Si/VO_2 electro-optic waveguide device. VO_2 and Au are false colored purple and gold, respectively. Figure reprinted with permission from [52]. © 2015 ACS. (b) Optical microscope image of Si/VO_2 electro-optic waveguide device which delocalizes the optical mode to increase interaction with VO_2:R. Figure reprinted with permission from [59]. © 2015 OSA.

In addition, there have been interesting proposed geometries [60-62] which embed VO_2 within a silicon waveguide. Specifically in Ref. [60], the author proposes a device geometry where optical transmission is controlled by electrically actuating a thin film of VO_2 in a Si/SiO_2/VO_2/SiO_2/Si hybrid plasmonic waveguide adjacent to the input silicon waveguide. The authors suggest that by directional coupler theory, radiation from the input silicon waveguide will couple into the hybrid plasmonic waveguide. By applying a voltage across the top and bottom silicon components of the hybrid plasmonic waveguide to actuate the SMT, the VO_2 in the hybrid plasmonic waveguide becomes metallic and the optical loss is increased before the radiation couples back into the input silicon waveguide. The proposed device geometry is shown in Figure 1.13(a) and suggests implementation as a modulator will give > 3 dB extinction ratio with ~ 1 dB insertion loss over the entire C-band (1.53-1.565 μm). In Ref. [61], a similar geometry is proposed, shown in Figure 1.13(b). Here, the VO_2 segment is placed in the propagating waveguide and is positioned between the silicon waveguide and a top copper electrode. The authors analyze both TE and TM operation, suggesting in a 500 nm long device,

insertion loss and extinction ratios of 2.7 (1.79) dB and 3.87 (8.7) dB are expected for TE (TM) polarizations, respectively.

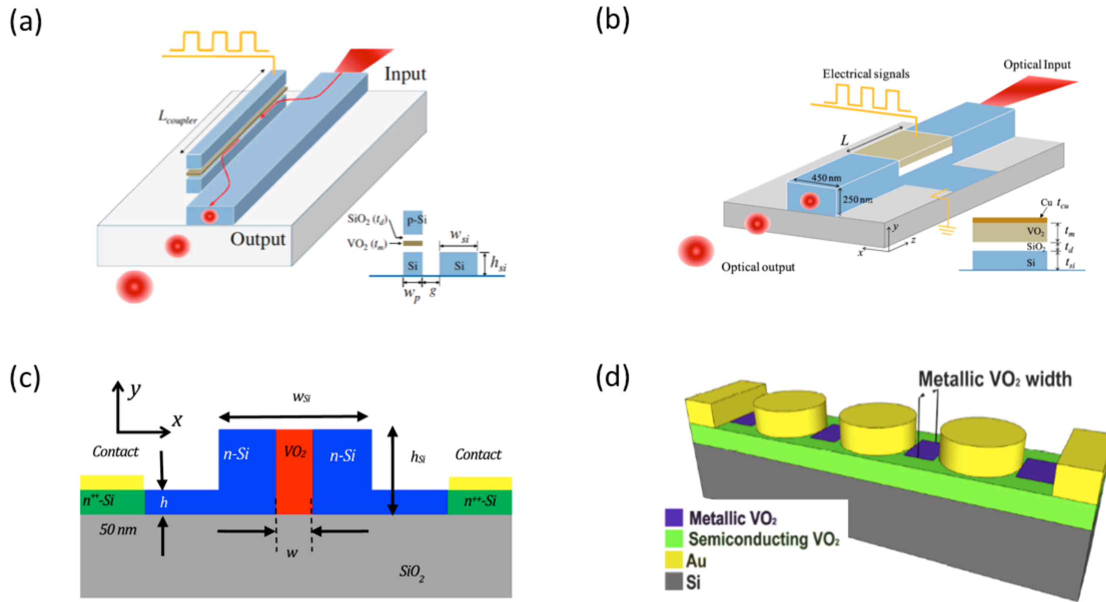

Figure 1.13. (a) Proposed Si/VO_2 electro-optic modulator design based on directional coupler theory. Figure reprinted with permission from [60]. © 2014 OSA. (b) Proposed Si/VO_2 hybrid plasmonic electro-optic waveguide modulator. Figure reprinted with permission from [61]. © 2015 IEEE. (c) Proposed Si/VO_2 electro-optic design including a vertically embedded VO_2 section within the silicon waveguide. Figure reprinted with permission from [62]. © 2017 IEEE. (d) Proposed Si/Au/VO_2 electro-optic modulator design based on near field plasmonic coupling. Figure reprinted with permission from [63]. © 2015 OSA.

In Ref. [62], the authors propose an embedded design where a vertical slot of VO_2 is placed in the center of a heavily doped silicon waveguide [Figure 1.13(c)]. The authors determined the optimal device geometry for maximum changes in propagation losses (α) by sweeping the widths of the silicon waveguide and VO_2 section. As an electro-absorption modulator, simulations for the optimized design suggest very large extinction ratio (21 dB) and modest insertion loss (3 dB) are possible for a device length of 1 μm. In addition to these embedded designs, a Si/VO_2/Au

plasmonic-photonic electro-optic modulator, shown in Figure 1.13(d), was proposed suggesting ~ 9 dB/μm extinction ratio/length and the potential for reduced power consumption [63].

1.4.3 All-optical Si/VO_2 photonic devices

As a continuation of the work described in Section 1.4.1 where VO_2 was integrated on an ultrasmall silicon ring resonator and linear silicon waveguides [56], transient functionality was demonstrated using a nanosecond optical pulse (~ 25 ns FWHM) to initiate the SMT of VO_2 [64]. Figure 1.14(a) presents the Si/VO_2 ring resonator in addition to the transient optical transmission as a function of incident fluence. For lower fluences, the optical response approaches the temporal envelope of the excitation pulse. With increasing fluence, the maximum transmission increases as a result of accessing the full SMT of VO_2, and for the highest fluences shown, the longer device response times are associated with VO_2 experiencing a thermal environment beyond what is required to access its SMT, forcing longer times to return to the temperature required to undergo the MST. Additionally, recent work has proposed the use of a Au/VO_2 hybrid pattern on a silicon waveguide for all-optical modulation with in-plane excitation [65] **[**Figure 1.14(b)]. Although this design suggests large extinction ratio/length (24 dB/μm), it exhibits large insertion loss (~ 7 dB) and is expected to require relatively complex fabrication.

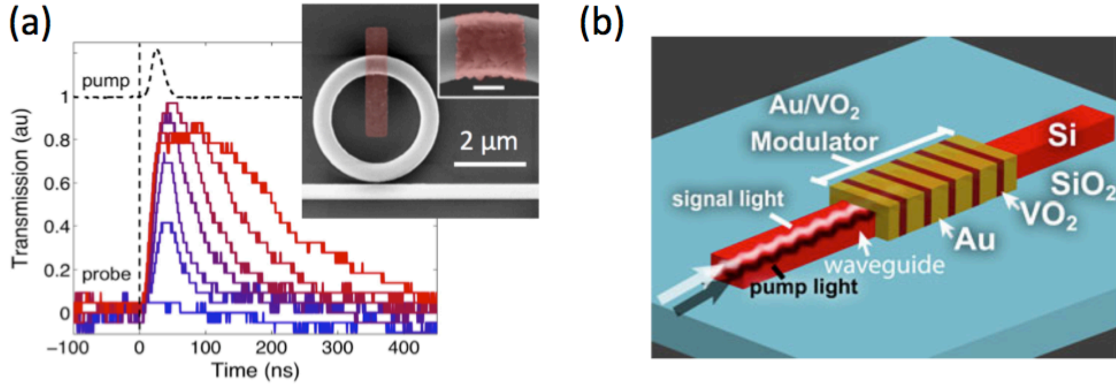

Figure 1.14. (a) Transient response of Si/VO_2 ring resonator for increasing pump fluence. Fluences range from 0.45-4.74 mJ/cm^2 and are increasing from blue to red. SEM image of Si/VO_2 ring resonator in top right (VO_2 is false colored maroon). Small scale bar in SEM image inset is 250 nm. Figures taken and adopted with permission from [56, 64]. © 2012 OSA, © 2013 OSA. (b) Schematic for proposed $Si/Au/VO_2$ all-optical modulator. Figure reprinted with permission from [65]. © 2018 IEEE.

1.5 Objectives and dissertation overview

The objective of this thesis is to continue to push forward the practical functionality of integrated Si/VO_2 photonic devices, in particular for implementation as electro-optic and all-optical modulators. In **Chapter 2**, platforms for Si/VO_2 electro-optic modulation are presented, including the design, fabrication, and characterization of a Si/VO_2 electro-optic ring resonator device. In **Chapter 3**, platforms for Si/VO_2 all-optical modulation are presented, including the design, fabrication, and characterization of a hybrid waveguide comprising a VO_2 patch embedded within a silicon waveguide. While only voltage-driven thermal actuation is demonstrated in Chapter 3, the embedded design provides a potential platform for in-plane all-optical modulation. In **Chapter 4**, expected performance of the device presented in Chapter 3 as an all-optical modulator with in-plane excitation is presented in comparison to other in-plane all-optical modulators. In addition, further improvements for practical implementation of Si/VO_2

electro-optic and all-optical modulators are proposed and discussed, including an analysis of waveguide geometry considerations, transient mode propagation, and polarization independent operation. Lastly, in **Chapter 5** a brief conclusion of this thesis is presented and future research avenues are suggested.

Chapter 2

2. Platforms for Si/VO_2 electro-optic modulation

2.1 Introduction

As mentioned in Section 1.2, integration of on-chip optical and electrical components provides a potential pathway to continue to improve the performance of traditional information processing systems [66]. Considering only silicon-based platforms, realization of these electronic-photonic systems requires the development of silicon-based chip-scale lasers [9], photodetectors [11, 12], and electro-optic modulators [10]. Platforms for electro-optic modulators, which serve to imprint an electrical signal on an optical signal, are the focus of this chapter. As mentioned in Section 1.2.1, there have been two primary types of proposed silicon-based photonic electro-optic modulators: (i) silicon-only electro-optic modulators and (ii) hybrid electro-optic modulators which integrate a second active material with optical properties superior to silicon within a silicon photonic platform. The designs in this chapter fall within the second type, specifically integrating vanadium dioxide (VO_2) into silicon photonic devices. Described in detail in Section 1.3.1, VO_2 is a transition metal oxide optical phase change material which demonstrates dynamic optical tunabilty (at 1550 nm, n and κ go from 3.3 and 0.3 to 1.8 and 3.3, respectively) [43]. While its SMT and MST have been shown to be no more than 2 [52, 53] and 3 ns [52], respectively, when electrically actuated, sufficient optical modulation (4-5 dB) at these time scales has remained evasive [52, 59]. In this chapter, VO_2 is first integrated on top of a silicon photonic ring resonator device with the goal of achieving improved optical modulation while maintaining the temporal device response. Additionally, a design for a Si/VO_2 electro-absorption modulator with fundamental TM mode operation is presented and characterized.

2.2 Si/VO_2 electro-optic ring resonator modulator

With optical excitation, prior work, presented in Section 1.4.3, demonstrated the potential for implementation of ring resonator structures to enhance the light-matter interaction with VO_2, and therefore demonstrate improved optical performance [64]. Specifically, for a given VO_2 patch length of 500 nm, in a linear geometry, ~ 2 dB extinction ratio was achieved, while for an identical VO_2 patch in a ring resonator structure, ~ 7 dB extinction ratio was achieved. With this knowledge, in addition to the demonstrated ability to modify optical waveguide transmission by electrically initiating the SMT of VO_2 atop a silicon waveguide [52, 59], here, electrical actuation of the SMT of a patch of VO_2 on a silicon ring resonator is explored.

2.2.1 Si/VO_2 ring resonator fabrication

The Si/VO_2 ring resonators were fabricated in three lithography steps, the results of which are presented in schematics in Figure 2.1(b-d). The first lithography step defined the silicon ring resonator photonic structure and silicon supports to ensure continuous electrical contacts in a SOITEC silicon-on-insulator (SOI) wafer (220 nm Si layer; 3 µm SiO_2 box layer). These silicon supports proved to be integral in improving device reliability in the Si/VO_2 electro-absorption design in Ref. [52], as device failure often occurred without them, likely due to electrical contact burnout when the electrical contacts were patterned on the side walls of the silicon waveguides. The SOI wafer was cleaved into a small square (*e.g.,* 30 mm × 30 mm) and excess particulates were removed with N_2 gas. ZEP 520A electron beam resist was spun at 6000 rpm and subsequently prebaked for 2 minutes at 180°C. In order to define the silicon structures, the pattern was exposed using a JEOL 9300FS 100kV electron beam lithography system at the Center for Nanophase Materials Sciences (CNMS) at Oak Ridge National Laboratory. Samples

were then developed for 30 seconds in Xylenes, rinsed multiple times with isopropyl alcohol (IPA), and dried with N_2. The wafer was etched using a C_4F_8, SF_6, Ar gas mixture in an Oxford Plasmalab 100 RIE system at CNMS. The etch recipe consisted of a 3 second strike step at RF and ICP powers of 50 and 1800 W with gas flows of 50 sccm C_4F_8, 12 sccm SF_6, and 50 sccm Ar followed by a 2 minute, 15 second etch (RF and ICP powers of 30 and 1200 W with gas flows of 60 sccm C_4F_8, 25 sccm SF_6, and 5 sccm Ar). With a measured silicon etch rate of ~ 160 nm/minute, this etch likely etches into the SiO_2 layer. However, it is expected this is insignificant due to the low etch rate of SiO_2 for this etch recipe. The table temperature was set to 20°C during both the strike and etch steps. Following the silicon etch, a ten-minute O_2 descum was performed (100 W RF power and 20 sccm O_2 at 20°C table temperature) to strip remaining ZEP 520A resist.

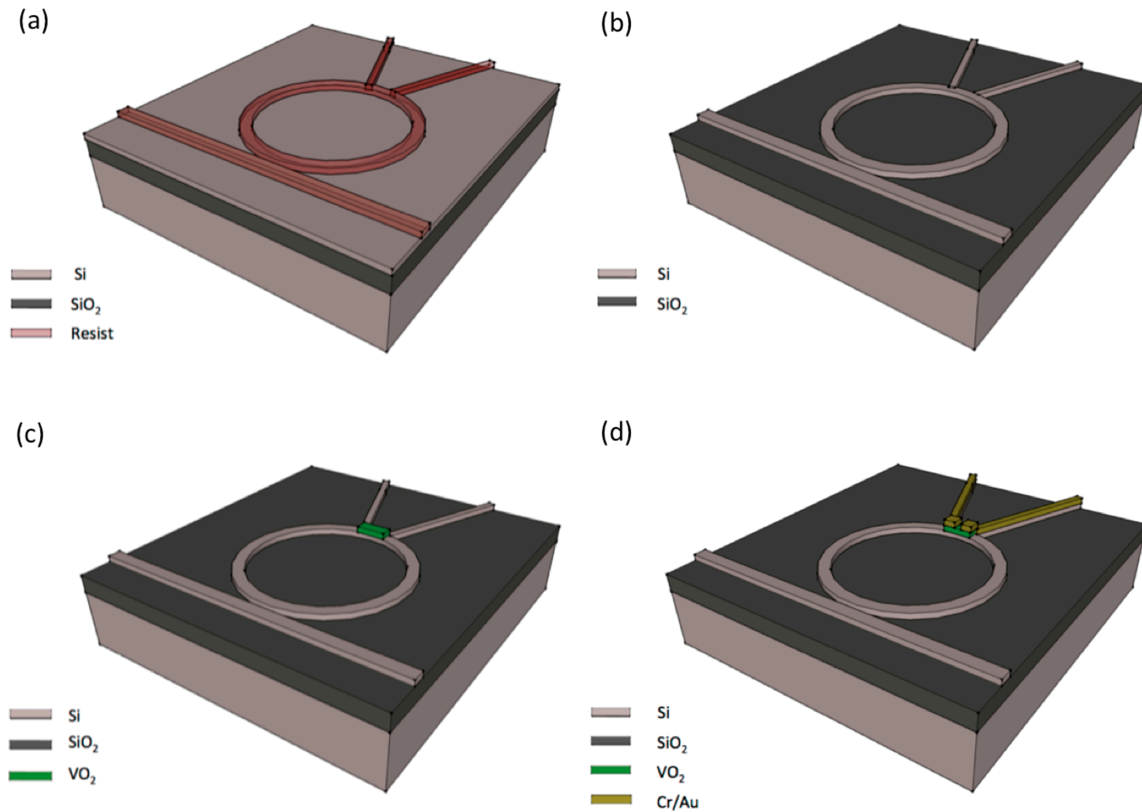

Figure 2.1. Multilayer lithography patterning of Si/VO_2 electro-optic ring resonator modulator. Throughout the figures, Si, SiO_2, VO_2, Cr/Au, and the resist are light gray, dark gray, green, gold, and red, respectively. (a) Patterning and development of resist in preparation of etching of silicon photonic ring resonator. (b) Silicon photonic ring resonator after etching and subsequent liftoff of resist. (c,d) Silicon photonic ring resonator after resist patterning, deposition of VO_2 (c) and Cr/Au (d), and subsequent liftoff of resist.

Before the second lithography step, the sample was soaked in piranha solution (H_2SO_4/H_2O_2 3:1) for one minute at room temperature and subsequently rinsed with deionized (DI) H_2O to ensure that no residual ZEP 520A remained on the sample surface. The VO_2 patch and metal contacts were placed on the device in the second and third lithography steps. For both steps, 950 PMMA A4 electron beam resist was spun at 500 rpm for 5 seconds, 2000 rpm for 45 seconds, and prebaked for 90 seconds at 180°C in the Vanderbilt Institute of Nanoscale Science and Engineering (VINSE). The resist-coated samples were then exposed using a Raith eLine electron

beam lithography system in VINSE. The dosing parameters (dose, aperture, step size, voltage) were 750 μC/cm^2, 30 μm, 10 nm, and 20 kV and 300 μC/cm^2, 30 μm, 20 nm, and 20 kV for the second and third lithography steps, respectively. For patterning of the large electrical contact features [everything outside of the blue box in Figure 2.2(a)], an aperture of 100 μm was used to reduce the write time to ~ two minutes per pair of electrical contacts. After exposure, samples were developed in methyl isobutyl ketone (MIBK)/isopropyl alcohol (IPA) 1:3 for 45 seconds and 90 seconds for the second and third lithography steps, respectively. After the second and third lithography steps, residual 950 PMMA A4 was removed in a short O_2 clean to ensure the VO_x and metal contacts were deposited on a clean surface. Surface cleanliness is expected to be very important for consistent electrical performance. For the VO_2 deposition, a vanadium-metal target was RF sputtered at 6 mTorr pressure with 20 sccm Ar and 1 sccm O_2 in a multipurpose Angstrom deposition tool in VINSE. The chamber pressure was initially set to 40 mTorr to ignite the plasma after which it was returned to 6 mTorr. After deposition of VO_x, room temperature liftoff was performed in acetone for ~ one hour, followed by rinsing with acetone and IPA (front and back of sample multiple times), and drying with N_2. To form polycrystalline VO_2, the sample was annealed for 9 minutes at 450°C in a vacuum-sealed tube furnace at 250 mTorr O_2 pressure. For the metal contacts, resistive evaporation was used in VINSE to deposit chromium for adhesion to the silicon surface and gold for electrical contact. Another room temperature liftoff was then performed in acetone for ~ three hours, followed by thorough rinsing with acetone and IPA and drying with N_2. VO_2 and Cr/Au deposition thicknesses were measured by profilometry (Veeco Dektak 150 profilometer) on witness samples in VINSE. Figure 2.2 shows a fully fabricated device. The VO_2 patches were 500 nm wide (covering the width of the ring resonator waveguide), ~ 100 nm thick, and of variable length (L_{VO_2}). Gold/chromium thickness

(desired target deposition of 5 nm Cr and 50 nm Au) was measured to ~ 65 nm. The silicon ring resonator was 5 μm in radius with a 500 nm (wide) × 220 nm (thickness) waveguide geometry. The silicon supports were ~ 100 nm in width at their connection point to the silicon ring resonator.

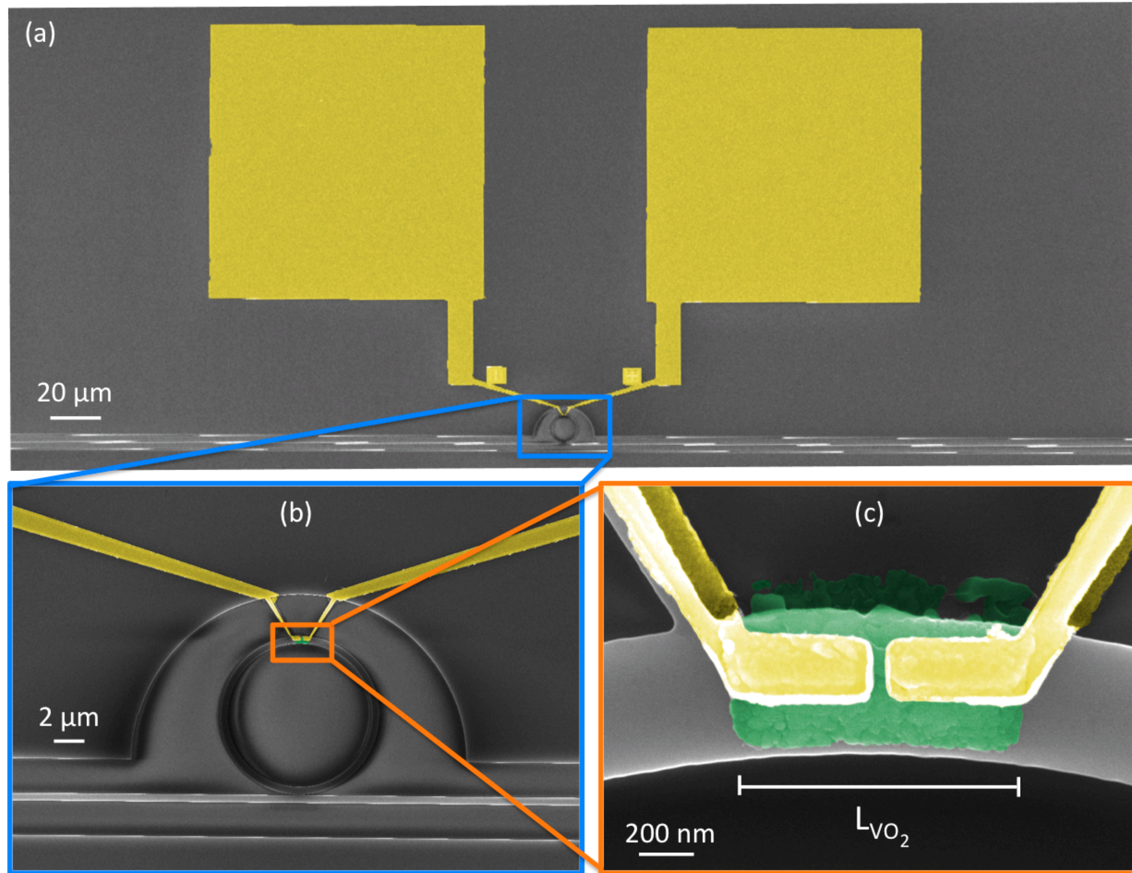

Figure 2.2. (a) SEM image of fully fabricated Si/VO_2 ring resonator modulator, including gold contact pads (100 μm × 100 μm) for electrical access. (b) Zoomed-in SEM image to show detail of Si/VO_2 ring resonator. (c) Zoomed-in SEM image showing patterned VO_2 and Au on silicon ring resonator structure. Patterned VO_2 patches are of variable lengths (L_{VO_2}). The VO_2 patch shown in this image has L_{VO_2} = 1 μm. In both images, VO_2 and Au are false colored green and yellow, respectively.

2.2.2 Characterization of VO_2

2.2.2.1 Optical characterization of VO_2

To verify that the VO_x films had formed stoichiometric VO_2 under annealing, the switching temperature for the SMT (T_{SMT}) was measured by temperature-dependent reflectometry. Measurements were performed on a thin film of VO_2 on a silicon substrate that experienced identical processing conditions as the VO_2 deposited on the modulator devices. A fiber coupled 3000 K tungsten-halogen light source (Spectral Products – Model ASBN-W-L) was incident on the sample. The sample temperature was controlled by a Peltier heater attached to the stage and temperature-dependent reflected power was detected using an InGaAs photodetector (Thorlabs PDA10CS). Figure 2.3(a) shows the experimental result. As the temperature is increased, VO_2 undergoes the SMT around 65°C, which is typical for VO_2 films. This is exhibited by an increase in the measured reflectance as the VO_2 is more reflective in the VO_2:R phase. As the VO_2 film temperature returns to room temperature, reflectance drops to its original baseline as the VO_2 undergoes the MST.

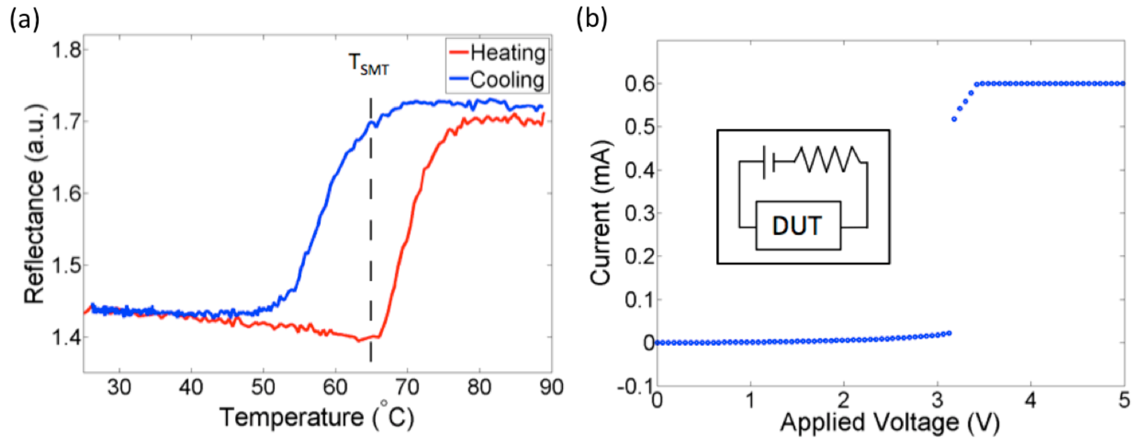

Figure 2.3. (a) Temperature-dependent reflectometry of a thin film VO_2 witness sample on silicon, demonstrating T_{SMT} ~ 65 °C. (b) Typical IV curve from voltage sweep applied to a Si/VO_2 ring resonator device. Schematic of electrical measurement is shown in inset. The in-series resistor is 3 kΩ for the measurement shown. Discontinuity in current is indicative of the SMT of VO_2. Figures reprinted with permission from [67]. © 2016 SPIE.

2.2.2.2 Electrical characterization of VO_2

The VO_2 switching voltage was determined by performing IV measurements [schematic for electrical measurement is shown in inset of Figure 2.3(b)] on the Si/VO_2 ring resonator using a Keithley 2400 Sourcemeter. For the curve shown in Figure 2.3(b), a 3 kΩ in-series resistor was used to limit current passing through the device after the VO_2 undergoes the SMT. The discontinuity in current is indicative of the SMT as the sharp increase in current is a result of VO_2 switching from the more electrically resistive VO_2:M phase to the more electrically conductive VO_2:R phase. The constant 600 μA current after the discontinuity is due to the current limit of 600 μA programmed with the Keithley 2400 Sourcemeter to protect from device failure. Assuming negligible resistance in the gold contacts and subtracting the voltage drop across the 3 kΩ resistor (3 kΩ multiplied by the measured current just before the discontinuity), the switching voltage is 3.06 V. With approximately 100 nm between contacts, this switching

voltage corresponds to a threshold electric field of 3.06×10^7 V/m, which is in agreement with previously measured values [53, 68].

2.2.3 Experimental setup

Electro-optic and thermo-optic characterization of the Si/VO_2 ring resonators was performed, and the experimental setup for each characterization is presented below. For all measurements, TE polarized light from a tunable laser (Santec TSL-510) was coupled into the device via butt coupling of a lensed tapered fiber (OZ Optics 39318 TPMJ-3U-1550-8/125-0.25-10-2.5-14-1). Methods of polarization control and characterization can be found in Appendix A.1. The optical signal was coupled out of the device via a lensed tapered fiber and received by a power meter (Newport 2936-C). All transmission spectra were acquired using the Santec Swept Test System STS-510 software package. Figure 2.4 shows an image of the full fiber-coupled, optical characterization setup for passive device characterization. Below, modifications to this setup to allow for active (*i.e.*, electro-optic, thermo-optic) characterization are presented.

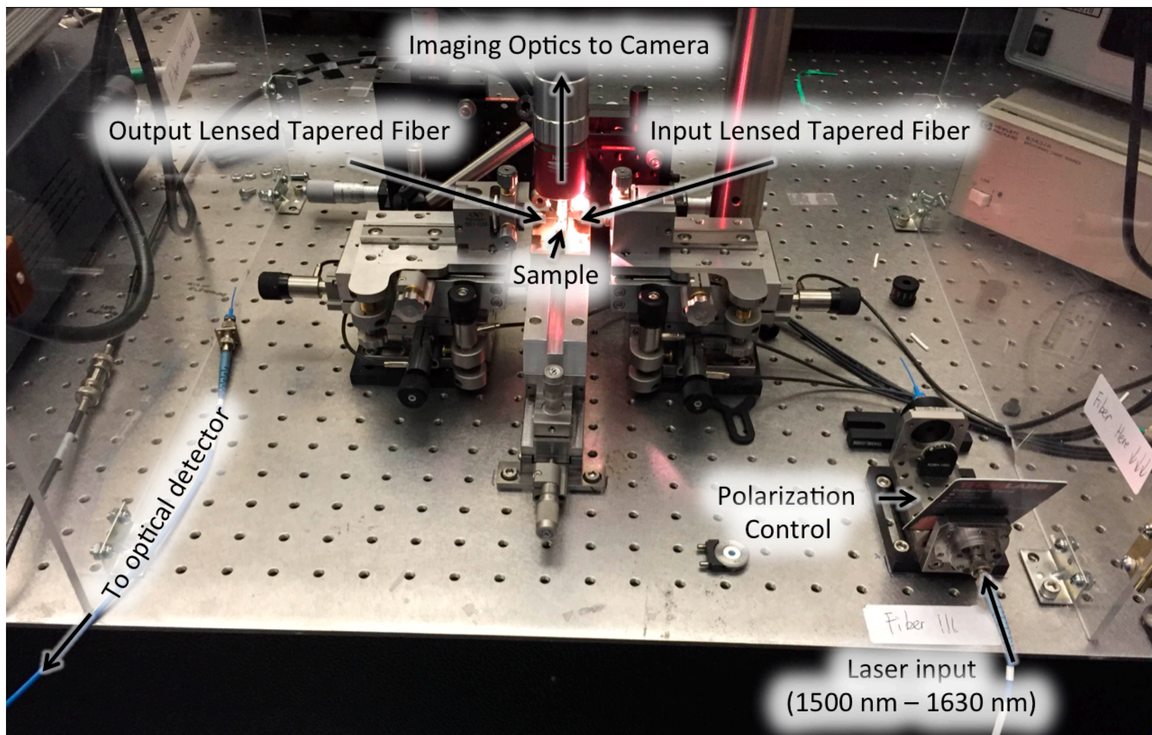

Figure 2.4. Fiber-coupled optical setup for passive characterization of integrated silicon photonic devices. Polarization of tunable laser input from Santec TSL-510 is determined with variable orientation of a linear polarizer and half-wave plate, shown in the bottom right. Optical input is coupled into and out of the device with lensed tapered fibers. This is achieved with visual aid from a live monitor image, using a Mitutoyo M Plan Apo NIR 20X microscope objective. Outcoupling signals are received by a power meter (Newport 2936-C).

2.2.3.1 Electro-optic experimental setup

For all electro-optic measurements, the sample was mounted to a high-speed sample holder [Figure 2.5(a)]. Electrical connections to the Au pads were made using a Westbond 7476D wire bonder. The electrical source was connected at one terminal while the other was grounded through an in-series resistor. Steady-state electro-optic measurements were performed using a Keithley 2400 Sourcemeter. High-speed electro-optic measurements were performed using a Stanford Research Systems DG535 pulse generator. Figure 2.5(b) shows the high-speed sample holder integrated into the optical fiber-coupled setup. For high-speed measurements, the output

optical signal was converted to an electrical signal with a high-speed photodetector (Menlo Systems FPD 510) and then read out on an oscilloscope (Tektronix TDS 2024C).

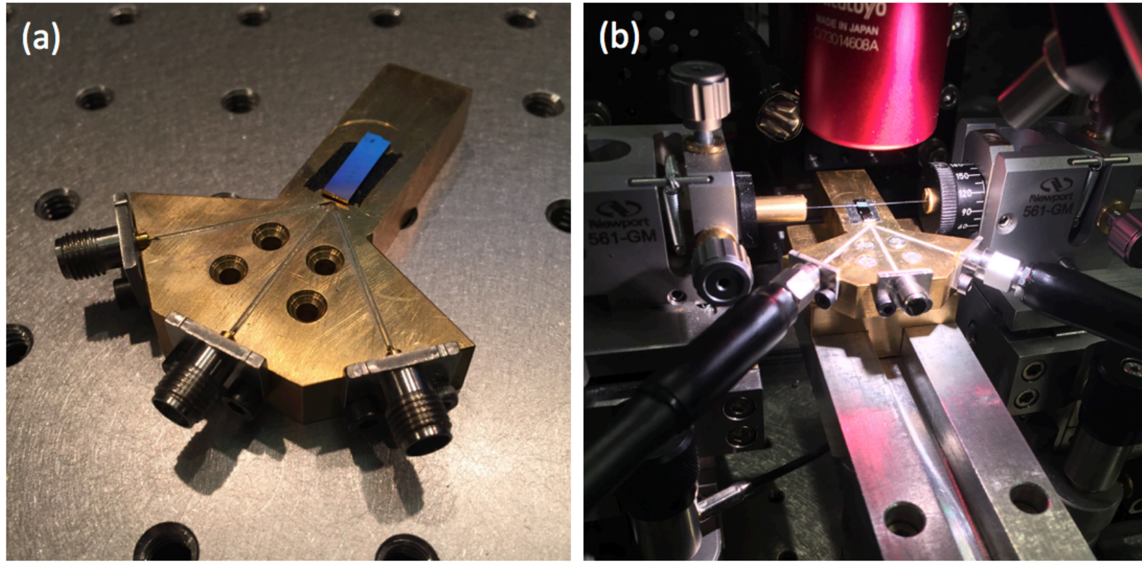

Figure 2.5. Electro-optic experimental setup. (a) Sample holder including a mounted device. For electro-optic characterization, electrical connection to the sample holder was made with electrical cables. Electrical connection to the device was achieved via wire bonding from the electrical strips to the patterend contact pads on the device. (b) Electro-optic sample holder integrated into fiber-coupled, optical setup. Optical input and output coupling are achieved using lensed tapered fibers, and the electrical signal is supplied via connection to the right and left SMA ports of the sample holder. The left port is connected to the electrical supply and the right port is grouded through an in-series resistor.

2.2.3.2 Thermo-optic experimental setup

For thermo-optic measurements, the sample was mounted on a Physitemp TS-4MP thermal stage, shown in Figure 2.6(a). Active stage temperature control (20°C - 100°C) was supplied by a water-based Physitemp PTU-3 pump and tank unit, shown in Figure 2.6(b). For these thermo-optic measurements, thermal fluctuations were reduced by ensuring all components of the sample, stage, and lensed tapered fibers were tightly secured. In addition, reducing the distance

by which the fibers extend from the copper casing and extending the distance between fibers and the sample (while still maintaining optical coupling) minimized thermally induced transmission fluctuations.

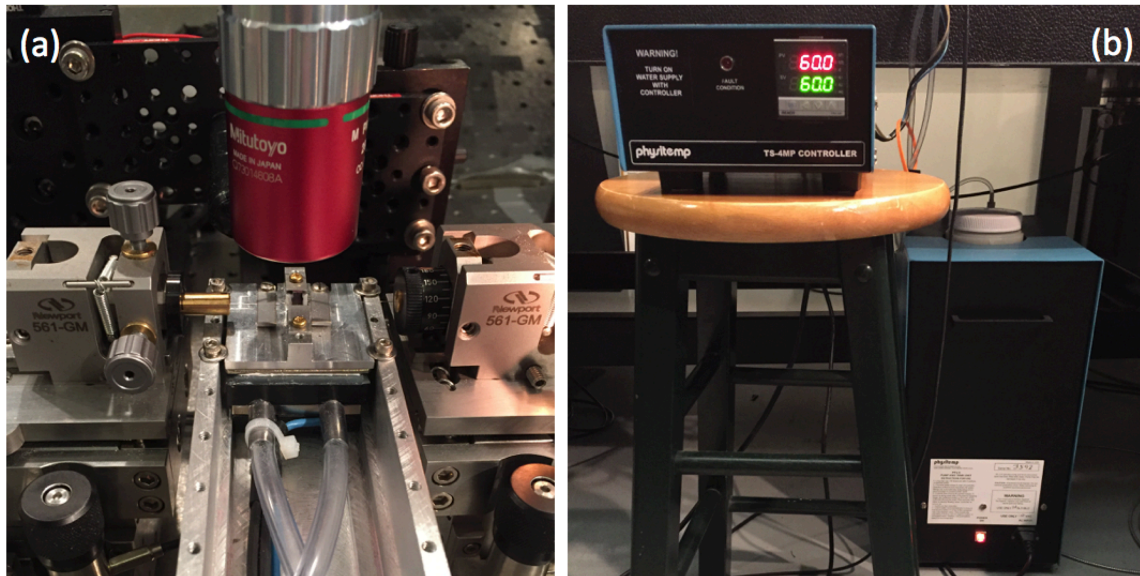

Figure 2.6. Thermo-optic experimental setup. (a) Si/VO_2 ring resonator sampled mounted on Physitemp TS-4MP thermal stage, showing optical input and output coupling using lensed tapered fibers. (b) Physitemp PTU-3 pump and tank unit for controlling the sample temperature. Here, the sample temperature is set to 60°C.

2.2.4 Results and discussion

Steady-state electro-optic measurements were performed to initially characterize the Si/VO_2 ring resonator response to an applied voltage. The experimental setup used for these experiments is described in Section 2.2.3.1. Figure 2.7(a) shows the transmission spectra for applied voltages of 0 V and 3.2 V on a device with L_{VO_2} = 3 µm. Corresponding results from a high-speed electro-optic measurement are shown in Figure 2.7(b). Figure 2.7(c) and Figure 2.7(d) show steady-state

and high-speed electro-optic measurements on a device with L_{VO_2} = 1 μm. All devices in Figure 2.7 were measured with a 3 kΩ in-series resistor.

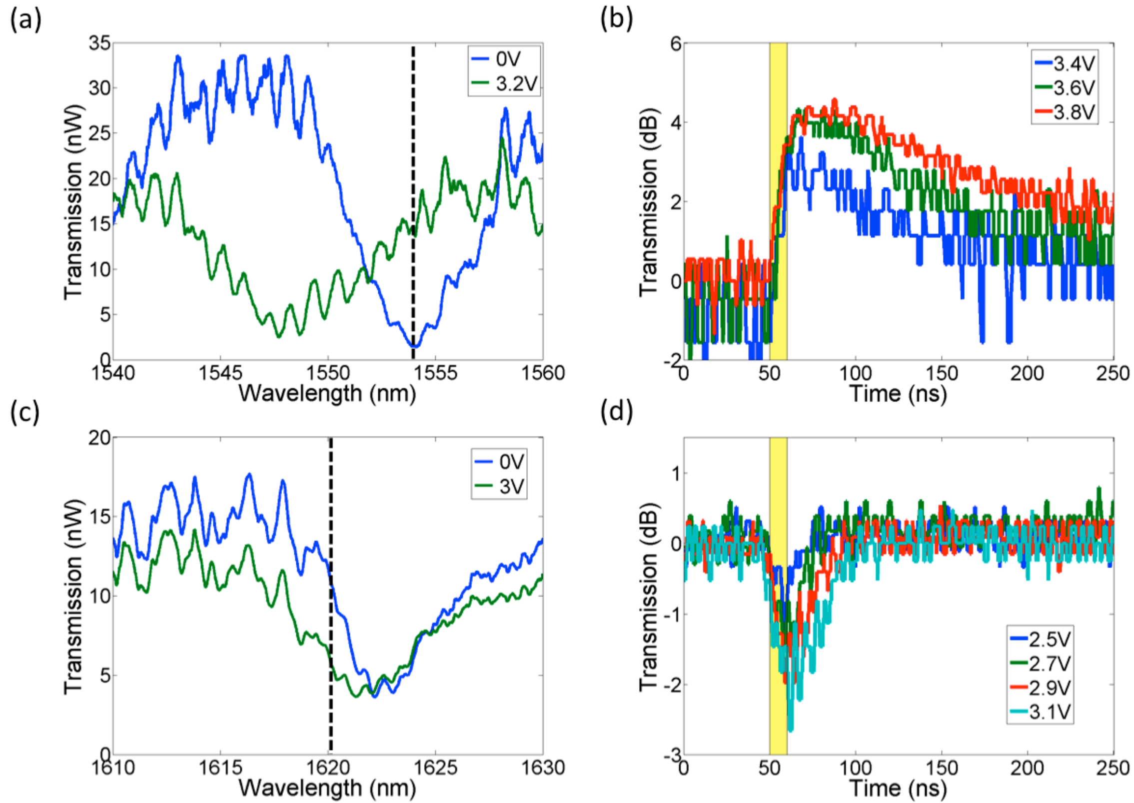

Figure 2.7. (a) Steady-state and (b) high-speed electro-optic measurements for a Si/VO_2 ring resonator device with L_{VO_2} = 3 μm. (c) Steady-state and (d) high-speed electro-optic measurements for a similar device with L_{VO_2} = 1 μm. In (a) and (c), the dashed vertical lines represent the wavelength at which the high-speed measurement was taken in (b) and (d), respectively. The yellow block in (b) and (d) highlights the time duration when the square voltage pulse is on. Figures reprinted with permission from [67]. © 2016 SPIE.

As the VO_2 patch undergoes the SMT, a blueshift of the resonance is expected. The SMT decreases the refractive index of the VO_2 patch and therefore reduces the modal index for the light in the ring resonator. The decreased modal index leads to a blueshift of the resonant wavelength of the ring, as demonstrated in previous thermo-optic and all-optical measurements

[56, 64]. Figure 2.7(a) and Figure 2.7(c) indeed show blueshifted resonances when VO_2 switches from the VO_2:M to the VO_2:R phase. A larger blueshift is observed with the larger VO_2 patch and it is expected believe the entire VO_2 patch is being switched in both cases, as discussed in the next paragraph. In the steady-state measurement shown for the L_{VO_2} = 3 μm device [Figure 2.7(a)], an extinction ratio of 10 dB is measured between applied voltages of 0 V and 3.2 V at a probe wavelength of 1554.16 nm. At this wavelength, in response to a 10 ns square voltage pulse, extinction ratios of ~ 3 – 4.5 dB are measured depending on the applied voltage. This indicates the entire 3 μm VO_2 patch does not undergo the SMT, suggesting 10 ns is not sufficient time for the Joule heating mechanism proposed by Ref. [52], described in Section 1.4.2, to switch the entire patch. In the steady-state measurement shown for the L_{VO_2} = 1 μm device [Figure 2.7(c)], an extinction ratio of 2.9 dB is measured between applied voltages of 0 V and 3 V at a probe wavelength of 1620.38 nm. At this wavelength, in response to a 10 ns square voltage pulse, extinction ratios of ~ 1.5 – 2.6 dB are measured depending on the applied voltage, suggesting for the highest voltages, 10 ns is sufficient time for nearly all 1 μm of the VO_2 patch to undergo the SMT. Additionally, Figure 2.7(b) and Figure 2.7(d) give important insight into the device recovery times. In both devices, it is apparent that recovery times become longer for higher applied voltages. This is most likely attributable to two effects: (i) the portion of VO_2 which is switched to the VO_2:R phase and (ii) the temperature of the VO_2 patch. For the L_{VO_2} = 1 μm device, at an applied voltage of 2.5 V, just above the switching voltage for this device, an extinction ratio of ~ 1.5 dB is measured. However, increasing the voltage to 3.1 V results in an extinction ratio of ~ 2.6 dB which is nearly equivalent to the steady state measurement of 2.9 dB, suggesting nearly all of the VO_2 patch is in the VO_2:R phase. Therefore, for the L_{VO_2} = 1 μm device, as the voltage is increased from 2.5 to 3.1 V, the volume of the VO_2 that is in the VO_2:R

phase is increasing, resulting in larger extinction ratios but also longer recovery times. The VO_2 patch temperature increase that is associated with increasing applied voltages is also expected to increase recovery times. Before the VO_2 patch can return to the VO_2:M phase and the transmission intensity can return to its initial value, the temperature of the VO_2 patch must fall below $T_{SMT.}$ Hence, thermal dissipation is a key consideration in these devices. For the L_{VO_2} = 3 μm device, the recovery times are ~ 5x longer than for the L_{VO_2} = 1 μm device, suggesting more than 1 μm of the 3 μm long VO_2 segment is in the VO_2:R phase for all applied voltages. For the L_{VO_2} = 3 μm device, for increasing voltages, larger extinction ratios and longer recovery times are also exhibited, as was seen in the L_{VO_2} = 1 μm device.

To verify that the entire patch is switching in the steady-state electro-optic measurements in Figure 2.7, thermal measurements were performed on the L_{VO_2} = 3 μm device measured in Figure 2.7(a). The resonance shift as a function of temperature is shown in Figure 2.8(a). The raw data reveal contributions from the SMT of VO_2 (blueshift contribution) and the thermo-optic coefficient of silicon (redshift contribution). For temperatures below the SMT, the silicon thermo-optic coefficient leads to an overall redshift of the ring resonator resonance while for temperatures near the SMT, the change in refractive index of the VO_2 dominates the silicon thermo-optic effect and leads to an overall blueshift of the resonance. Significantly above the SMT, a slight redshift can again be observed due to the silicon thermo-optic effect. Figure 2.8(a) also shows normalized data that subtracts the contribution from the silicon thermo-optic effect and therefore reflects the resonance shift due only to the contribution from the SMT of VO_2. The data were normalized by carrying out a linear fit of the first five raw data points to account for the thermo-optic effect and subsequently subtracting that contribution from the data set. The normalized resonance shift of 6.1 ± 0.6 nm is in good agreement with the measured resonance

shift of ~ 5.5 nm between 0 V and 3.2 V in Figure 2.7(a), suggesting that the entire patch is in the VO_2:R phase after applying a steady-state voltage.

In order to gain further insight into the dependence of VO_2 switching performance on the portion of the VO_2 patch in the VO_2:R phase, which relates to the applied voltage, a 10 kΩ in-series resistor was used in order to limit the current passing through a different L_{VO_2} = 3 μm device. Figure 2.8(b) demonstrates an incremental blueshift for this device as the voltage is increased up to 6 V, indicating a proportional switching of VO_2. Between 6 and 7 V, there is no change in resonance wavelength, indicating that at 6 V the entire patch has switched. In Figure 2.8(b), an applied voltage of 6 V corresponds to a measured current of 429 μA whereas 440 μA was measured at 3.2 V in Figure 2.7(a). Therefore, although different resistors were used and consequently the applied voltages were different, the voltage drop and current passing through the VO_2 is nearly identical, suggesting that the current is the driving factor in the extent of the VO_2 patch that switches, discussed further in the next paragraph.

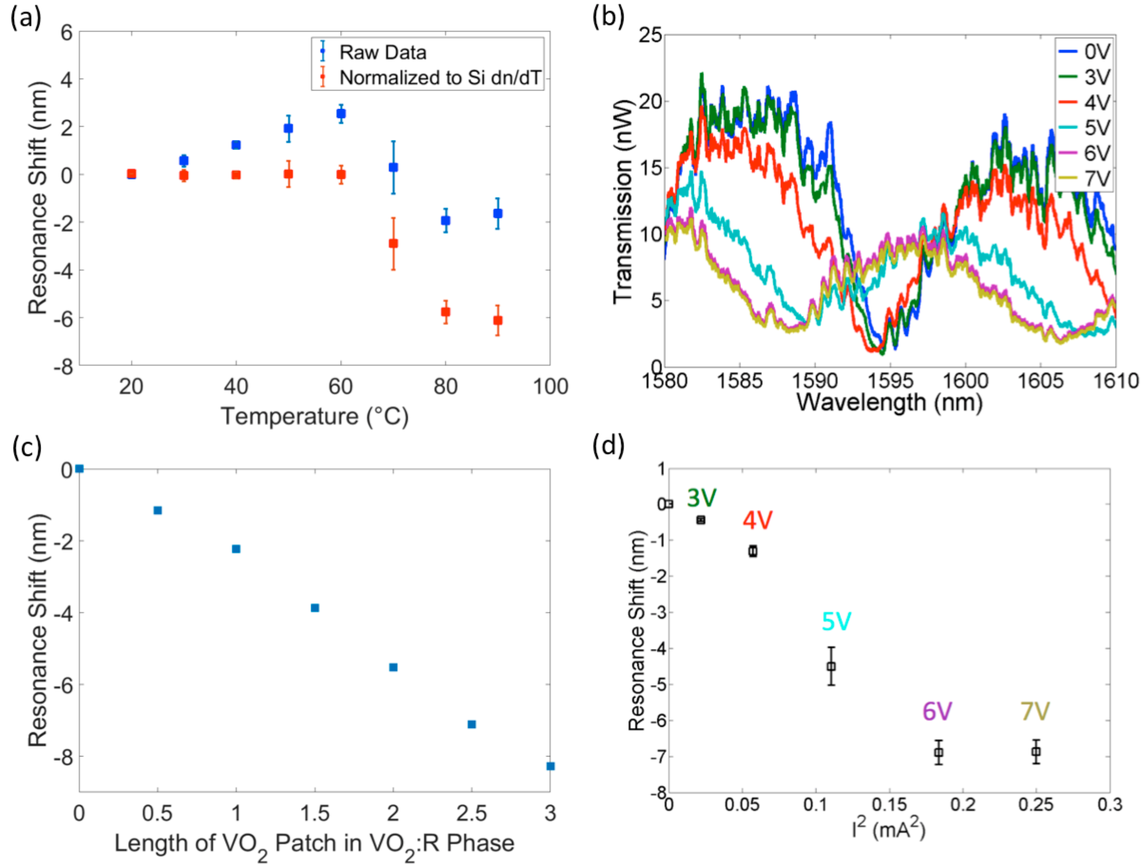

Figure 2.8. (a) Measured resonance shift as a function of temperature for the L_{VO_2} = 3 μm device presented in Figure 2.7(a,b). (b) Transmission spectra for an additional L_{VO_2} = 3 μm device at various voltages (10 kΩ in-series resistor). (c) Three-dimensional FDTD calculations of the resonance shift of an L_{VO_2} = 3 μm Si/VO_2 ring resonator device where the portion of VO_2 in the VO_2:R phase is varied. (d) Measured resonance shift as a function of I^2 for the L_{VO_2} = 3 μm device presented in (b). Figures reprinted with permission from [67]. © 2016 SPIE.

Figure 2.8(c) and Figure 2.8(d) provide additional confirmation that the full patch of VO_2 is switching in the steady-state voltage regime, and further evidence that the fraction of the VO_2 patch that switches depends on the current passing through the patch. Figure 2.8(c) displays three-dimensional finite-difference time-domain (FDTD) simulation results (Lumerical FDTD Solutions) for a L_{VO_2} = 3 μm device where the fraction of the VO_2 patch that is in the VO_2:R phase is varied. A linear dependence of the resonance shift on the fraction of the VO_2 patch in

the VO_2:R phase is found. In the simulation, VO_2 optical constants were taken from [69]. The calculated resonance shift of ~ 8 nm is in reasonable agreement with the measured resonance shifts of ~ 5.5 nm and ~ 7 nm for the L_{VO_2} = 3 μm devices reported in Figure 2.8(a) and Figure 2.8(b), respectively. The slight differences in resonance shift are most likely attributable to the coarse mesh rendering that was implemented for efficient computation as well as slight variations in the thickness of the VO_2 deposited on the two devices measured in Figure 2.8(a) and Figure 2.8(b). In Figure 2.8(d), the measured resonance shift for the L_{VO_2} = 3 μm device from Figure 2.8(b) is plotted as a function of I^2. Error bars are calculated from resonance shifts of multiple resonances. A linear trend is observed from 3 V to 6 V, suggesting that the magnitude of the resonance shift depends linearly on I^2 in this regime, and saturation of the resonance shift occurs at 6 V and 7 V when the VO_2 patch is presumed to be fully switched. Comparison of Figure 2.8(c) and Figure 2.8(d) shows that I^2 is associated with a linear change in the VO_2 patch size, suggesting mainly a Joule heating contribution, which is governed by $P_{Joule} = I^2R$, in this region.

2.2.4.1 Considerations of the coupling condition

A limitation of the Si/VO_2 ring resonator presented in this work is the induced optical loss in the ring resonator in its passive state (*i.e.*, with no applied voltage). The VO_2:M phase, although more optically transmissive than the VO_2:R phase, has non-negligible absorption ($\kappa = 0.3$ at 1550 nm) [43]. This absorption, in addition to loss avenues from the silicon supports and the metallic contacts, gives non-trivial optical insertion loss. Assuming negligible loss at the coupling interface between the bus waveguide and ring resonator, critically coupling (*i.e.*, perfect extinction) is achieved when the total power loss in the ring is matched to the power coupled

from the bus waveguide into the ring [37]. To increase the optical coupling from the bus waveguide into the resonator, in the work presented above, a physical coupling connection was employed between the bus waveguide and the ring resonator, shown in Figure 2.9 for a device with L_{VO_2} = 3 μm. The length of the coupling connection is labeled $L_{coupling}$.

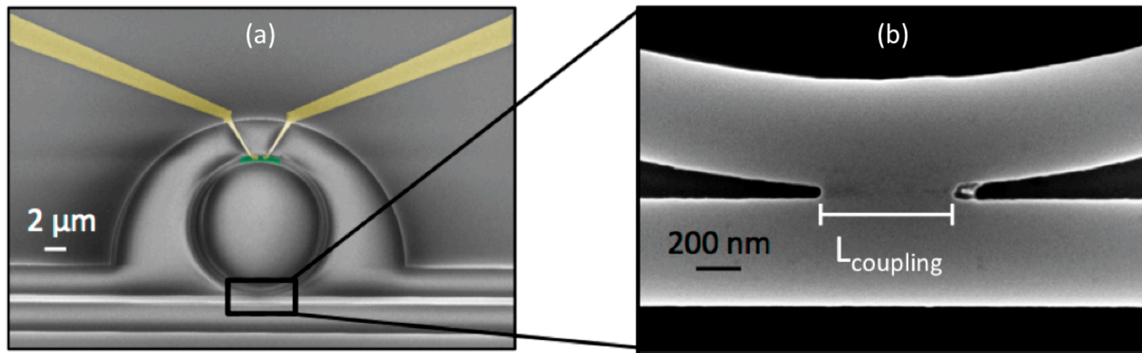

Figure 2.9. (a) SEM image of Si/VO_2 ring resonator electro-optic modulator with L_{VO_2} = 3 μm. (b) Zoomed-in SEM image of coupling area, shown in black box in (a), between the bus waveguide and ring resonator, showing the physical coupling connection between the two. The length of this coupling connection is labeled $L_{coupling}$.

For example, for the L_{VO_2} = 3 μm device characterized in Figure 2.8(b), $L_{coupling}$ = 1.25 μm. While this design method allows for maximized resonance depths in the passive state, the physical coupling condition provides an additional loss mechanism, reducing the resonator Q factor, broadening the resonance, and therefore requiring large resonance shifts (> 5 nm) to achieve substantive extinction ratios. Maintaining narrow (~ 100 nm) contact spacing to retain low voltage operation leads to more metal interacting with the optical mode, further increasing losses and broading the resonance. Consequently, realization of resonance shifts > 5 nm has required use of volumes of VO_2 that extend beyond the electrical contacts, which limits the temporal performance of the device as discussed above. In the next section, a design approach

for a Si/VO_2 electro-absorption modulator to potentially address this concern is proposed and demonstrated.

2.3 Transverse magnetic mode Si/VO_2 electro-absorption modulator

For typical silicon waveguide geometries where the waveguide width is larger than the waveguide height, the TE mode is better guided than the TM mode. For this reason, typical silicon photonic device design is for TE polarization to minimize propagation losses. However, with recent demonstrations of efficient, compact devices for polarization conversion [70, 71], components designed for TE and TM polarization can likely be integrated onto the same chip with relative ease. With this in mind, a TM mode Si/VO_2 electro-absorption modulator (*i.e.,* straight silicon waveguide with VO_2 patch on top) with the potential to operate at low voltages, high speeds, and respectable extinction ratio is proposed and demonstrated. In particular, the importance of both polarization and waveguide geometry for interaction with VO_2 are analyzed. For this, the transmission for a VO_2 patch in its VO_2:M and VO_2:R phases for four polarization/waveguide thickness combinations [(i) TE: 220 nm, (ii) TM: 220 nm, (iii) TE: 270 nm, and (iv) TM: 270 nm] was simulated (Lumerical FDTD Solutions). In the simulation, VO_2 optical constants were taken and imported from [69]. All waveguides were 500 nm wide. The VO_2 patches were placed on top of the silicon waveguide and have dimensions 500 nm (width) × 350 nm (length) × 60 nm (height). The inset in Figure 2.10(a) provides a schematic of the simulated structure. Figure 2.10(a) gives the induced optical loss (*i.e.*, summation of scattering, absorption, and reflection) when VO_2 undergoes the SMT for each waveguide geometry/polarization combination.

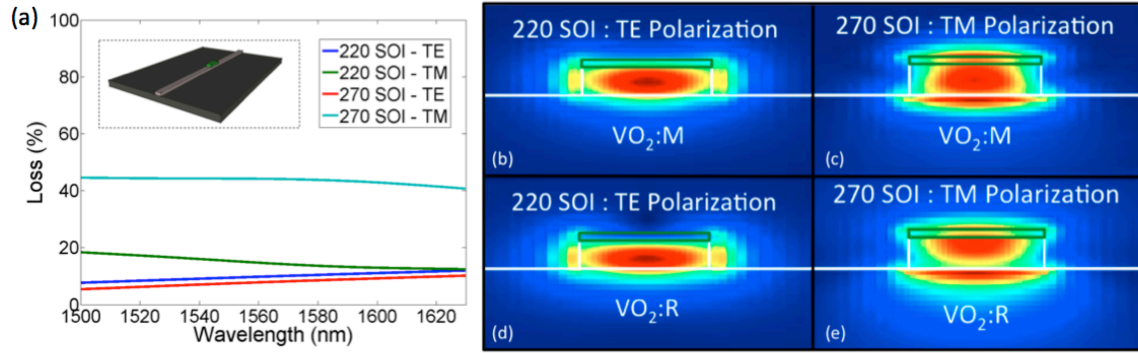

Figure 2.10. (a) Induced optical loss when VO_2 undergoes the SMT for four waveguide geometry/polarization combinations. Inset is a schematic of the simulated device design. Dark gray is SiO_2, light gray is Si, and green is VO_2. (b-e) Electric field intensity cross-sections for varying waveguide geometries, polarizations, and VO_2 phase (VO_2:M or VO_2:R). White and green lines give the outline for the Si/VO_2 structure. VO_2 is represented by the green rectangle, Si is under the VO_2, SiO_2 is the substrate, and air is cladding.

The increase in loss for TM polarization (for both 220 and 270 SOI) can be explained by the electric field mode profiles shown in Figure 2.10(b-e). Here, as a comparison, the TE and TM mode profiles for the waveguide geometry and wavelength that give the greatest loss (*i.e.*, TE: 220 SOI at 1630 nm, TM: 270 SOI at 1500 nm) are shown. Qualitatively, it is clear TM polarization has more interaction with the top of the waveguide, and therefore the VO_2. For the two cases shown in Figure 2.10(b-e), the VO_2:M cases give 82.6% and 72.5% transmission, for TE and TM polarizations, respectively. However, for VO_2:R, TM polarization gives 27.9% transmission while TE polarization gives 70.6% transmission. Therefore, TM and TE polarizations exhibit extinction ratios of 4.15 dB and 0.68 dB while both give nearly equivalent insertion loss (1.4 dB for TM, 0.83 dB for TE). This is attributed to the enhanced interaction between the optical mode and the metallic VO_2 at the Si/VO_2 interface for the TM mode.

To experimentally verify these results, a Si/VO_2 TM mode electro-absorption waveguide modulator was fabricated following processing steps similar to those outlined in Section 2.2.1.

Figure 2.11(a) shows the fully fabricated device. The silicon waveguide, in addition to silicon supports (to ensure continuous gold contacts) was formed in 270 nm SOI, and has a width of 500 nm. The VO_2 patch is of dimensions 500 nm (width) × 350 nm (length) × 80 nm (height). For both TE and TM polarizations, optical transmission was measured at no applied bias (VO_2:M) and above the switching voltage (VO_2:R). Methods of polarization control and characterization can be found in Appendix A.1. Extinction ratio for both polarizations is shown in Figure 2.11(b), demonstrating higher extinction ratio for TM polarization consistent with expectations from the simulations.

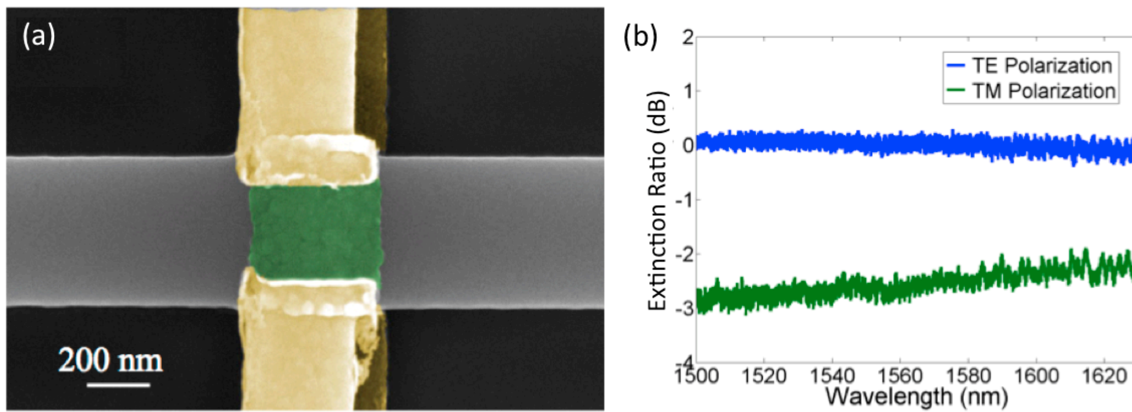

Figure 2.11. (a) SEM image of fully fabricated Si/VO_2 TM mode electro-absorption waveguide modulator. Si, SiO_2, VO_2, and Au are light gray, dark gray, green (false colored), and gold (false colored), respectively. (b) For TE and TM polarizations, difference in optical transmission with no voltage applied (VO_2:M) and a voltage greater than the switching voltage applied (VO_2:R), plotted as extinction ratio.

At 1500 nm, TM polarized light shows an extinction ratio of ~ 3 dB, demonstrating promise that this geometry modification and polarization selection has the potential to improve the extinction ratio. Additional waveguide optimization is expected to give further improvement, as presented in simulation in Ref. [58]. In the geometry shown in Figure 2.11(a), since the VO_2 patch

necessary to achieve the demonstrated extinction is between the contacts, this geometry has the potential for temporal operation that pushes the intrinsic limits of VO_2. Unfortunately, high-speed measurements resulted in failure of this device. The cause for failure is unclear, but it may be a result of the thermal environment from repeated electrical testing.

2.4 Conclusions

In this chapter, Si/VO_2 ring resonator electro-optic modulators were fabricated and characterized. Experimental results reveal the role of VO_2 patch size in device performance. In a device with a 3 μm long VO_2 patch, a steady-state extinction ratio of 10 dB was measured. However, in high speed testing of this device, long recovery times are observed mainly due to Joule heating contributions and the slow relaxation time of the VO_2:R phase. By reducing the VO_2 patch size from 3 μm to 1 μm, in response to a 10 ns, 2.5 V voltage pulse, an extinction ratio of ~ 1.5 dB that appears to recover to baseline optical transmission after 10 ns is demonstrated. While this is a slight improvement to previous demonstrations of Si/VO_2 electro-optic modulators, this design poses challenges. In particular, for electrical actuation of the SMT, additional losses in Si/VO_2 ring resonator from implementation of additional design features (silicon supports, metallic contacts) suggest it may be difficult to achieve the device performance shown in a thermo-optic or all-optical geometry [56, 64] in an electro-optic geometry. With this in mind, Si/VO_2 electro-absorption designs may be the most suitable geometry. Here, the importance of waveguide geometry and polarization selection was demonstrated in an electro-absorption geometry, showing enhanced performance for TM polarized light for a 500 nm × 270 nm silicon waveguide coated with a 350 nm (long) × 500 nm (wide) × 80 nm (thick) VO_2 patch. Further optimization of this design may provide an avenue for large extinction ratios using small

patches of VO_2, pushing toward Gb/s operation. In Chapter 4, an additional proposed Si/VO_2 geometry for TE polarized light that may also achieve this goal is presented.

Chapter 3

3. Platforms for Si/VO_2 all-optical modulation

3.1 Introduction

In light of the discussion of the extent to which photonic components can replace their electronic counterparts in entirety for information processing [5] and storage [6, 7], here, Si/VO_2 photonic platforms with the potential for all-optical control are explored. In particular, the demonstration of a geometry whereby VO_2 is placed within a silicon waveguide, therefore enhancing optical interaction with VO_2 and giving large extinction ratios for short device lengths, is highlighted. The optical performance of this structure is characterized by thermally actuating the SMT of the embedded VO_2 patch. The potential implementation of this structure as an all-optical modulator with in-plane excitation is discussed. In addition, based off the demonstration in Chapter 2 of enhanced interaction with VO_2 for TM polarization, experimental results of a TM mode Si/VO_2 ring resonator device, and its potential implementation as an all-optical modulator with out-of-plane excitation, are presented.

3.2 VO_2 embedded silicon waveguide

In this section, a geometry to more effectively utilize the large optical tunability of VO_2 is theoretically and experimentally presented. By integrating VO_2 within a silicon waveguide, the interaction of the guided mode in silicon with VO_2 is maximized. Figure 3.1 shows cross sectional electric field intensity profiles of light propagating through a VO_2 coated silicon waveguide [Figure 3.1(a)] and through a silicon waveguide with VO_2 embedded inside of it [Figure 3.1(b)], demonstrating the increased interaction with VO_2.

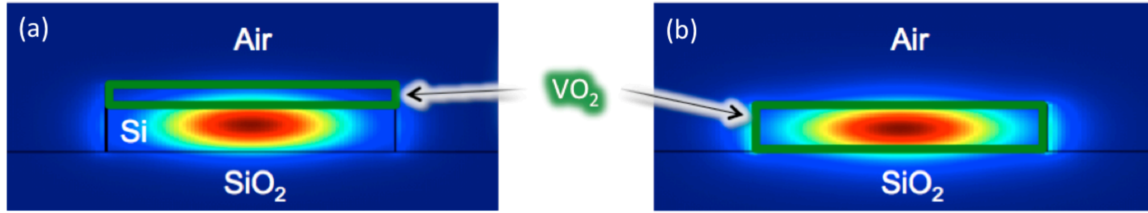

Figure 3.1. Electric field intensity optical mode profiles (Lumerical MODE Solutions) for the TE mode propogating through (a) a silicon waveguide coated with a patch of VO_2 and (b) a waveguide where the guiding material is VO_2. In both cases, VO_2 is outlined in green, and the enhanced interaction with the optical mode for (b) is clearly demonstrated.

As discussed in Section 1.3.1, ultrafast studies on VO_2 thin films have revealed unique ultrafast dynamics [44-51], demonstrating the SMT and MST of VO_2 can be accessed on ~ femtosecond and ~ 1-10 picosecond times, respectively. The geometry proposed here may provide a platform where those same ultrafast dynamics can be accessed within a silicon photonic all-optical modulator. With the demonstration of optically inducing the SMT with near infrared wavelengths (*e.g.*, 1650 nm) [72], it is expected the SMT can be actuated by pump light within the silicon waveguide. In order to explore the feasibility of this geometry, in this section, silicon waveguides with embedded VO_2 sections of variable length are simulated, fabricated, and characterized. Additionally, it is expected this design will initiate embedded integration of VO_2 within silicon photonic devices, in particular for electro-optic modulation, and will be discussed in Section 4.2.2.

3.2.1 Device Simulation

All simulations were performed using three-dimensional FDTD analysis (Lumerical FDTD Solutions). Simulations were run with an auto non-uniform meshing parameter of 6 and perfectly matched layer boundary conditions for the fundamental TE mode source. The simulated structure

consisted of a silicon ridge waveguide on a silicon dioxide substrate with a VO_2 patch of the same cross sectional dimensions embedded within the silicon waveguide, as shown in Figure 3.2(a). The width and height of both the waveguide and VO_2 patch were 700 nm and 220 nm, respectively. The length of the VO_2 patch in the direction of propagation (L_{VO_2}) was varied from 0 to 1000 nm in steps of 100 nm. Transmission through each waveguide was calculated using frequency-domain field and power monitors; both the semiconducting and metallic states of VO_2 were considered. Optical constants for VO_2 were taken from [43] and imported into Lumerical for the simulations while optical properties of silicon and silicon dioxide were taken from Lumerical Solutions' material database [73]. Figure 3.2(b) shows transmission at 1550 nm as a function of L_{VO_2} for the hybrid waveguide when the VO_2 patch is in its semiconducting (blue circles) and metallic (red squares) phases. When the VO_2 patch is in the semiconducting phase, there is a nearly perfect refractive index match between VO_2 and silicon, and reflection at the Si/VO_2 interface is simulated to be less than 1%. Therefore, transmission through the VO_2 embedded silicon waveguide is dictated by absorption in VO_2 when VO_2 is in the semiconducting phase. Accordingly, the curve fit for the transmission data is a single exponential function obeying Beer's law for $\kappa = 0.31$, which is in good agreement with the optical properties of semiconducting VO_2 films at 1550 nm. The curve fit for the transmission data with metallic VO_2 patches does not simply follow Beer's law for light transmitted through an equivalent thickness metallic VO_2 thin film because the spread in the optical mode profile as light passes through the low refractive index metallic VO_2 section of the waveguide causes a significant portion of the mode to propagate in the cladding region outside the lossy VO_2 patch. In depth consideration of transient modal propagation in this VO_2 embedded silicon waveguide geometry is presented in Section 4.3.3.

For the VO_2 embedded silicon waveguide, calculated insertion loss (IL) and extinction ratio (ER) are presented in Figure 3.2(c,d) and are given by

$$IL = -10 \times \log\left(\frac{T_{Si}}{T_{Si-semiconductingVO_2}}\right) \quad (4)$$

and

$$ER = -10 \times \log\left(\frac{T_{Si-semiconductingVO_2}}{T_{Si-metallicVO_2}}\right) \quad (5)$$

where T_{Si}, $T_{Si-semiconductingVO_2}$, and $T_{Si-metallicVO_2}$ are the optical transmission through a silicon waveguide with no VO_2, a silicon waveguide with embedded semiconducting VO_2, and a silicon waveguide with embedded metallic VO_2, respectively. The trend in extinction ratio as a function of VO_2 length that shows a maximum extinction ratio for a VO_2 patch length of 400 nm can be explained by considering the saturation in the transmission intensity of light through the VO_2 embedded silicon waveguide for metallic VO_2 patch lengths greater than about 400 nm. Taking into account both extinction ratio and insertion loss, Figure 3.2 suggests that a favorable geometry is a 200 nm embedded VO_2 patch, which enables nearly 14 dB extinction ratio with approximately 2 dB insertion loss.

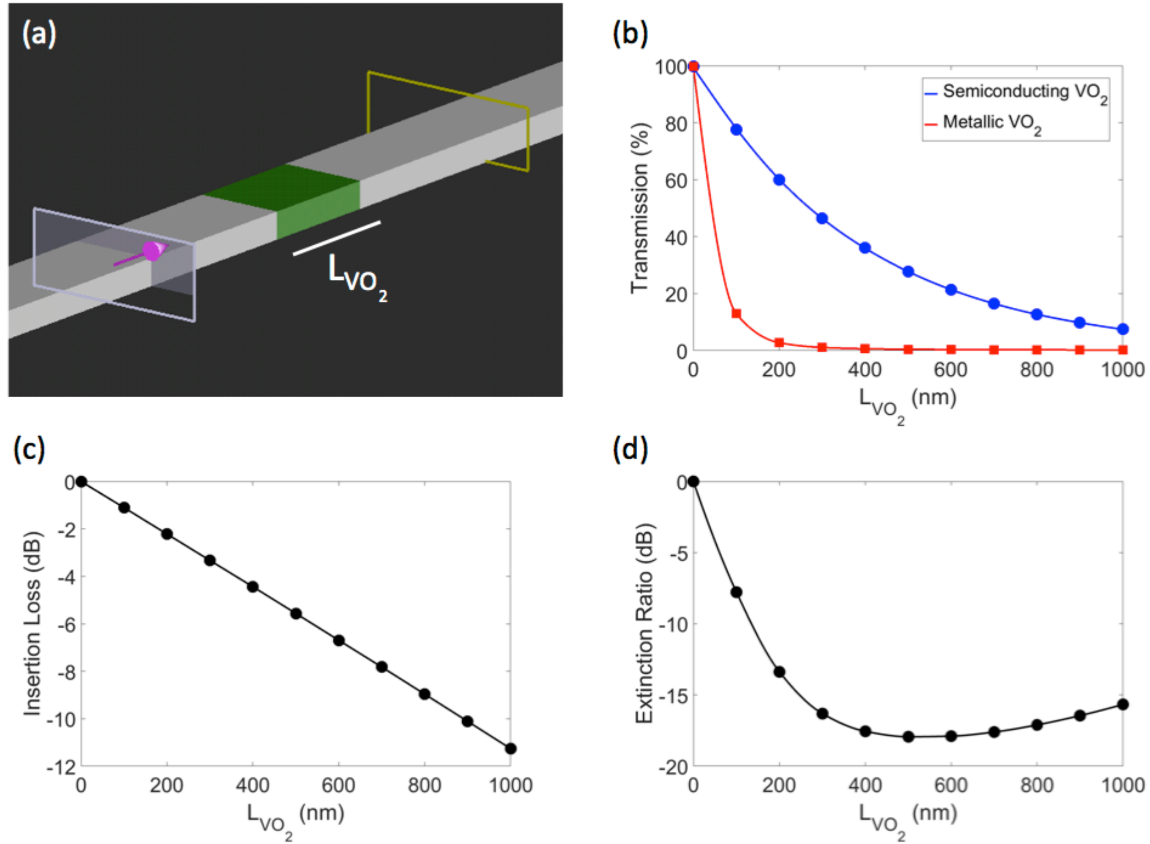

Figure 3.2. (a) Schematic for simulation of VO_2 embedded silicon waveguide shown in gray (silicon) and green (VO_2) on a silicon dioxide (dark gray) substrate. The purple arrow surrounded by the gray box and yellow box represent the optical source and monitor, respectively. For the fundamental TE mode, (b) simulated transmission as a function of L_{VO_2} through VO_2 embedded silicon waveguide with VO_2 in its semiconducting (blue circles) and metallic (red squares). Optical properties of VO_2 are taken from [43]. (c) Insertion loss and (d) extinction ratio of VO_2 embedded silicon waveguide as a function of L_{VO_2}, calculated from transmission data shown in (b). With the exception of the semiconducting VO_2 curve fit in (b) which is a single exponential fit, the corresponding curve fits in (b), (c), and (d) serve as guides to the eye. Figures reprinted with permission from [74]. © 2017 OSA.

3.2.2 Device Fabrication

Fabrication procedures very similar to those outlined in Section 2.2.1 were followed to fabricate the VO_2 embedded silicon waveguides and are shown in Figure 3.3. In particular, the first step to use to define the base silicon photonic structure was identical. Cartoon schematics of

the device after development, etch, and the resist strip are shown in Figure 3.3(a,b). In addition, similar to the second and third lithography steps in Section 2.2.1, localized VO_2 deposition in the trenches was achieved by opening windows of the requisite dimensions using electron beam lithography (Raith eLine). This step was performed in two identical iterations to ensure complete O_2 diffusion during the annealing step to form stoichiometric VO_2. For both steps, dosing parameters (dose, aperture, step size, voltage) of 400 $\mu C/cm^2$, 30 μm, 10 nm, and 20 kV were used. The results of each VO_2 deposition are shown in Figure 3.3(c,d). Figure 3.3(d) shows a cartoon schematic assuming perfect fabrication. In reality, there are imperfections, and the morphology and thickness of the deposited VO_2 films embedded in waveguides with differing trench lengths is discussed in Section 3.2.3.1.

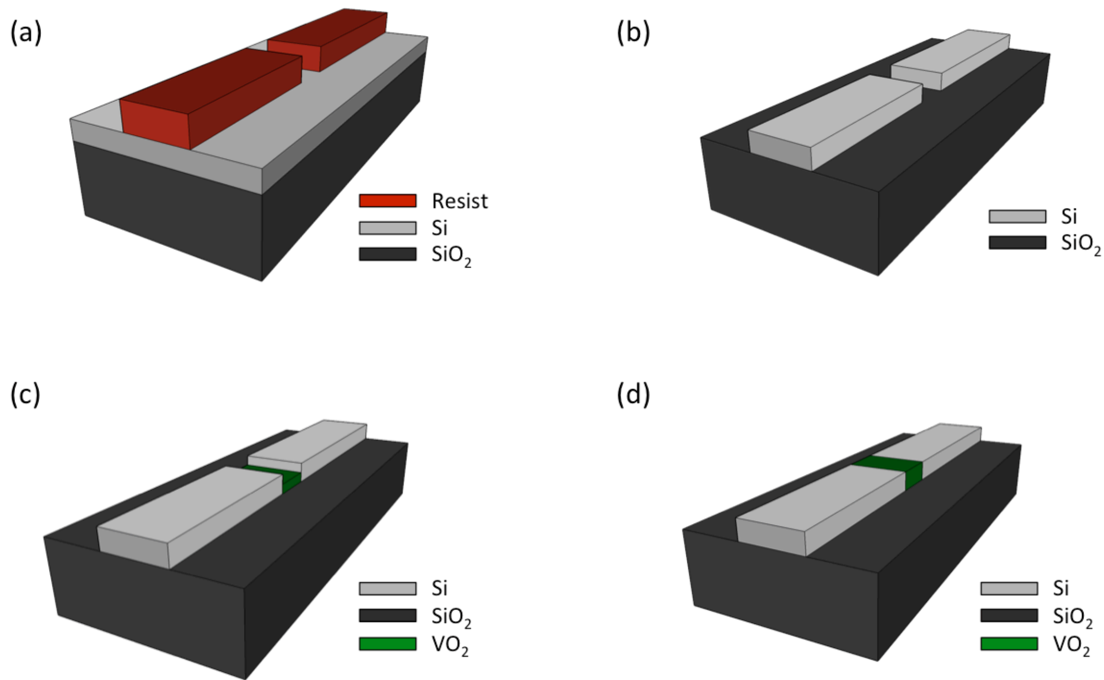

Figure 3.3. Multilayer lithography patterning of VO_2 embedded silicon waveguide. In each schematic, Si, SiO_2, VO_2, and the resist are light gray, dark gray, green, and red, respectively. (a) Patterning and development of resist in preparation of etching of silicon photonic structure. (b) Silicon waveguide with trench after etching and subsequent liftoff of resist. (c,d) VO_2 embedded silicon waveguide resist patterning and (c) first and (d) second deposition of VO_2, including liftoff of resist after each deposition.

For characterization of the VO_2 embedded silicon waveguides, the complete design, shown in Figure 3.4, included bifurcated waveguides and integrated resistive heaters. For the bifurcated waveguides, the upper waveguide in each pair includes the VO_2 embedded silicon waveguide structure (Figure 3.4 – left inset), while the lower waveguide is a standard, continuous ridge waveguide for control measurements (Figure 3.4 – right inset). The resistive heaters, serving to thermally actuate the SMT, are false colored gold in Figure 3.4 and were fabricated adjacent to the waveguides using electron beam lithography patterning (Raith eLine), thermal evaporation of a 5 nm Cr adhesion layer and a 120 nm Au layer, and liftoff. The integrated heaters were patterned using an aperture of 100 μm to reduce the write time of the electron beam exposure.

Additionally, another set of bifurcated silicon waveguides was fabricated with VO_2 deposited on top of the control waveguides in order to compare their performance with the VO_2 embedded silicon waveguides. These results are presented in Section 3.2.7. All devices were cleaved to access both input and output waveguides for fiber coupled measurements. The post-cleaved devices measured ~ 3 mm in length.

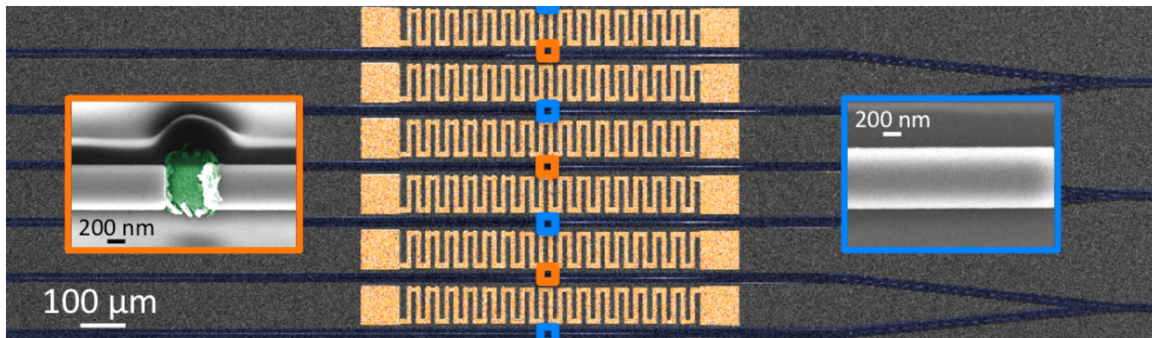

Figure 3.4. SEM image of bifurcated silicon waveguides (false colored navy) and integrated heaters (false colored gold). In the center of the figure, the small boxes highlight VO_2 embedded silicon waveguides (orange) and control waveguides (light blue). The left inset with orange outline shows an SEM image of the VO_2 embedded silicon waveguide. For clarity, VO_2 is false colored green. The right inset outlined in light blue shows the control silicon waveguide. Figure adapted and reprinted with permission from [74]. © 2017 OSA

3.2.2.1 Design parameters for integrated heaters

Figure 3.5 shows zoomed-in SEM images of the integrated resistive heaters. The designed heaters consist of two square pads of side dimension (L_{pad}) 70 µm to be accessed by electrical probes. These two blocks are connected by sixteen pairs of a repeating structure (shown in inset of Figure 3.5). This repeating structure has a gold wire width (w_{Au}) of 8 µm, gold wire length (L_{Au}) of 65 µm, and the gap between gold wires (w_{gap}) is 9 µm. The edge of the gold wires is ~ 8

μm from the edge of the silicon dioxide trench which defines the silicon waveguide. The silicon dioxide trench is 8 μm wide in the case of the bifurcated waveguides.

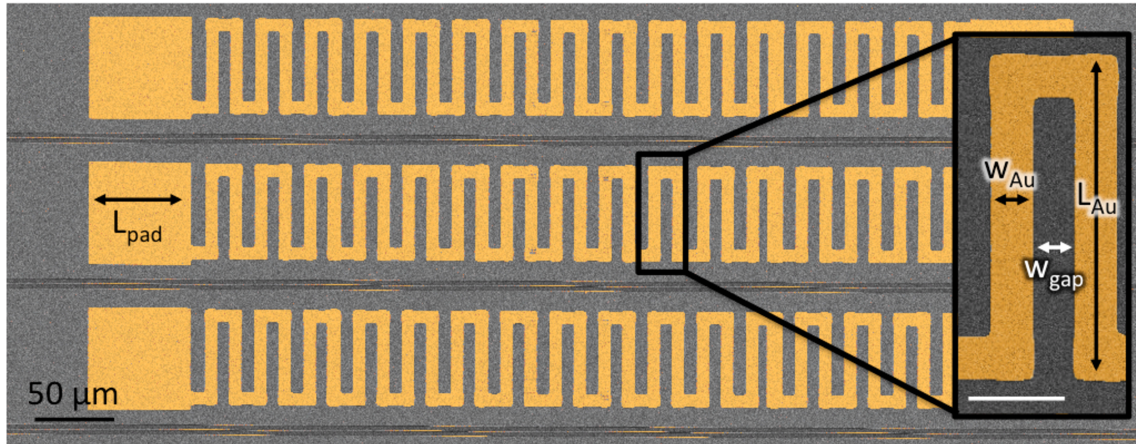

Figure 3.5. SEM image of the integrated resistive heaters. The metallic components are false colored gold. Any gold coloring appearing on the waveguide surfaces is an artifact of the false coloring method used for image processing. The right inset shows a zoomed-in SEM of a unit cell of the integrated heater. The gold wire width, gold wire length, and gap between gold wires are labeled w_{Au}, L_{Au}, and w_{gap}, respectively. The white scale bar in the bottom left of the inset is 20 μm.

3.2.3 Device characterization

3.2.3.1 Characterization of waveguides

The VO_2 embedded silicon waveguides were characterized by tilted SEM imaging and atomic force microscopy (AFM). As shown in Figure 3.6(a), the VO_2 deposition was not sufficient to completely fill the trenches. The shorter trenches with higher aspect ratio of depth to width had thinner VO_2 films compared to the longer trenches, most likely due to known challenges with depositing material into high aspect-ratio holes. Atomic force microscopy measurements for a waveguide with L_{VO_2} = 1000 nm suggest that the VO_2 film thickness in the lowest aspect-ratio trench is approximately 180 nm [Figure 3.6(b,c)], which is less than the

220 nm height of the silicon waveguide. The deposition of VO_2 on top of the silicon waveguide at one end of the trench [Figure 3.6(a)] was due to a slight misalignment of the resist window during fabrication. Atomic force microscopy measurements also revealed that the VO_2 patches on top of the control waveguides have a thickness of approximately 210 nm, which is slightly less than the thickness (250 nm) of a 100 μm × 100 μm VO_2 film patterned adjacent to the waveguides. This difference is expected to be due to shadowing effects of the resist.

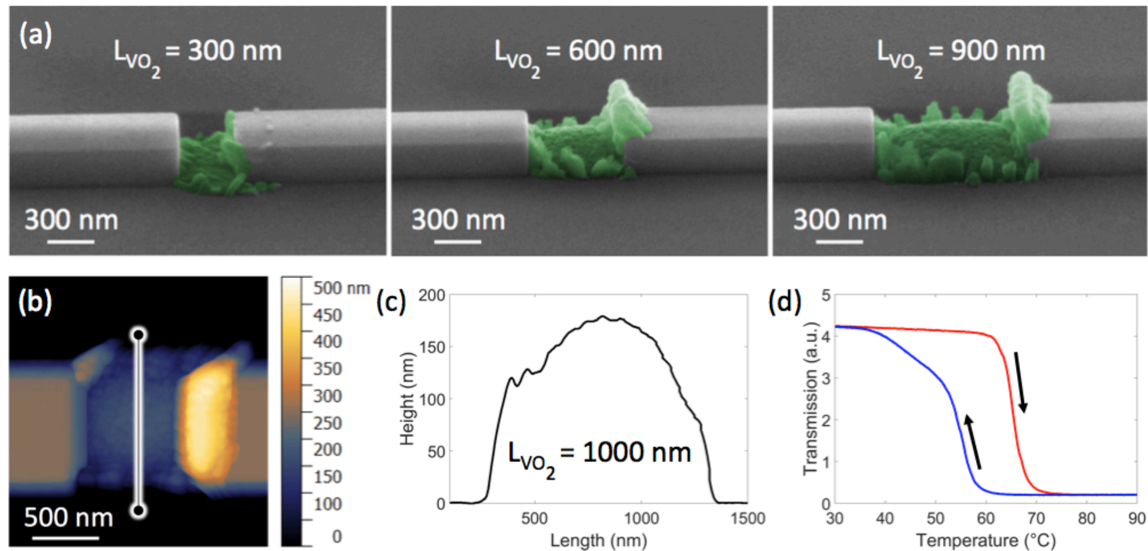

Figure 3.6. a) Tilted SEM images of VO_2 embedded silicon waveguides with L_{VO_2} = 300, 600, and 900 nm. VO_2 is shown in false colored green. (b) AFM image of VO_2 embedded silicon waveguide with L_{VO_2} = 1000 nm. Vertical profile of line cut (black line outlined in white) is presented in (c), showing a VO_2 thickness of ~ 180 nm within the trench. (d) Temperature-dependent transmission measurements on a thin film VO_2 witness sample on a glass substrate. The red and blue curves show transmission with increasing and decreasing temperature, respectively. Figures reprinted with permission from [74]. © 2017 OSA.

3.2.3.2 Characterization of VO_2

To verify the optical switching properties of VO_2, temperature-dependent transmission measurements were performed on a thin film of VO_2 on a glass substrate that underwent identical processing steps to the VO_2 embedded silicon waveguides. With the exception that transmission is measured instead of reflection, the experimental setup used for this characterization is identical to that described in Section 2.2.2.1. Figure 3.6(d) shows the measured transmission through the VO_2 film for both heating (red) and cooling (blue) curves. As the temperature is increased, transmission through the film decreases due to the increased reflection and absorption of the VO_2 as it is undergoes the SMT. As the VO_2 film temperature returns to room temperature, transmission increases to its original value as the VO_2 undergoes the MST. The onset of the SMT is measured to be near 65°C, typical for VO_2 films.

3.2.4 Experimental setup

Fiber-coupled transmission measurements were carried out using the Santec Swept Test System STS-510 software package with a tunable laser (Santec TSL-510) and power meter (Newport 2936-C). Primarily TE polarized (98% TE; 2% TM) near infrared light (1500-1630 nm) was coupled into and out of the waveguides using lensed tapered fibers (OZ Optics). An infrared camera (Sensors Unlimited SU320M) was used to aid alignment. Free space polarization control of the optical input was maintained using a linear polarizer and half wave plate. Transverse electric (TE) polarization was used for all measurements. Methods of polarization control and characterization can be found in Appendix A.1. As a modification to the experimental setup used in Section 2.2.3.1, to more rapidly characterize the VO_2 embedded silicon waveguides, an integrated electrical probe station was constructed within the existing

fiber coupled optical setup to actuate the patterned integrated on-chip heaters shown in Figure 3.5. This probe station provides high precision (can easily access patterned electrical pads between waveguides which are spaced by 100 µm), high durability (eliminated waveguide damage caused during wire bonding process), and rapid testing capability as there is no need for wire bonding or use of a custom sample holder. An image of the experimental setup, including the electrical probe station, is shown in Figure 3.7. Figure 3.7(b) shows a zoomed-in image of the electrical probes integrated into the fiber-coupled setup. The positioning of these electrical probes is controlled by individual XYZ stages. With this control, electrical connections to square metal pads with lateral dimension as small as ~ 50 µm can be accomplished. Figure 3.7(c) shows a display monitor readout from a Sensors Unlimited SU320M camera image collected through a Mitutoyo M Plan Apo NIR 20X microscope objective. The image, showing the left electrical probe above the integrated heaters and VO_2 embedded silicon waveguides, serves to show how the electrical probes can be used to make electrical connection to photonic devices.

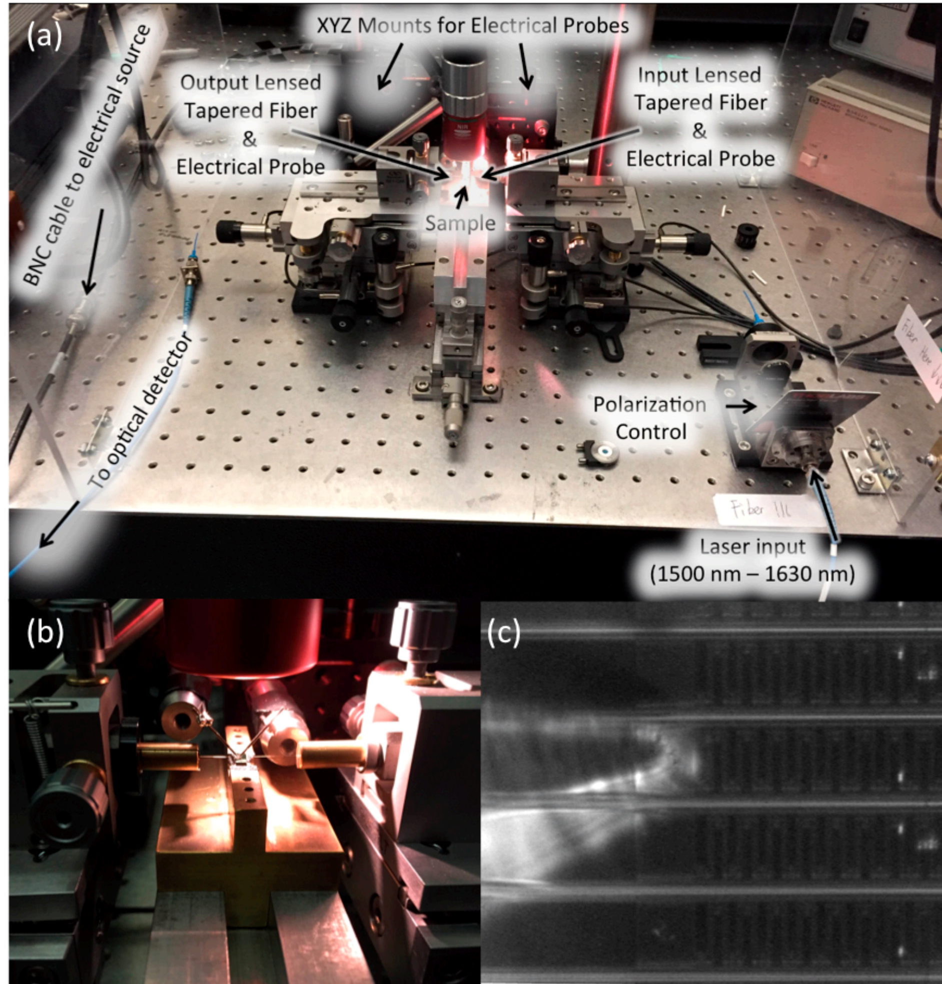

Figure 3.7. Fiber-coupled optical setup, including integrated electrical probe station, for active characterization of VO_2 embedded silicon waveguides. (a) Image of entire experimental setup, showing optical input/output, polarization control, and components for electrical probing of photonic devices. (b) Zoomed-in image on the sample, showing optical coupling to and from the pohotonic device via optical fiber in addition to electrical connections from the two electrical probes. (c) Image taken from a monitor reading an image from a Sensors Unlimited SU320M camera through a Mitutoyo M Plan Apo NIR 20X microscope objective. This image shows the left electrical probe just above one of the contact pads of the resistive heaters. The horizontal lines represent the VO_2 embedded silicon waveguides.

3.2.5 Results and discussion

3.2.5.1 Transmission results

High contrast Fabry-Perot fringes were observed in the transmission spectra [thin lines in Figure 3.8(a)], which are attributed to reflections from stitching errors in the waveguides that occurred during the first step of electron beam lithography, roughness at the Si-VO_2/Si-air interfaces, and the bifurcated waveguide design. These high contrast Fabry-Perot fringes were also observed in the continuous, control silicon waveguide, indicating that the fringes are not primarily caused by the VO_2 embedded design. To minimize the effect of the Fabry-Perot fringes, the data were smoothed with a moving average across 10 nm for each data point (*i.e.*, 5 nm to each side of the data point, totaling 10,001 data points). An example of this smoothing is shown by the thick lines in Figure 3.8(a). These smoothed curves were used for all insertion loss and extinction ratio calculations. Temperature-dependent transmission measurements were carried out by varying the applied electrical power supplied to the resistive heaters. Figure 3.8(b) shows the extinction ratio, which is reported based on the ratio of transmission through the VO_2 embedded silicon waveguide with and without an applied voltage, for varying applied voltages. The SMT of VO_2 is initiated with approximately 0.73 W applied, as indicated by the change in extinction ratio, and is completed with 1.41 W applied. Accordingly, for all calculations in the next section, we assume that VO_2 is in the semiconducting state when no electrical power is applied to the resistive heaters and VO_2 is in the metallic state when 1.41 W is applied. Since VO_2 is fully switched at ~ 80°C, the VO_2 patch must be at or above that temperature when the maximum extinction ratio is achieved. The temperature is likely much higher near the heater since the heat must be transferred through SiO_2 before reaching the VO_2 patch. Figure 3.8(b) also demonstrates the broadband (exceeding 100 nm) operation of the VO_2 embedded silicon

waveguides as expected from simulation due to the relatively small variation in optical constants of VO_2 from 1510-1620 nm.

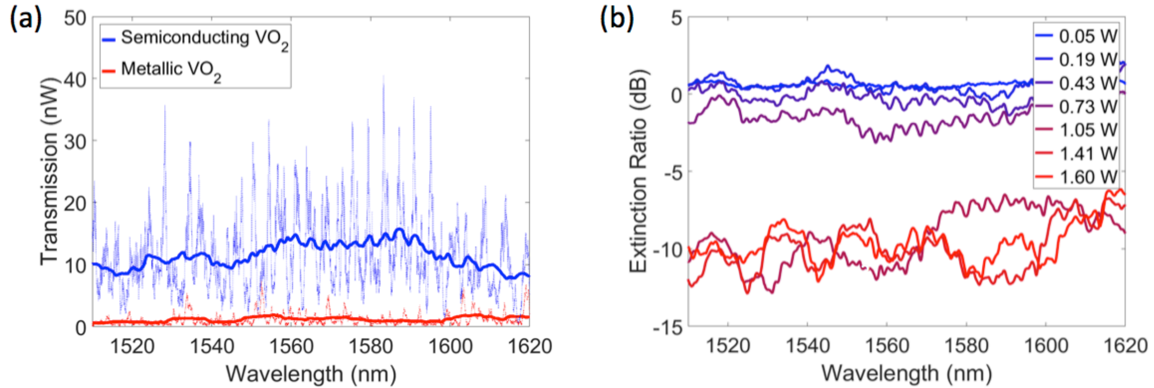

Figure 3.8. (a) Raw (thin lines) and smoothed (thick lines) data for transmitted power through a VO_2 embedded silicon waveguide with L_{VO_2} = 600 nm. Blue curves correspond to 0 W applied electrical power (*i.e.*, VO_2 in semiconducting state) and red curves correspond to 1.41 W applied electrical power (*i.e.*, VO_2 in metallic state). (b) Extinction ratio of same sample for various applied electrical powers, calculated from the smoothed spectra. Figures reprinted with permission from [74]. © 2017 OSA.

After carrying out multiple transmission measurements on each of the VO_2 embedded silicon waveguides with different trench lengths, trends in the transmitted intensity, insertion loss, and extinction ratio as a function of L_{VO_2} were analyzed at a wavelength of 1550 nm, as shown in Figure 3.9. Error bars in Figure 3.9 were calculated based on the standard deviation of multiple (> 3) measurements on each device. The experimental results deviate from the simulation data presented in Figure 3.2(b) that assume complete filling of VO_2 in the trench because the fabricated structures have only partially filled VO_2 trenches (seen in Figure 3.6). Accordingly, the simulation results presented alongside the experimental data in Figure 3.9 assume VO_2 thicknesses from 90 nm for L_{VO_2} = 100 nm to 180 nm for L_{VO_2} = 1000 nm, with a linear interpolation between these values (*i.e.*, 10 nm increase in VO_2 height per 100 nm increase in

L_{VO_2}). As in Figure 3.2, for all simulation results shown in Figure 3.9, the optical properties of VO_2 were taken from [43] and imported into Lumerical. Our experimental data in Figure 3.9 show good agreement with the simulated curves for silicon waveguides with partially filled VO_2 trenches. The deviation between experiment and simulation for extinction ratio [Figure 3.9(d)] can be attributed in large part to the slightly higher measured transmission of the waveguide compared to simulation when the VO_2 patch is in the metallic state. The data in Figure 3.9 reveal a clear tradeoff between insertion loss and extinction ratio. Due to the absorption of VO_2 in the semiconductor state, longer VO_2 filled trenches lead to higher insertion losses. At the same time, the longer VO_2 filled trenches allow more reflection, scattering, and absorption of light when VO_2 is in the metallic state, leading to a larger extinction ratio. For the partially filled VO_2 embedded silicon waveguide with L_{VO_2} = 500 nm, extinction ratio of 9.7 ± 0.8 dB with a corresponding insertion loss of 6.5 ± 0.9 dB is demonstrated.

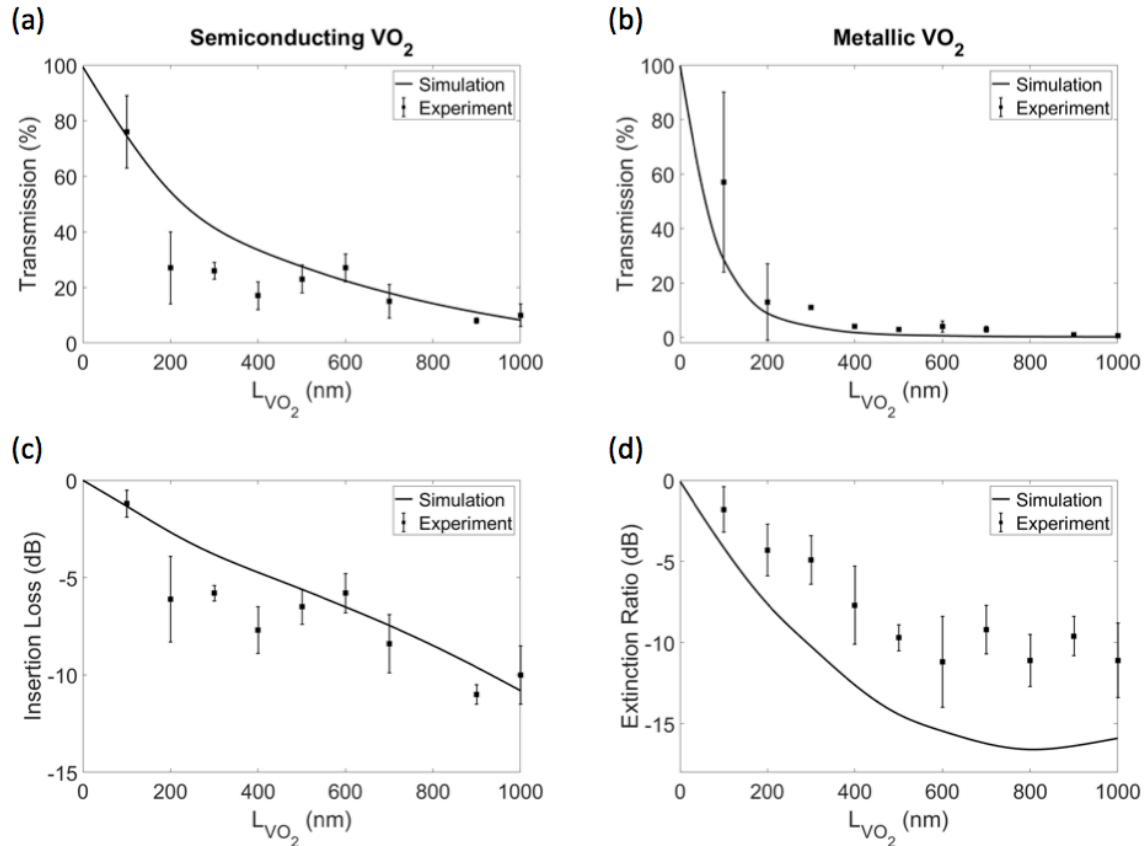

Figure 3.9. Measured transmission through VO_2 embedded silicon waveguide as a function of L_{VO_2}, normalized to transmission through a reference silicon waveguide, for VO_2 in its (a) semiconducting and (b) metallic state. Calculated (c) insertion loss and (d) extinction ratio of VO_2 embedded silicon waveguide as a function of L_{VO_2} based on measured data in (a) and (b). The solid curves present Lumerical simulation results (VO_2 optical properties from [43]) that assume partial VO_2 filling of the silicon trench, as described in Section 3.2.5.1. Figures reprinted with permission from [74]. © 2017 OSA.

As the primary focus of this work was to demonstrate a nanophotonic platform for all-optical modulation, the integrated heater design was not optimized for high-speed or low-power operation. With an optimized heater design, it is expected this platform will be able to achieve operation with response times of order μs, commensurate with what has been demonstrated in previous work with VO_2 optical switches [59].

3.2.5.2 Transmission results for non-bifurcated waveguides

Additional waveguide samples without the bifurcated design were fabricated and characterized to help elucidate the cause of the fringes shown in Figure 3.8(a). Figure 3.10 shows the optical response of a non-bifurcated VO_2 embedded silicon waveguide with L_{VO_2} = 500 nm. In comparison with Figure 3.8, the Fabry-Perot fringes are largely reduced. While it is unclear if this reduction is due to reduced stitching error, removal of the bifurcated design, or another variable, it does provide further evidence the Fabry-Perot fringes shown in Figure 3.8 are not an intrinsic property of the VO_2 embedded silicon waveguide design. In addition, Figure 3.10(b) shows that without any data averaging, for almost all wavelengths from 1500 nm – 1630 nm, the exhibited extinction ratio is ≥ 10 dB. Across this wavelength range, the average extinction ratio is 15 dB.

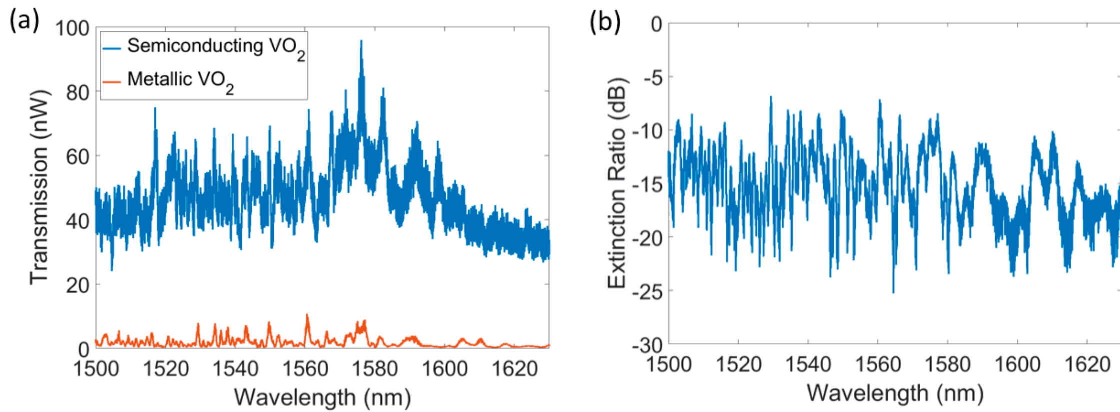

Figure 3.10. (a) Transmission through a VO_2 embedded silicon waveguide with L_{VO_2} = 500 nm in a non-bifurcated device geometry for semiconducting (blue) and metallic (orange) VO_2. (b) Measured extinction ratio corresponding to the data in (a), without any data averaging.

3.2.6 Considerations of fabrication imperfections

Motivated by the work above, to better understand how the modulator performance will be affected by imperfect fabrication (*e.g.*, not fully filling the waveguide with VO_2), Si/VO_2 embedded waveguide modulators with L_{VO_2} = 200 nm and variable VO_2 thickness were simulated in a three-dimensional Lumerical FDTD Solutions simulation. Vanadium dioxide film heights (h_{VO_2}) from 0 nm to 220 nm, in 20 nm steps, were calculated in the simulations. The device geometry for the case of h_{VO_2} = 220 nm is shown in Figure 3.2(a). For an incident wavelength of 1550 nm, Figure 3.11(a) shows transmission, absorption, and reflection for the Si/VO_2 embedded waveguide when VO_2 is in the semiconducting and metallic states as a function of h_{VO_2}. To understand the transmission, absorption, and reflection curves in Figure 3.11(a), cross section electric field intensity profiles were taken at the center of the VO_2 section of the modulator considering both semiconducting and metallic VO_2, as shown in Figure 3.11(b) and Figure 3.11(c), respectively, for different values of h_{VO_2}. In the semiconducting state, for decreasing h_{VO_2}, there is less modal overlap with the VO_2, resulting in less absorption, as seen in Figure 3.11(a). However, for the semiconducting state, transmission is relatively constant (0.4 – 0.54) across all VO_2 heights. This is because for small VO_2 thicknesses ($h_{VO_2} < \sim$ 60nm), there is significant reflection due to the large impedance mismatch between the silicon-air interface, while for larger VO_2 thicknesses, the impedance mismatch is reduced, which decreases reflection, but absorption is increased. Considering transmission in the metallic state, for decreasing h_{VO_2}, more of the optical mode is pushed outside of the VO_2, giving less interaction with the metallic VO_2 and resulting in higher transmission. At larger values of h_{VO_2}, above 100 nm, reflection and absorption from the VO_2 dominate, giving transmission of less than 10% of the incident power. Figure 3.11(d) demonstrates the effect of VO_2 thickness on insertion loss

and extinction ratio. Insertion loss is not strongly affected by VO_2 thickness, consistent with the discussion above for the relatively constant optical transmission through the modulator with semiconducting VO_2. Due to this relatively constant optical transmission when VO_2 is in the semiconducting state, extinction ratio is dictated primarily by the optical transmission of metallic VO_2. Therefore, since optical transmission through metallic VO_2 is significantly reduced with increasing h_{VO_2}, extinction ratio increases with increasing h_{VO_2}, as expected.

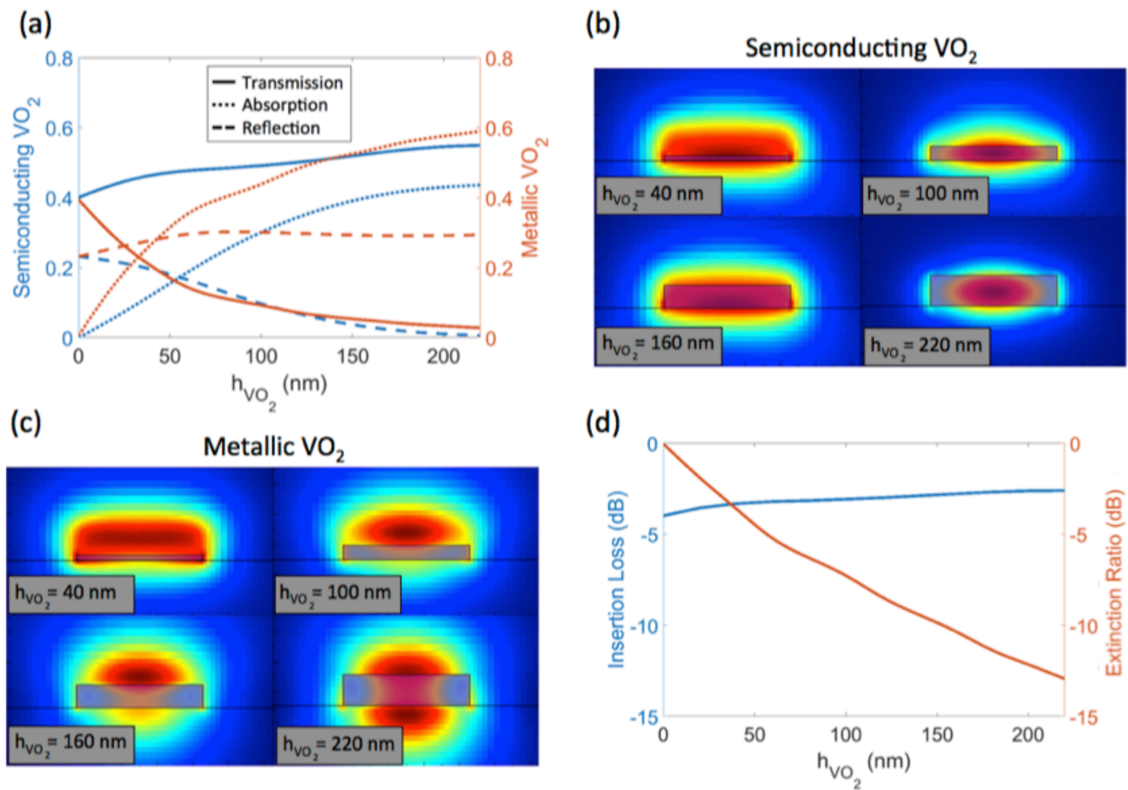

Figure 3.11. (a) Transmission, absorption, and reflection for VO_2 embedded silicon waveguide with the embedded VO_2 in the semiconducting (blue) and metallic (orange) state as a function of VO_2 thickness. (b,c) Electric field intensity profile of optical mode at the center of the modulator (*i.e.*, cutting through the VO_2 section), considering (b) semiconducting and (c) metallic VO_2 for h_{VO_2} = 40, 100, 160, and 220 nm. The transparent purple section represents the VO_2. (d) Insertion loss and extinction ratio for the Si/VO_2 all-optical modulator as a function of VO_2 thickness. Figures reprinted with permission from [75]. © 2017 SPIE.

3.2.7 Comparison of VO_2 placement location

To demonstrate the advantage of placing the VO_2 patch within the silicon waveguide instead of on top of the waveguide, a direct experimental comparison was carried out, shown in Figure 3.12. As expected, the integrated geometry provides a larger extinction ratio for all VO_2 patch lengths due to the improved interaction of the guided mode with the VO_2. Here, the reader is reminded that the waveguides were processed in an identical manner (even though the resulting VO_2 thicknesses were slightly different as discussed in Section 4.1) to isolate the effect of the location of the VO_2 patch. However, prior work suggests that an optimized waveguide geometry may be able to further improve the extinction ratio and insertion loss metrics. Using a Si/VO_2 rib waveguide design that supports a delocalized TE mode, 12 dB extinction with 5 dB insertion loss was reported with a 1000 nm long patch of VO_2 on top of the Si waveguide while 4 dB extinction was reported for a 500 nm long VO_2 patch [59]. For our design presented in Figure 3.2 which assumes complete filling of VO_2, our simulated results with L_{VO_2} = 200 nm show extinction ratio and insertion loss of 13.8 dB and 2.2 dB, respectively. Therefore, with improved silicon waveguide design, in addition to improved fabrication procedures that allow more complete filling of VO_2 in a silicon trench, it should be possible to achieve even larger extinction ratios with lower insertion losses using the VO_2 embedded silicon waveguide platform. This work, in combination with prior work integrating a 2 μm long segment of $Ge_2Sb_2Te_5$ (GST) within a silicon waveguide [76], serves to push forward design approaches which integrate tunable materials within silicon photonic waveguides. In particular, the embedded trench approach is expected to be a promising platform to explore emerging, engineered O-PCMs with optimized properties, such as GSS_4T_1 [77], which by minimizing κ can further reduce insertion loss while maintaining a large extinction ratio.

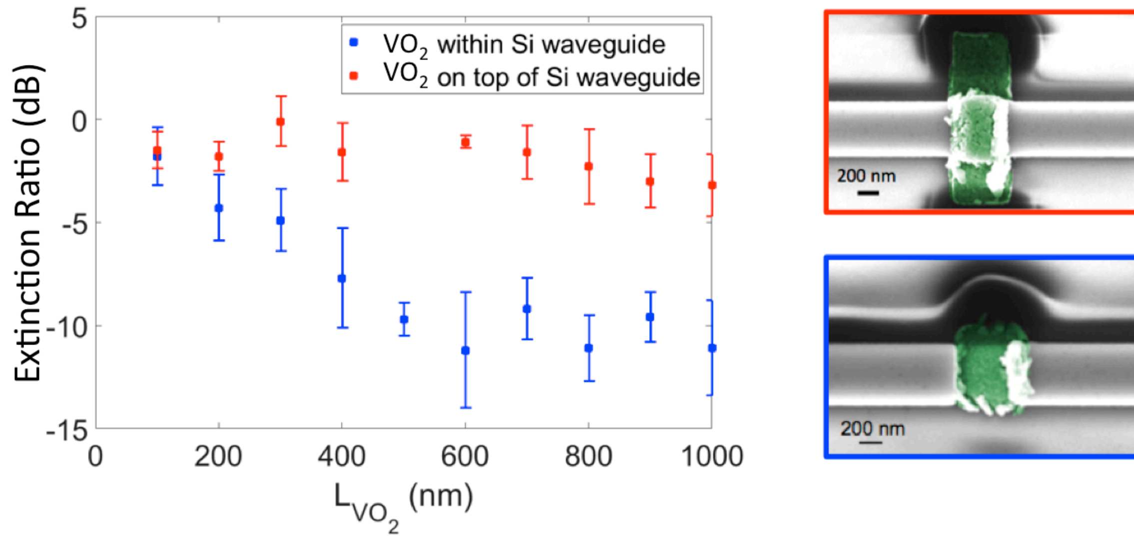

Figure 3.12. Measured extinction ratio for Si/VO_2 waveguides with VO_2 on top of (red data points and upper right SEM image) and embedded within (blue data points and lower right SEM image) the silicon waveguide. Figure adapted and reprinted with permission from [74]. © 2017 OSA.

3.2.8 Proposed implementation as all-optical modulator with in-plane excitation

As mentioned in Section 3.2, with the demonstration that the SMT can be induced with near infrared wavelengths (*e.g.*, 1650 nm) [72], it is expected radiation within the silicon waveguide can induce the SMT of the embedded VO_2 section. Figure 3.13 shows cartoon schematics of this proposed device operation. In Figure 3.13(a), continuous wave (CW) near-infrared radiation (light blue) is transmitted through the VO_2 embedded silicon waveguide. For this case, the VO_2 is in the semiconducting state and is shown in green. In Figure 3.13(b), ultrafast near-infrared pump pulses, shown in purple, are injected into the silicon waveguide. These pulses induce the SMT of VO_2, transiently switching the VO_2 into the metallic phase (shown in red). To mimic the free-space optical experiments which induced the SMT of thin films of VO_2 [44-51, 72], fabrication improvements will likely be necessary to achieve smooth Si/VO_2 interfaces and

successfully fill the trenches with high aspect ratios. Inducing the SMT of the embedded VO_2 section results in modulation of the incident CW radiation and is seen at the output in Figure 3.13(b). For clarity, two different colors are used to represent the incident CW radiation and the pump pulses. However, these can be centered at the same wavelength, which is most suitable for practical implementation [5]. Further analysis of this VO_2 embedded silicon waveguide geometry as an in-plane, ultrafast all-optical modulator, including its projected comparison to other state-of-the-art all-optical modulators, is presented and discussed in Section 4.3. In addition, for electro-optic applications, it is expected modification of the proposed embedded geometry that allows for integration of electrodes can be used to realize high-speed, small-footprint electro-optic modulators. This is discussed in Section 4.2.2.

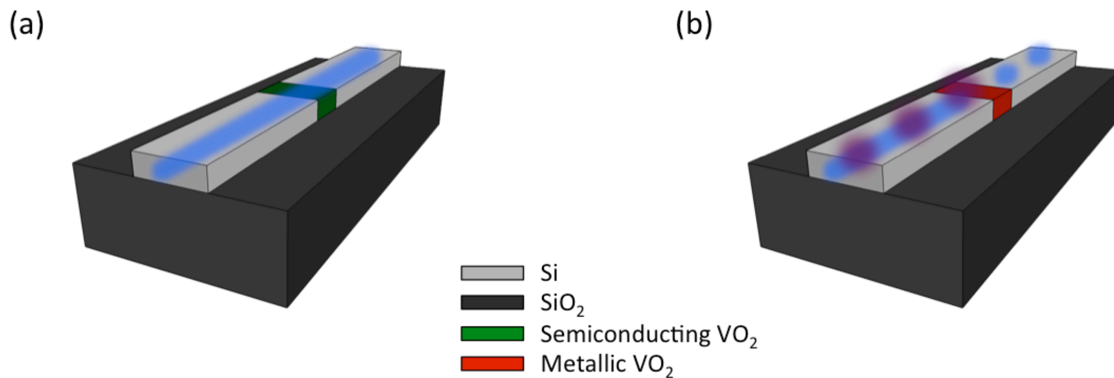

Figure 3.13. Schematic of proposed operation of VO_2 embedded silicon waveguide geometry as an all-optical modulator with in-plane excitation. (a) VO_2 embedded silicon waveguide in its passive state, showing transmission of radiation (light blue) through silicon (gray) and semiconducting VO_2 (green). (b) VO_2 embedded silicon waveguide showing optical modulation. Ultrafast pulses (purple) induce the SMT of VO_2, switching the VO_2 to its metallic state (shown in red), resulting in modulation of the incident radiation at the output of the waveguide.

3.3 Transverse magnetic mode Si/VO_2 ring resonator

In this section, an experimental demonstration of a TM mode Si/VO_2 ring resonator structure that has the potential to support ultrafast optical signal modulation is presented. As described in Section 2.3, in comparison to TE polarization, TM polarized light has increased interaction with VO_2 atop a silicon waveguide. By operating a TM-mode Si/VO_2 ring resonator in the near critical coupling regime, large extinction ratios can be achieved with small patches of VO_2. This is demonstrated in Figure 3.14 using a 10 μm radius Si/VO_2 ring resonator (waveguide dimensions are 500 nm width × 220 nm height) with a 350 nm long × 500 nm wide × ~ 80 nm thick VO_2 patch atop the silicon waveguide. Thermo-optic characterization (see Section 2.2.3.2 for experimental setup) was performed on both Si/VO_2 and control (silicon only) ring resonators. The results are shown in Figure 3.14(b-d). Figure 3.14(b) shows the raw transmission data for the Si/VO_2 ring resonator. The redshift is a result of the thermo-optic effect of silicon while the changes in resonance depth for $T \geq 60°C$ are attributed to the SMT of VO_2. Although the T_{SMT} of VO_2 is typically ~ 68°C, a change in the resonance condition is likely seen at 60°C due to the thermal stage heating above 60°C before stabilizing at 60°C. To clearly see the effect of VO_2, the data are replotted in Figure 3.14(c) with the thermo-optic effect of silicon subtracted out. This figure represents the performance expected to be demonstrated by using ultrafast out-of-plane optical excitation for which no transient heating is expected. In this device geometry, assuming operation at room temperature (*i.e.*, no effect from silicon), ~ 9 dB extinction can be achieved with a VO_2 percent ring coverage of only 0.55%. The observed change in resonance depth occurs due to modification of the ring coupling condition by tuning the losses in the ring when the VO_2 transitions to the metallic phase. The idea of modifying the coupling condition of a ring resonator to achieve high extinction modulation was previously demonstrated in a graphene coated silicon

nitride ring resonator [31]. To understand the impact of polarization, as a comparison, ~ 10 dB was achieved in a 1.5 μm radius TE mode Si/VO_2 ring resonator, also operating in the near critical coupling regime, using a 500 nm patch of VO_2 (VO_2 percent ring coverage of 5%) [56]. Figure 3.14(d) shows data for the control (silicon only) TM mode ring resonator as clarification that the effects seen in Figure 3.14(b,c) are primarily from VO_2. The data shown in Figure 3.14(d) also have the thermo-optic effect of silicon subtracted out.

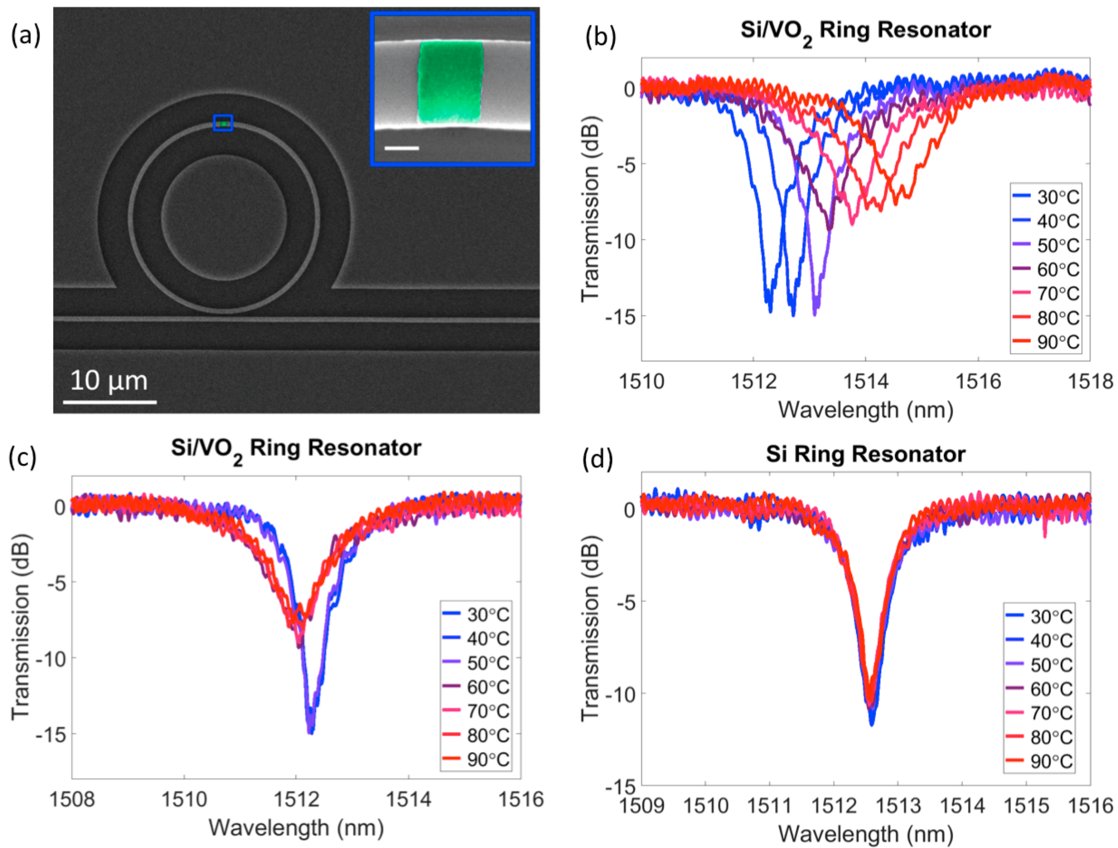

Figure 3.14. (a) SEM image of 10 μm radius TM mode Si/VO_2 ring resonator. The VO_2 patch (false colored green) is 350 nm long and is shown in the inset. The white scale bar in the inset is 200 nm. (b) Raw data from thermo-optic measurement of resonance in Si/VO_2 ring resonator. (c,d) Thermo-optic measurement of resonance in (c) Si/VO_2 and (d) Si ring resonator with the thermo-optic effect of silicon subtracted out to clearly demonstrate the effect of the SMT of VO_2.

3.3.1 Proposed implementation as all-optical modulator with out-of-plane excitation

Figure 3.15 presents cartoon schematics for implementation of the TM mode Si/VO_2 ring resonator as an all-optical modulator with out-of-plane excitation. This proposed experimental geometry is very similar to that used in Ref. [64] which showed optical modulation of a Si/VO_2 ring resonator with 25 nanosecond optical pulses. Figure 3.15(a) shows the ring resonator for the case where the VO_2 patch is semiconducting (shown in green). For the example shown, CW input light (shown in blue) resonant with the ring is selected. Therefore, in the passive state (*i.e.,* semiconducting VO_2 atop the ring resonator), there is no optical transmission through the device. To induce transmission through the device, ultrafast optical pulses with pulse lengths on the order of 100 femtoseconds, shown in orange in Figure 3.15(b), are incident on the VO_2 patch. By inducing the SMT of VO_2, the resonance condition in the resonator is broken, and light is transmitted through the device. In this way, the optical pulse sequence from the orange pulses can be imprinted on the blue light within the bus waveguide. By selecting pulses in fluence regimes that allow for the ultrafast dynamics in VO_2 [44-51], it is expected individual pulses on the order of a picosecond can be generated within the bus waveguide. Since this geometry utilizes out-of-plane excitation, photon energies above the band gap of silicon may be used. However, especially if a large beam spot is used, care must be taken to ensure effects resulting from the SMT of VO_2 will dominate in comparison to induced linear or nonlinear optical responses in silicon.

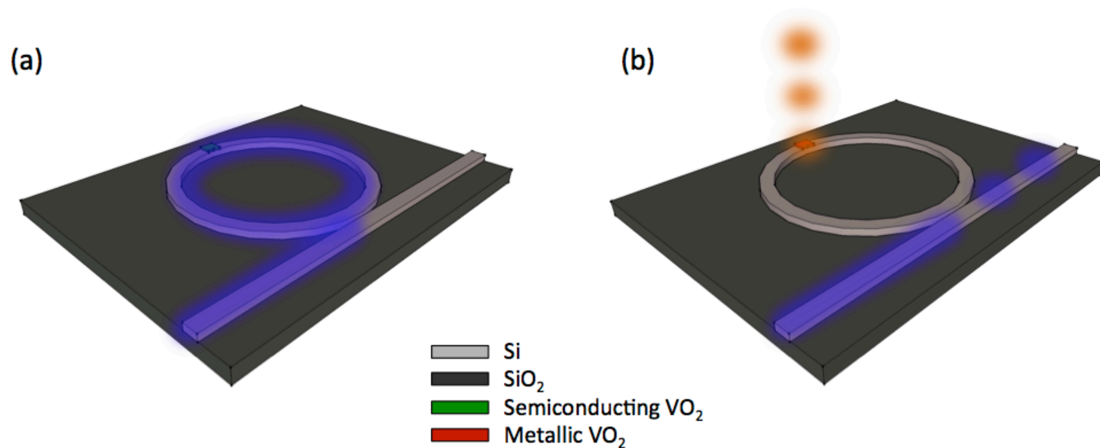

Figure 3.15. Schematic of proposed operation of TM mode Si/VO_2 ring resonator an all-optical modulator with out-of-plane excitation. (a) For semiconducting VO_2 (shown in green), the input wavelength is resonant and there is no optical transmission. (b) Ultrafast optical pulses (shown in orange) induce the SMT of VO_2, switching the VO_2 to its metallic state (shown in red). This results in modification of the resonant condition, resulting in optical transmission through the device that mimics the sequence of the incident optical pulses.

3.4 Conclusions

In summary, in this chapter, a compact, non-resonant, broadband hybrid Si/VO_2 integrated photonic device was first demonstrated by embedding VO_2 within a silicon waveguide for improved modal overlap with VO_2. With thermal activation of the SMT, devices with VO_2 lengths varying from 100 nm to 1000 nm were characterized, showing ~ 10 dB extinction at 1550 nm in experiment for a VO_2 length of only 500 nm. With fabrication improvements, calculations suggest an extinction ratio of nearly 14 dB with approximately 2 dB insertion loss can be achieved. This steady-state characterization provides insight into expected device performance for high-speed applications, and proposed implementation as an all-optical modulator with in-plane excitation was presented. Chapter 4 serves to extend that discussion, presenting its projected performance with other state-of-the-art all-optical modulators. In

addition, within in this chapter, experimental results for a TM mode Si/VO_2 ring resonator device were presented, demonstrating improved extinction ratio per VO_2 fractional coverage of the silicon ring (in comparison to a Si/VO_2 TE ring resonator) as a result of using TM polarization. Its proposed implementation as an all-optical modulator with out-of-plane excitation was also briefly presented.

Chapter 4

4. Perspectives on Si/VO_2 optical modulators

4.1 Introduction

In Chapter 2 and Chapter 3, work with the potential to push forward the realization of practical, high-speed Si/VO_2 electro-optic and all-optical modulators was presented. This chapter serves to summarize the perspectives on Si/VO_2 electro-optic and all-optical modulators while also providing additional considerations for further performance improvement. First, building on the experimental demonstration of embedding VO_2 within a silicon waveguide reported in Chapter 3, an embedded Si/VO_2 electro-optic device geometry with the potential to improve electro-optic Si/VO_2 modulator performance is proposed. Second, pushing toward more practical implementation of Si/VO_2 all-optical modulators, a more detailed analysis of the device geometry presented in Chapter 3 which allows for in-plane, ultrafast excitation is presented. Its expected optimal performance is compared to state-of-the-art all-optical modulators. In addition, design considerations to allow for more effective operation for both TE and TM input polarizations are examined, in particular by consideration of waveguide geometry and transient mode propagation.

4.2 Si/VO_2 electro-optic modulators

While the work in Chapter 2 pushed forward the understanding of electrically inducing the SMT of VO_2 in silicon photonic devices, there remains potential for improvement. In particular, to date, no Si/VO_2 electro-optic device has demonstrated sufficient (> 4 dB) extinction ratio performance using the fastest known time dynamics of the electrically induced SMT (< 2 ns) [52, 53] and MST (< 3 ns) [52]. The two Si/VO_2 electro-optic devices demonstrating the fastest

temporal responses have been silicon waveguide [52] [Figure 1.12(a)] and ring resonator [67] structures (Chapter 2) that integrate a patch of VO_2 on top of the respective silicon photonic structure. These geometries utilize a small gap (~ 100 nm) between the electrical contacts to reduce the required applied voltage; however, achieving sufficient extinction ratios (> 4 dB) required triggering the SMT of volumes of VO_2 outside the electrical contacts. Because the SMT of the portion of the VO_2 film residing outside the electrical contacts is likely activated by Joule heating, which results from the heating of metal filaments of VO_2 formed between the electrical contacts by a voltage-driven effect, suggested in Ref. [52] and discussed in Section 1.4.2, the time dynamics for switching the VO_2 domains outside the contacts is slower than switching the VO_2 domains between the contacts. The work in Ref. [59], briefly presented and discussed in Figure 1.12(b) and Section 1.4.2, suggests it is only using VO_2 between the electrical contacts to achieve the demonstrated modulation. However, > 1 μs response times are demonstrated, and it is possible this is a result of the relatively long (≥ 100 ns) voltage pulses used which are expected to cause significant Joule heating, forcing longer MST times. Here, a Si/VO_2 electro-optic modulator device design is proposed whereby the VO_2 patch is embedded within the silicon waveguide. In this geometry, nearly all of the active VO_2 volume is between the electrical contacts, suggesting the fastest SMT and MST dynamics can be fully utilized.

4.2.2 Si/VO_2 electro-optic modulator embedded design

In the proposed design, the first step of lithography will be to simultaneously define a rib waveguide and a void for backfilling with VO_2. This is done by etching 130 nm into a 230 nm SOI wafer, leaving 100 nm silicon slab thickness adjacent to the waveguide and a void of dimensions 300 nm (width) × 500 nm (length) × 130 nm (thickness) within the rib waveguide for

subsequent filling with VO_2. Due to the higher thermal conductivity of silicon in comparison to silicon dioxide, the silicon slab in the rib waveguide geometry is expected to provide more rapid heat dissipation to enable faster MST times. In the second step of lithography, the void will be backfilled with VO_2. The aspect ratio of this void is not expected to limit its filling with typical physical vapor deposition methods (*e.g.*, sputtering, pulsed laser deposition). The third and final step of lithography will serve to pattern electrical contacts on top of the backfilled VO_2 section. To allow for low voltage operation, the metallic contacts are patterned with 250 nm spacing, overlapping each side of the VO_2 patch by 25 nm. In the fully fabricated device, the metallic contacts are 70 nm thick on top of the silicon waveguide and slab and 50 nm thick on the waveguide side walls. Figure 4.1 shows schematics for the proposed fabrication steps for the fully fabricated device.

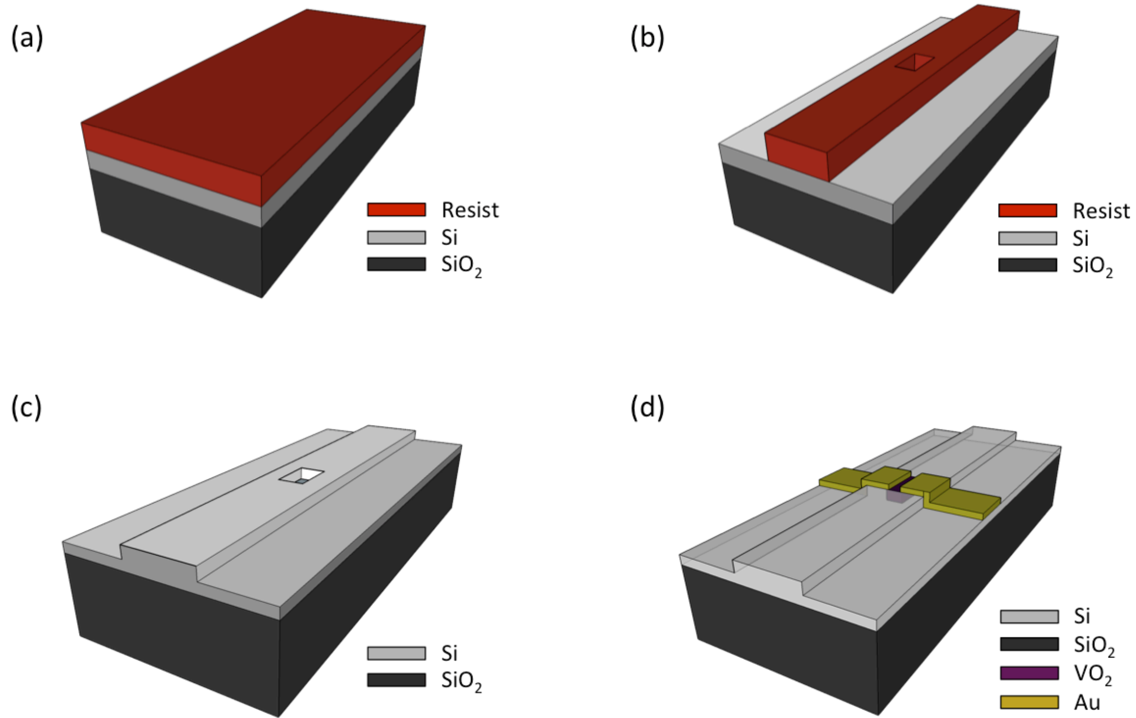

Figure 4.1. Multiple lithography steps for proposed Si/VO_2 embedded electro-optic design. Resist, Si, SiO_2, VO_2, and Au are shown in red, light gray, dark gray, purple, and gold. (a-c) First step of lithography, showing (a) resist spun on the silicon substrate, (b) patterning and development of the resist, and (c) etching of rib waveguide and void in the center of the waveguide. (d) Final device structure after two additional lithography steps (resist patterning and deposition of VO_2; resist patterning and deposition of Au).

Since the proposed design patterns the metallic contacts on the top surface and side walls of the waveguide, non-negligible absorption and reflection from the contacts is expected, especially when the waveguide width is narrow and the optical mode significantly extends outside of the silicon guiding layer. Increasing the waveguide width is expected to reduce the interaction with the metallic contacts as a result of the increased optical confinement. However, for the fixed volume of VO_2 in the proposed design, extending the waveguide width is also expected to give reduced extinction ratios due to the reduced optical interaction with VO_2. To verify this hypothesis, the silicon waveguide width was swept from 500 nm to 1500 nm in 100 nm intervals

and the waveguide transmission was monitored for the fundamental TE mode in a three-dimensional FDTD simulation (Lumerical FDTD Solutions). Optical properties for VO_2 were taken and imported from [43] while optical properties of silicon, silicon dioxide, and gold were taken from Lumerical Solutions' material database [73, 78]. Figure 4.2(a) shows a perspective view of the Si/VO_2 embedded electro-optic design, explicitly showing the silicon waveguide width, which was swept during the simulation. Figure 4.2(b) presents the extinction ratio as a function of the silicon waveguide width for incident wavelengths spanning 1500 nm – 1630 nm and reveals a silicon waveguide width of ~ 700 nm is optimal, giving extinction ratios greater than 6 dB from 1530 nm – 1630 nm. In addition, Figure 4.2(c) shows both the insertion loss and extinction ratio as a function of the silicon waveguide width for a wavelength of 1550 nm. The results in Figure 4.2(b,c) assume the entire VO_2 segment is undergoing the SMT. For high-speed operation (with reduced Joule heating), if the expected extinction ratio is not observed, it could be due to a bottom portion of the VO_2 not undergoing the SMT as it will have an electric field environment different to the top portion of the VO_2. As expected, shown in Figure 4.2(c), the device exhibits an inverse relationship between insertion loss and waveguide width. For example, for a waveguide width of 500 nm, there is significant interaction with the metal contacts, giving an insertion loss of approximately 9 dB. This large insertion loss also results in low (~ 1.5 dB) extinction ratio. As the waveguide width increases, a maximum extinction ratio of 6.1 dB is shown for a waveguide width of 700 nm. Further increasing the waveguide width beyond 700 nm gives reduced extinction ratio (and reduced insertion loss) as less of the mode interacts with both the metallic contacts and the VO_2. Operation at a waveguide width of 700 nm is recommended, where at 1550 nm, the insertion loss and extinction ratio are 4.4 and 6.1 dB, respectively. It is expected this design geometry could operate with the fastest electrically

induced SMT and MST dynamics. The performance metrics presented here are inferior to those for the VO_2 embedded silicon waveguide (Chapter 3) as a result of the integration of the metal contacts.

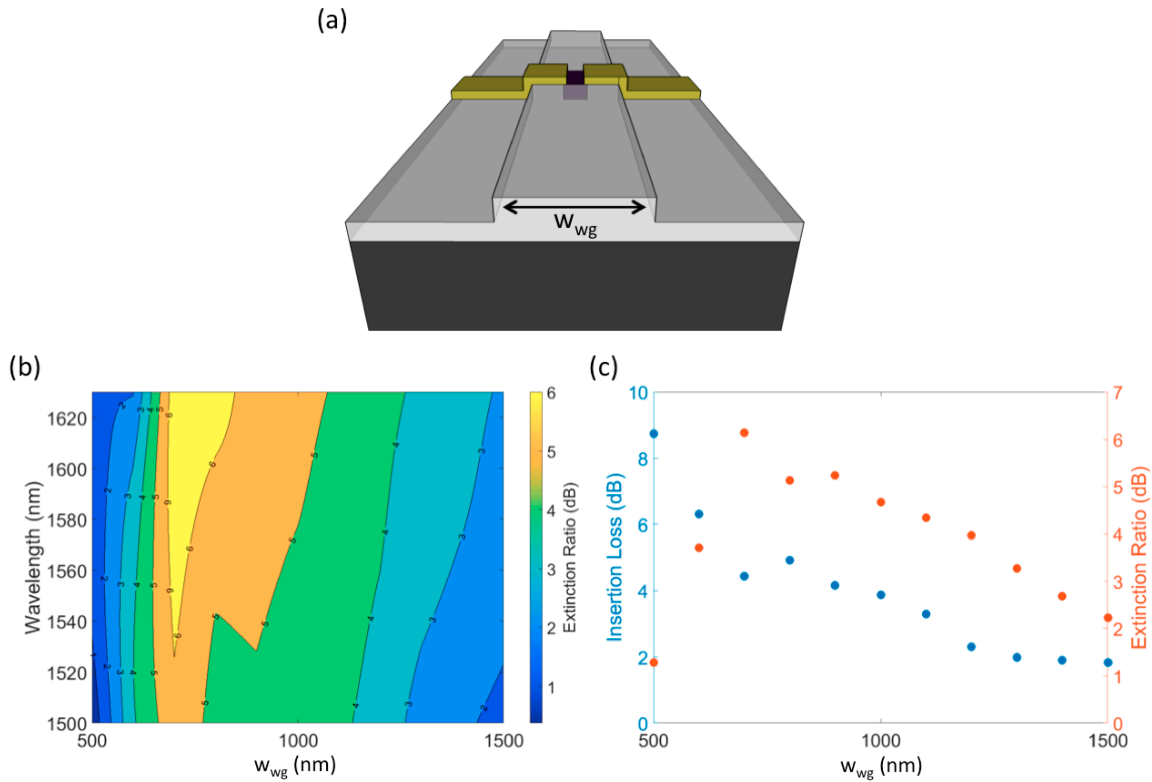

Figure 4.2. (a) Perspective view of Si/VO_2 embedded electro-optic modulator design, showing the silicon waveguide width (labeled w_{wg}) which is swept during the simulations. Si, SiO_2, VO_2, and Au are shown in light gray, dark gray, purple, and gold. (b) Extinction ratio as a function of silicon waveguide width from 1500 nm - 1630 nm. (c) Insertion loss and extinction ratio at 1550 nm as a function of w_{wg}.

While the design proposed above demonstrates promise by means of combining the Si/VO_2 designs in Ref. [52] and Chapter 3, other proposed Si/VO_2 electro-optic modulator designs [60-63], discussed in Section 1.4.2, which utilize VO_2 only between the electrical contacts may also provide avenues to push the limits of high-speed, high extinction ratio Si/VO_2 electro-optic

modulators. However, feasibility of the proposed modulator in Ref. [62] will require fabrication improvements for depositing VO_2 in high aspect ratio nanoscale gaps. In addition, for these proposed geometries [60-62] whereby at least one of the electrical contacts is silicon, it must be confirmed that high-speed electrical performance is not compromised when using doped silicon for electrical actuation of the SMT since the electrical conductivity of highly p-doped silicon (10^{20} cm^{-3} dopant concentration) is three orders of magnitude less than that of gold at room temperature [79, 80], and it is expected there will be increased insertion loss in these proposed geometries if extremely high doping is required to actuate the SMT.

4.3 Si/VO_2 all-optical modulators with in-plane excitation

Considering all-optical modulator geometries, out-of-plane excitation is the most readily translatable method to demonstrate ultrafast tunability of Si/VO_2 photonic devices. For example, as mentioned in Section 1.4.3, Ref. [64] demonstrated active tunability of Si/VO_2 ring resonators and waveguides by actuating the SMT transition with a 25 nanosecond optical pulse. It is expected these Si/VO_2 device geometries, in addition to the geometry presented in Section 3.3, can also be used as platforms to realize modulation on fast time scales (~ femtosecond “on”, ~ picosecond “off”) with the large quantity of ultrafast studies on VO_2 thin films [44-51]. However, for more practical implementation, an interchip or intrachip all-optical modulator will likely require in-plane excitation. With experimental evidence the SMT can be induced with near infrared wavelengths [72], it is expected the VO_2 embedded silicon waveguide geometry can be implemented as an all-optical modulator with in-plane excitation (*i.e.,* within the silicon waveguide), as introduced in Section 3.2.8. In this section, expected modulator performance is

compared with state-of-the-art modulators and methods for more effective polarization independent operation are explored.

4.3.1 Calculation of energy consumption

Using the design described in Chapter 3 for L_{VO_2} = 200 nm and assuming perfect fabrication (*i.e.*, h_{VO_2} = 220 nm), the threshold incident energy ($E_{inc,th}$) needed to induce optical changes in the VO_2 is given by:

$$E_{inc,th} = \frac{F_{abs,th} \times (w \times h)}{A} \tag{6}$$

where $F_{abs,th}$ is the measured threshold absorbed fluence (0.25 mJ/cm^2), taken from [72], w and h are the cross-sectional width and height of the Si/VO_2 waveguide (700 nm and 220 nm, respectively), and A is the absorbed fraction of the simulated input light when VO_2 is in the semiconducting state [shown in Figure 3.11(a)]. Calculation gives an expected $E_{inc,th}$ of ~ 880 fJ at a wavelength of 1550 nm.

4.3.2 Comparison to state-of-the-art all-optical modulators

As discussed in Section 1.2.1, the ideal modulator simultaneously maximizes modulation speed, extinction ratio, and optical bandwidth while minimizing insertion loss, device footprint, and energy consumption. Table 1 compares these performance metrics for five state-of-the-art all-optical modulators along with the embedded Si/VO_2 all-optical modulator design described in Chapter 3 for L_{VO_2} = 200 nm and h_{VO_2} = 220 nm, assuming the embedded Si/VO_2 all-optical modulator can be modulated at a speed commensurate with the optically-activated switching speed of VO_2 thin films. This table only considers modulators with in-plane pump pulses; no all-optical modulators with out-of-plane pumping are considered. Modulation speed is presented in

both units of picoseconds (total “on” and “off” time) and Gb/s to include metrics for modulators that were tested for individual pulses (picoseconds) and for data streams (Gb/s). For a general comparison, a full “on-off” cycle corresponds to 2 bits. With this assumption, as an example, a total “on-off” time of 50 picoseconds corresponds to a 40 Gb/s data stream.

All-Optical Modulators	**Footprint (μm^2)**	**Insertion Loss (dB)**	**Incident Switching Energy (fJ)**	**Speed (ps : Gb/s)**	**Optical bandwidth (nm)**	**Extinction Ratio (dB)**
Si PhC nanocavity [23]	< 10	NA	~ 100 - 450	~ 67 : NA	< 0.5	≤ 10
Si-organic hybrid slot waveguide [35]	~ 4000	NA	~ 9,500	NA : 170.8	> 80	7.7
InGaAsP PhC nanocavity [36]	0.125	NA	0.42 – 2.88	~ 55 : NA	< 1	3 - 10
GaAs PhC nanocavity [81]	< 10	NA	~120	~ 15 : NA	< 2	10
Si-nc/SiO_2 filled Si slot ring resonator [82]	1600	NA	~10,000	20 : NA	< 1	3.6
This work (simulated)	0.14	2.2	~ 880	~ 10 : NA	> 200	13.8 (upper limit)

Table 1. All-optical modulator performance metrics (device footprint, insertion loss, incident switching energy, operation speed, optical bandwidth, and extinction ratio) experimentally measured for modulators in Refs. [23, 35, 36, 81, 82] and theoretically expected for our proposed Si/VO_2 all-optical modulator. Table reprinted with permission from [75]. © 2017 SPIE.

Inspection of Table 1 reveals the promise of the Si/VO_2 in-plane all-optical modulator, projecting a device footprint, operation speed, optical bandwidth, and extinction ratio equivalent or superior to the other modulators in each of these categories. For extinction ratio, it is unclear whether the full change in optical properties will be observed when accessing the short-lived (~1-10 ps) transient state of VO_2. For example, in Ref. [49], it appears there is reduced optical contrast at lower incident fluences, but in Ref. [51], it appears lower fluences demonstrate the same magnitude of optical response as high fluences. This can be seen in Figure 1.9(a-b).

Therefore, in Table 1, 13.8 dB is suggested as the upper limit for the expected extinction ratio. While resonator-based, high Q/V structures (*e.g.*, PhC nanocavities in Refs. [23, 36, 81]) show lower incident switching energy, these structures have reduced bandwidths. Moreover, the modulators fabricated in Ref. [81] and Ref. [36] were patterned in GaAs and InGaAsP, respectively, and are therefore not easily compatible with silicon photonics fabrication. For applications where low switching energy is of paramount importance and optical bandwidth can be compromised, integrating VO_2 in a high Q/V photonic structure (*e.g.*, [83]) could reduce the required incident energy to a few fJ.

4.3.3 Design considerations for polarization independent operation

While the work presented in Chapter 3 and the above analysis have considered only TE operation, here design considerations to achieve large extinction ratios for both TE and TM polarization are examined. In Chapter 3 and above, a waveguide width of 700 nm was chosen because it increases the effective index (forcing more interaction with the VO_2) while not clearly supporting the second order TE mode. The second order TE mode is clearly supported for a waveguide width of 800 nm. However, for this waveguide geometry (220nm × 700nm), the fundamental TM mode is poorly guided (n_{eff} = 1.678 at λ = 1550nm) and is largely confined to the silicon dioxide substrate. This is demonstrated in Figure 4.3(a) which shows the electric field intensity mode profile for a silicon waveguide of both fundamental TE and TM modes (Lumerical MODE Solutions). In Figure 4.3(b), insertion loss and extinction ratio at λ = 1550 nm are presented for both the fundamental TE and TM modes for L_{VO_2} spanning 0 to 400 nm in 50 nm intervals. While both polarizations demonstrate comparable extinction ratios for L_{VO_2} = 50

nm, for longer VO_2 patches, there is quickly a saturation in extinction ratio for TM polarization. Below, design methods to improve operation for TM polarization are explored.

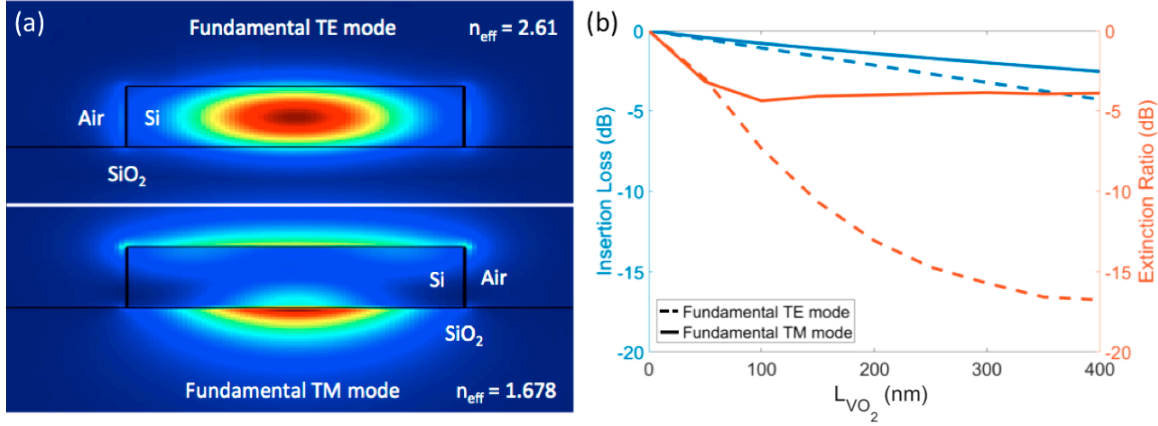

Figure 4.3. (a) Electric field intensity mode profiles of the fundamental TE (top) and fundamental TM (bottom) optical modes in a silicon waveguide of dimensions 700 nm (width) × 220 nm (height), generated using Lumerical MODE Solutions. Reduced confinement in the silicon is observed for the fundamental TM mode and is demonstrated in the reduced effective refractive index, n_{eff}. (b) Insertion loss and extinction ratio for both the fundamental TE and TM optical inputs for varying L_{VO_2} [device geometry is shown in Figure 3.2(a)], showing a saturation in extinction ratio for the fundamental TM mode for $L_{VO_2} \geq 100$ nm.

4.3.3.1 Considerations of mode propagation through VO_2

In this section, to further understand the extinction ratio saturation for TM polarization, transmission through the VO_2 embedded silicon waveguides for TE and TM polarizations are analyzed and compared, considering both semiconducting and metallic VO_2. To understand propagation losses for the case of semiconducting VO_2, optical modes of a waveguide composed entirely of semiconducting VO_2 are examined using Lumerical MODE Solutions. In addition, for TE and TM polarizations and both semiconducting and metallic VO_2, transient propagation of the mode through the VO_2 section of a Si/VO_2 waveguide is investigated by actively monitoring the mode in a three-dimensional FDTD simulation (Lumerical FDTD Solutions).

Figure 4.4(a) presents transmission through the Si/VO_2 waveguide as a function of L_{VO_2}, for TE and TM polarizations, considering both semiconducting and metallic VO_2. To understand transmission for semiconducting VO_2, the transmission [*T(z)*] data were fitted to a single exponential corresponding to Beer's law, of the form:

$$T(z) = T_0 e^{-\alpha z} \tag{7}$$

where z, α, and T_o are the propagation distance into the semiconducting VO_2 section, the absorption coefficient, and optical the transmission for a VO_2 patch length of 0 nm, respectively. For TE polarization, α = 2.47 μm^{-1} (R^2 = 1), while for TM polarization, α = 1.47 μm^{-1} (R^2 = 0.995). Converting to extinction coefficient (κ):

$$\kappa = \frac{\alpha\lambda}{4\pi} \tag{8}$$

gives κ of 0.31 and 0.18 for TE and TM polarizations, respectively. These values can be understood by inspection of the electric field intensity mode profiles for both polarizations, shown in Figure 4.4(b). Similar to Figure 4.3(a), Figure 4.4(b) presents the electric field intensity mode profiles (Lumerical MODE Solutions) for a waveguide composed entirely of semiconducting VO_2 (instead of for silicon as was shown in [Figure 4.3(a)]) and includes the complex effective refractive index ($\tilde{n}_{eff}$) for both TE and TM polarizations. The complex effective refractive index is given by:

$$\tilde{n}_{eff} = n_{eff} + i\kappa_{eff} \tag{9}$$

where n_{eff} and κ_{eff} are the real and imaginary components of the effective refractive index, respectively. Since the real components of the refractive indices of silicon and semiconducting

VO_2 are very similar at 1550 nm ($n_{semi\text{-}VO_2}$ = 3.3 [43] ; n_{Si} = 3.476 [73]), the mode profiles in Figure 4.4(b) appear very similar to those in Figure 4.3(a). This is represented in the real component of the n_{eff} of the modes. Considering TE polarization, n_{eff} is 2.61 and 2.418 for silicon and semiconducting VO_2 waveguides, respectively, while for TM polarization, n_{eff} is 1.678 and 1.547 for silicon and semiconducting VO_2 waveguides, respectively. However, in contrast to silicon, κ of semiconducting VO_2 is non-zero at 1550 nm. Therefore, the mode profiles for both polarizations have non-zero κ_{eff} values. The electric field intensity mode profiles give κ_{eff} values of 0.332 and 0.158 for TE and TM modes, respectively, which is in good agreement with the results from the fit of the transmission data in Figure 4.4(a) (κ of 0.31 and 0.18), demonstrating the optical mode is largely unchanged as it propagates through the semiconducting VO_2.

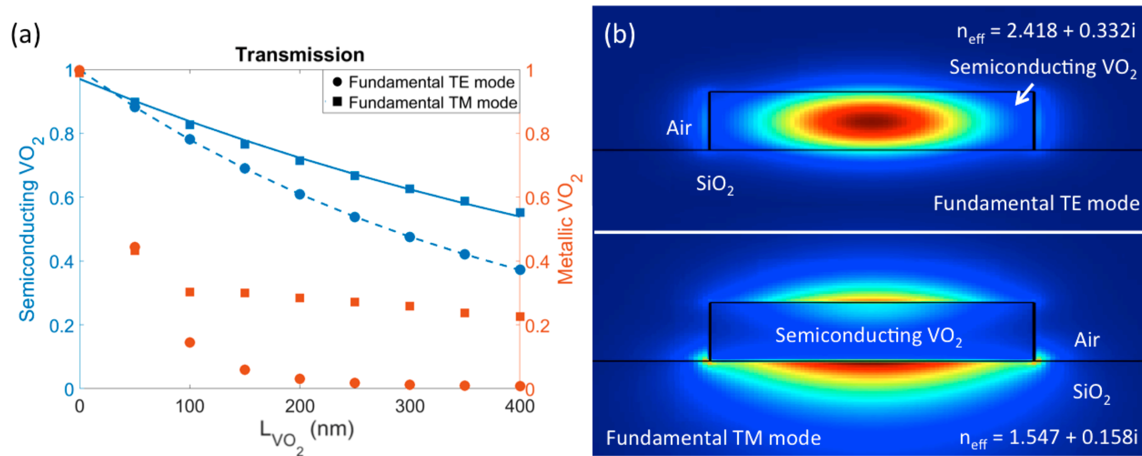

Figure 4.4. (a) Transmission through Si/VO_2 waveguide for both fundamental TE and TM optical inputs for varying L_{VO_2}, considering both semiconducting VO_2 (blue) and metallic VO_2 (orange). The waveguide dimensions are 700 nm (width) × 220 nm (height). The fundamental TE mode is represented by circles while the fundamental TM mode is represented by squares. Single exponential fits (dashed line for fundamental TE mode; solid line for fundamental TM mode) are shown for both semiconducting VO_2 curves. (b) Electric field intensity mode profiles of the fundamental TE (top) and fundamental TM (bottom) optical modes in a 700 nm (width) × 220 nm (height) waveguide composed entirely of semiconducting VO_2, generated using Lumerical MODE Solutions.

While semiconducting VO_2 supports a propagating (although with non-zero loss) optical mode, metallic VO_2 does not. Since metallic VO_2 does not support a propagating mode, transmission through a metallic VO_2 section of waveguide cannot be modeled with Beer's law. For this reason, transmission for metallic VO_2 is not fit with a single exponential in Figure 4.4(a), for either polarization. To better understand the transmission through the VO_2 embedded silicon waveguide for the case of metallic VO_2, cross sectional electric field intensity profiles at 50, 150, 250, and 350 nm into a 400 nm long metallic VO_2 segment are taken within a three-dimensional FDTD simulation (Lumerical FDTD Solutions). These profiles are shown in Figure 4.5 for both the fundamental TE [Figure 4.5(b)] and TM [Figure 4.5(c)] modes.

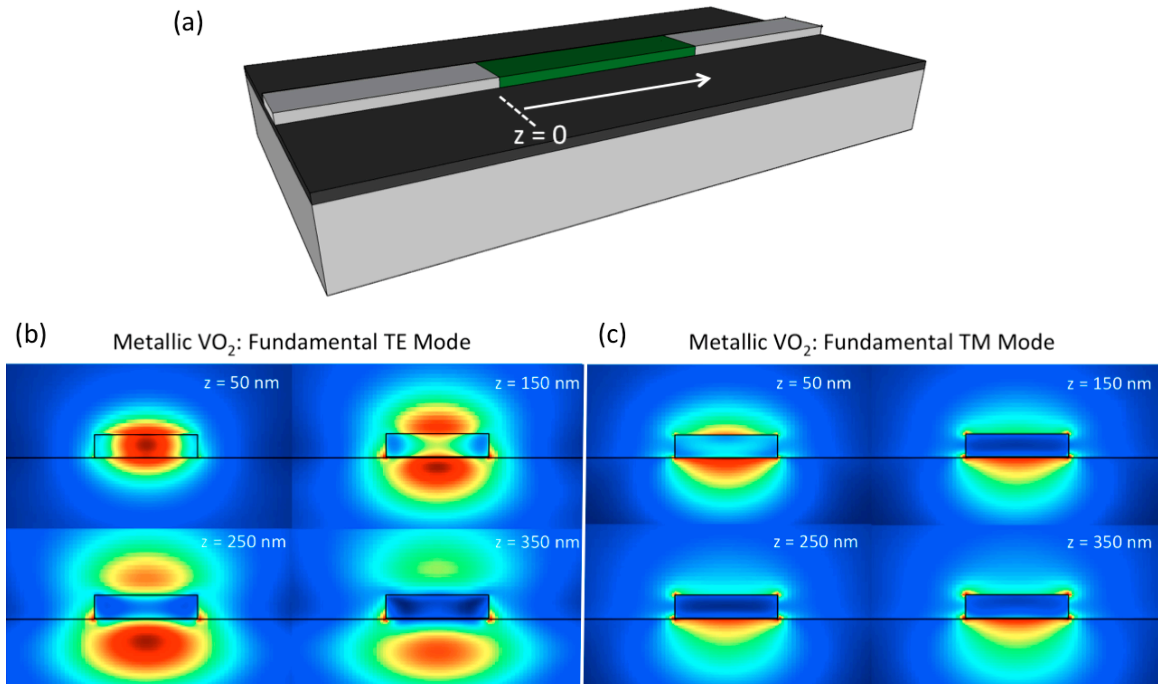

Figure 4.5. (a) Schematic of Si/VO_2 waveguide. VO_2, Si, and SiO_2 are green, light gray, and dark gray, respectively. (b,c) Cross sectional electric field intensity profiles of propagating optical mode (Lumerical FDTD Solutions) at different propagation distances in the VO_2 block, for both the fundamental TE (b) and TM (c) modes.

Figure 4.5 demonstrates the different behavior for the fundamental TE and TM modes as a function of propagation distance (z) in the VO_2 region of the waveguide. For both incident polarizations, the field is pushed out of the metallic VO_2 into the surrounding air and the silicon dioxide substrate. Specifically, after approximately 350 nm, the field has been almost entirely pushed out of the metallic VO_2 for both polarizations, as seen in the bottom right profiles of Figure 4.5(b) and Figure 4.5(c). However, for the fundamental TM mode, due to the orientation of the polarization, more of the optical mode incident at the silicon/metallic VO_2 interface is already within the silicon dioxide cladding, whereby it continues to propagate. For this reason, considering the fundamental TM mode, there is minimal interaction with metallic VO_2 for $z \geq$ 100 nm, resulting in the relatively constant transmission (~ 22-30%) shown for L_{VO_2} = 100 to L_{VO_2} = 400 nm in Figure 4.4(a).

4.3.3.2 Design considerations to improve interaction with metallic VO_2

In this section, two methods of enhancing the modal interaction with metallic VO_2 are considered: (i) adjusting the waveguide geometry and (ii) considering the use of multiple small, isolated segments in place of one single block of VO_2 to allow for mode regeneration. It is well known that increasing the silicon waveguide dimensions will increase the effective index of all propagating modes. Here, to improve the modal interaction with VO_2 for TM input while remaining within fabrication norms (silicon thickness from ~ 220 – 270 nm), the waveguide height is increased to 270 nm to increase the effective index of the TM mode. Due to the emergence of higher order modes for a waveguide geometry of 270 nm × 700 nm, to ensure single mode operation regime for both TE and TM polarizations, a waveguide geometry of 270 nm (height) × 500 nm (width) is used here. Figure 4.6(a) shows the optical mode profiles

(Lumerical MODE Solutions) of a silicon waveguide of this geometry for both the fundamental TE and TM modes. The effective index of the fundamental TM mode is increased to 2.013 [from 1.678 for the 220 nm × 700 nm geometry in Figure 4.3(a)]. This is exhibited in the improved extinction ratio for the fundamental TM mode [Figure 4.6(b)] compared to the prior geometry. For example, for L_{VO_2} = 100 nm, this geometry exhibits 6.4 dB extinction while the prior geometry showed 4.4 dB extinction. However, there is still a saturation of the extinction ratio for $L_{VO_2} \geq$ 100 nm. Optical performance of the TE mode remains largely unchanged, as expected from the relatively small difference in the effective index for the two waveguide geometries [2.61 for the 220 nm × 700 nm in Figure 4.3(a) and 2.55 for the 270 nm × 500 nm geometry in Figure 4.6(a)].

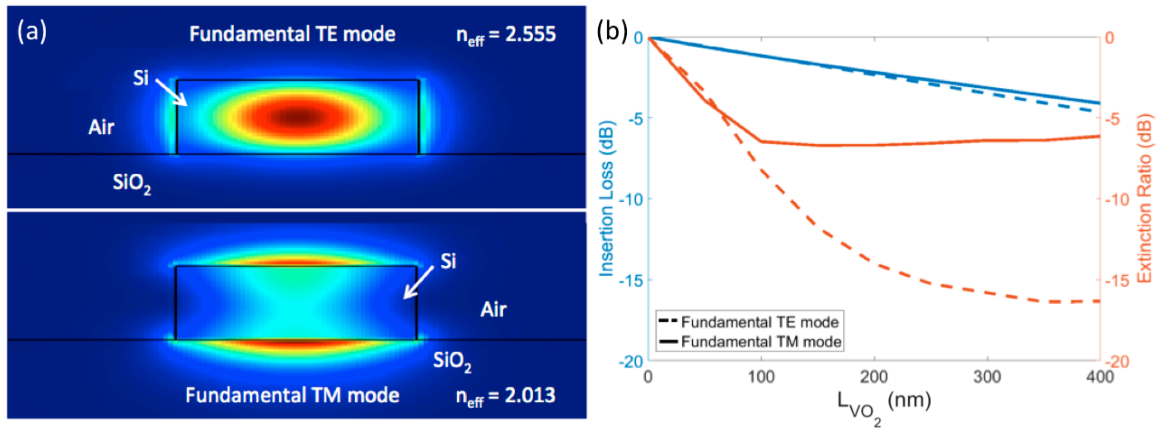

Figure 4.6. (a) Electric field intensity mode profiles of the fundamental TE (top) and fundamental TM (bottom) optical modes in a silicon waveguide of dimensions 500 nm (width) × 270 nm (height), generated using Lumerical MODE Solutions. (b) Insertion loss and extinction ratio for both the fundamental TE and TM optical inputs for varying L_{VO_2}. Increasing the n_{eff} of the fundamental TM mode by modifiying the waveguide geometry gives increased extinction ratio, but a saturation for $L_{VO_2} \geq$ 100 nm is still observed.

To further increase the interaction with metallic VO_2, mode regeneration (*i.e.*, after interaction with metallic VO_2, transient recovery of the propagating mode to its original electric field intensity distribution) is explored. To understand the transient propagation of the optical mode before and after its interaction with a 100 nm long segment of metallic VO_2, the electric field intensity mode profile in a three-dimensional FDTD simulation (Lumerical FDTD Solutions) was monitored. Figure 4.7 shows these profiles before and 50, 100, 500, 1000, and 2000 nm after interaction with the metallic VO_2. From this analysis, Figure 4.7(f) shows the mode returns to its original electric field distribution approximately 2 μm after its interaction with metallic VO_2.

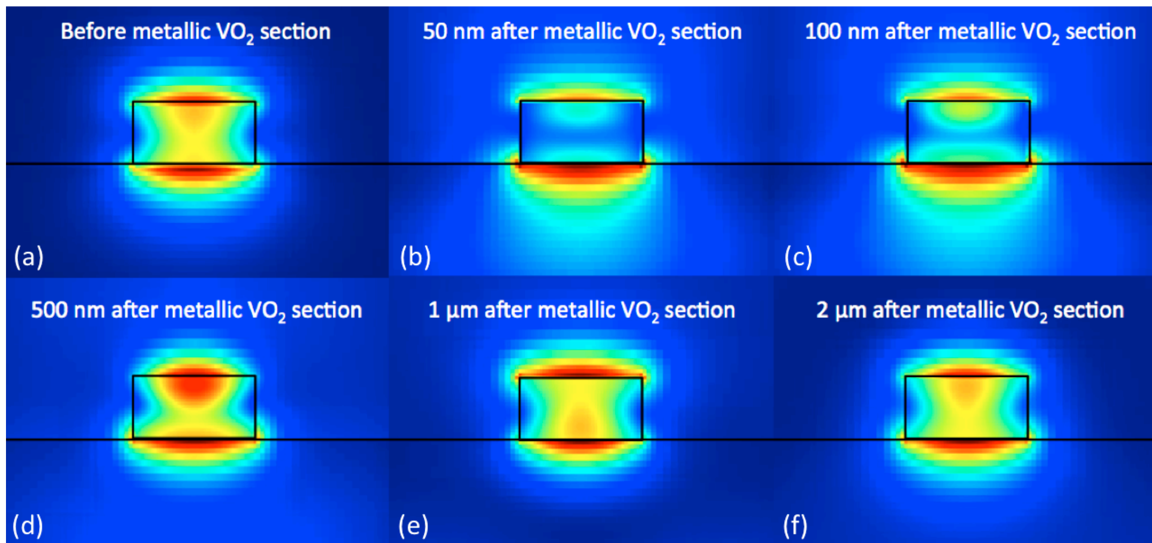

Figure 4.7. Cross sectional electric field intensity profiles of the fundamental TM optical mode (Lumerical FDTD Solutions) before (a) and 50 nm (b), 100 nm (c), 500 nm (d), 1 μm (e), and 2 μm (f) after interaction with a 100 nm long patch of metallic VO_2. After 2 μm, the fundamental TM mode has returned to its original electric field distribution.

By arranging individual 100 nm VO_2 segments spaced by 2 μm, the optical mode can recover before interacting with the next segment of VO_2, therefore increasing interaction with metallic

VO_2 in comparison to a single VO_2 block. A similar design was used in Ref. [84] to get a more uniform field distribution for fixed pulse energy optical switching of GST islands on top of a Si_3N_4 waveguide. Figure 4.8(a) and Figure 4.8(b) show cartoon schematics of two proposed Si/VO_2 device geometries. Here, both have waveguide dimensions of 500 nm (width) × 270 nm (height). Figure 4.8(a) presents a single VO_2 block Si/VO_2 waveguide design, as presented up to this point. Figure 4.8(b) shows the proposed device geometry whereby there are individual 100 nm VO_2 blocks spaced by 2 μm within the Si/VO_2 waveguide design. Figure 4.8(c) and Figure 4.8(d) show the insertion loss and extinction ratio for both the fundamental TE and TM modes, respectively, comparing responses between the two proposed geometries. The solid lines show the performance of the geometry shown in Figure 4.8(a) while the data points represent performance of the geometry shown in Figure 4.8(b). Use of the geometry in Figure 4.8(b), which allows for mode regeneration, shows an increase in the extinction ratio for both the fundamental TE and TM modes. Specifically, the extinction ratio saturation is no longer observed for the fundamental TM mode for $L_{VO_2} \geq 100$ nm. There is a modest (< 1 dB) increase in insertion loss for the fundamental TM mode.

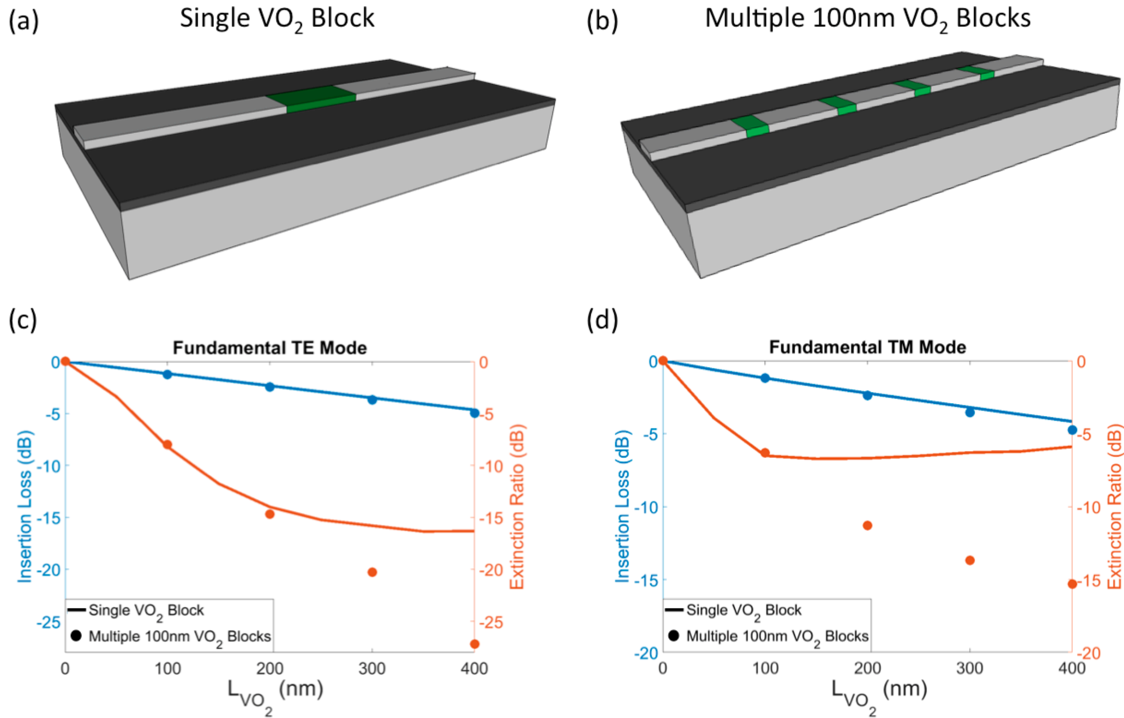

Figure 4.8. (a,b) Schematics of Si/VO_2 waveguide devices with (a) a single VO_2 embedded block of a given length and (b) multiple 100 nm long embedded VO_2 blocks spaced by 2 μm. VO_2, Si, and SiO_2 are green, light gray, and dark gray, respectively. (c,d) Insertion loss and extinction ratio comparison for waveguide geometries in (a) and (b) for the fundamental (c) TE and (d) TM optical modes.

Figure 4.8 serves to demonstrate the capability of mode regeneration and increased extinction ratios as a consequence. For high-speed applications, accessing the fast (~ 1-10 ps) transient recovery dynamics in VO_2 is achievable within a finite range of incident fluences, as shown in Figure 1.9. Therefore, incident pump fluences must be selected to ensure fluences only within this range are incident at each segment of VO_2. For example, in Ref. [51], the authors show a range of fluences from 0.28 to approximately 1.12 mJ/cm^2 give a fast (~ 10 ps) transient recovery [see Figure 1.9(b)]. Implementing the design shown in Figure 4.8(b), for an incident excitation fluence of 1.12 mJ/cm^2 and assuming the excitation pulse only interacts with semiconducting VO_2, simulation gives 44.3% transmission through the third segment of VO_2.

This corresponds to a fluence of 0.5 mJ/cm^2 incident at the fourth segment of VO_2, suggesting all four of the VO_2 segments would receive fluences which will access the ultrafast MST dynamics.

4.4 Conclusions

In this chapter, design considerations to push forward the practicality of both Si/VO_2 electro-optic and all-optical modulators were presented. Specifically for electro-optic modulation, a platform with simulated ~ 6 dB, broadband (~ 100 nm) extinction is proposed in a geometry with the potential to access the fastest electrically induced SMT and MST dynamics. For all-optical modulation, the expected performance of the device presented in Chapter 3 as an all-optical modulator with in-plane excitation was compared to other state-of-the-art all-optical modulators with in-plane excitation. Methods to improve device performance in response to TM light, in particular by modifying waveguide dimensions and understanding transient mode propagation, were also investigated.

Chapter 5

5. Conclusions and future avenues

5.1 Conclusions

The focus of this thesis has been to push forward the practicality of silicon-based modulators, both electro-optic and all-optical, that integrate vanadium dioxide (VO_2) for their active functionality. In Chapter 2, the first demonstration of electro-optic modulation of a patch of VO_2 atop a silicon ring resonator was presented. A tradeoff between extinction ratio and device response time was observed by examining rings with different VO_2 patch lengths and applied voltages. Using a 10 μm diameter silicon ring resonator with a VO_2 patch length of 1 μm, an extinction ratio of ~ 1.5 dB was measured with a response time of ~ 10 ns, matching the duration of the 2.5 V excitation voltage pulse. A broadband Si/VO_2 electro-absorption modulator design was also discussed; the design is comprised of a straight silicon waveguide with a 350 nm long patch of VO_2 on top, By selecting TM-polarized light and modifying the waveguide height accordingly, ~ 3 dB modulation was demonstrated using gold electrical contacts to resistively heat the structure. Since the VO_2 patch is almost entirely between the electrical contacts, this design may enable realization of faster temporal dynamics for electrically actuated switching of VO_2 by mitigating Joule heating of VO_2. In Chapter 3, Si/VO_2 photonic device platforms with potential implementation as all-optical modulators were presented. Specifically, a platform where VO_2 was embedded within a silicon waveguide, increasing modal interaction in comparison to a geometry where VO_2 is placed on top of the silicon waveguide, was explored. The experimental performance for varying lengths of VO_2 was presented using thermal initiation of the SMT of VO_2 via integrated resistive heaters. For an embedded VO_2 length of 500 nm, ~ 10 dB extinction was achieved. Projected implementation as an all-optical modulator with in-plane

excitation was discussed. In addition, a Si/VO_2 TM mode ring resonator was presented, demonstrating similar extinction ratio to a Si/VO_2 TE ring resonator with $1/10^{th}$ the VO_2 fractional coverage of the silicon ring as a result of using TM polarization. In addition, its projected implementation as an all-optical modulator with out-of-plane excitation was discussed. In Chapter 4, as a continuation of the demonstration of embedding VO_2 within a silicon waveguide in Chapter 3, a design for a TE mode Si/VO_2 electro-optic modulator was proposed where a small section of VO_2 was embedded within a silicon rib waveguide. Simulations suggest it can be implemented to improve device response times with sufficient extinction ratios (> 4 dB). In addition, the expected performance of the VO_2 embedded silicon waveguide as an all-optical modulator with in-plane excitation is compared with other state-of-the-art all-optical modulators. Detailed analysis of waveguide geometry and transient mode propagation through this structure was also analyzed, suggesting methods to increase device performance for all incident polarizations.

5.2 Future Avenues

While VO_2 has been studied for over half of a century, its implementation in silicon photonic structures has only been pursued within the last decade. This work pushes forward implementation of Si/VO_2 integrated photonic structures, but it is expected fabrication improvements and additional tuning of the optical properties will enable additional and improved functionalities. For example, demonstrations of atomic layer deposition of VO_2 [85-87] can likely be utilized in the VO_2 embedded silicon waveguide geometry proposed in Chapter 3 to successfully grow VO_2 in high aspect ratio trenches, allowing realization of the simulated optical performance shown in Figure 3.2(b). This method of successfully filling high aspect ratio

trenches can enable additional integrated photonic designs. For example, in Figure 5.1, a design idea is proposed for a Si/VO_2 all-optical ring resonator structure which could exhibit “fan-out” behavior, a necessary requirement of a proposed all-optical transistor [5], whereby a small input can provide an increase in device transmission. In this example design, using ALD, a patch of VO_2 (*e.g.*, 50 nm wide × 300 nm long × 220 nm tall) is embedded within a ring resonator. In the passive state, the VO_2 is semiconducting (shown in green) and an incident wavelength (shown in blue) resonant with the ring is selected, giving no transmission through the bus waveguide. By switching the VO_2 to the metallic phase (shown in purple) with an in-plane pump of the same wavelength, the resonance condition of the ring is changed, and the incident wavelength which is no longer resonant, is transmitted through the device.

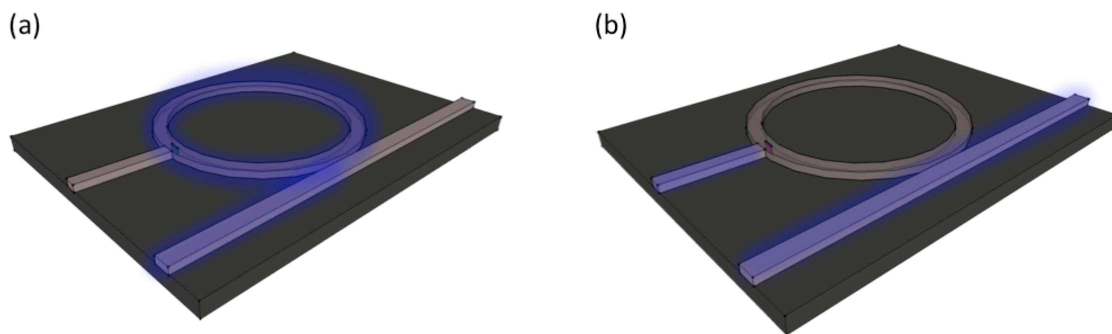

Figure 5.1. Proposed Si/VO_2 photonic device with potential implementation as an all-optical transistor, showing an embedded patch of VO_2 within a silicon ring resonator. (a) There is no incident pump on the VO_2 patch, leaving it in the semiconducting state (shown in green), and blue probe light is resonant, giving no transmission through the bus waveguide. (b) Pump light is incident, switching the VO_2 to its metallic state (shown in purple), and the blue probe light is no longer resonant, giving transmission through the bus waveguide.

Concerning tuning of the optical properties of VO_2, there has been extensive work focused on shifting the temperature of the SMT or tuning the optical properties of VO_2, particularly for smart window applications [88-90]. Specifically for integrated silicon photonic applications, explorations of reducing κ of semiconducting VO_2 would be instrumental in reducing insertion loss, especially for Si/VO_2 electro-optic devices. For all-optical devices with in-plane excitation, κ should be tuned appropriately to ensure the semiconducting VO_2 can be switched with incident radiation within the silicon waveguide. In addition, shifting the temperature of the SMT or using other vanadium oxide species could prove beneficial for use in low temperature or high temperature on-chip environments.

Appendix

A.1 Polarization in fiber-coupled optical setup

This section outlines the method used to control and characterize the polarization at the sample location for the fiber-coupled measurements presented in Chapter 2 and Chapter 3. Key components for control and characterization of the polarization are highlighted in Figure A.1. These are a linear polarizer (1), a half-wave plate (2), a fiber rotator (3), a polarization beam splitter cube (4), and a germanium photodetector (5). In general, the process is as follows. First, free-space polarization manipulation is achieved as light is coupled from the fiber into free-space (in the bottom right of Figure A.1), interacts with the linear polarizer (1) and half-wave plate (2), and is coupled into another fiber. Second, the polarization injected into the photonic devices is tuned via the positioning of the fiber rotator (3). The polarization beam splitter cube (4) transmits TE and reflects TM at 90°, so the polarization state is characterized by measuring the photocurrent generated in the germanium detector (5) when it is placed at 0° and 90° with respect to the beam path exiting the lensed tapered fiber. These steps are outlined in detail below.

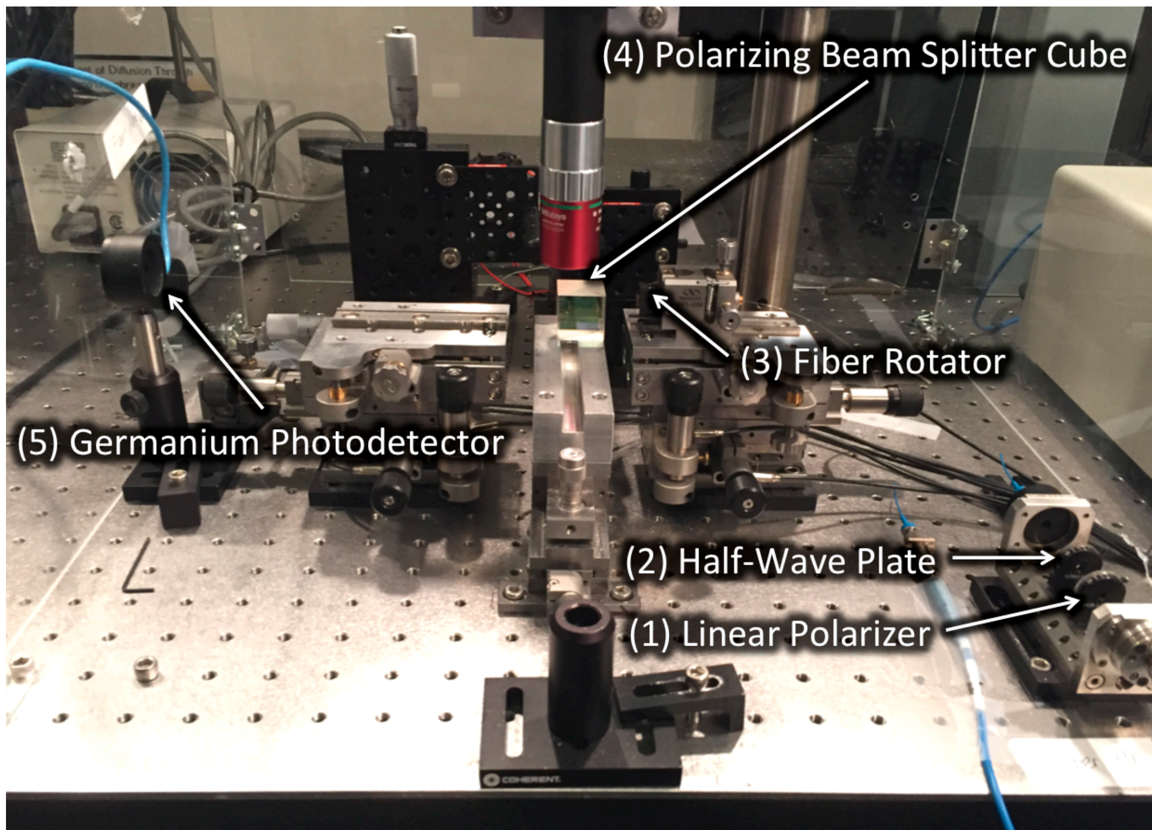

Figure A.1. Image of fiber-coupled optical setup showing components used for polarization control and characterization.

Figure A.2 shows a zoomed-in image of the area of free-space polarization control. The inset in the top right shows the entire setup, highlighting the zoomed-in area with a blue box. Tunable laser input (from a Santec TSL-510 in the current setup) is coupled from the fiber into free space. The linear polarizer serves to ensure the polarization is purely linear and should be rotated to maximize transmission of linearly polarized light. This can be done by removing the half-wave plate and measuring transmission through the linear polarizer with the germanium photodetector. In the current setup, this is achieved with the linear polarizer at an angle of 0°. This step can potentially be omitted since the laser light emitted is highly linearly polarized, but it is a useful step to ensure the light is linearly polarized and that the linear polarization is at 0° or 90°, as this

is helpful knowledge for use of the half-wave plate. The half-wave plate serves as the mechanism to switch between TE and TM operation of the photonic devices, as a half-wave plate at a 45° offset of the incident linear polarization will convert the linear polarization by 90°. Therefore, for measurements of integrated photonic devices, the two orientations of the half-wave plate should be (i) equal to the orientation of the linear polarizer and (ii) a 45° rotation in comparison to the orientation of the linear polarizer. For example, with the linear polarizer set to 0°, the half-wave plate should be set to 0° (or removed) and 45° for TE and TM measurements, or vice versa, depending on the fiber orientation, discussed in the following paragraph.

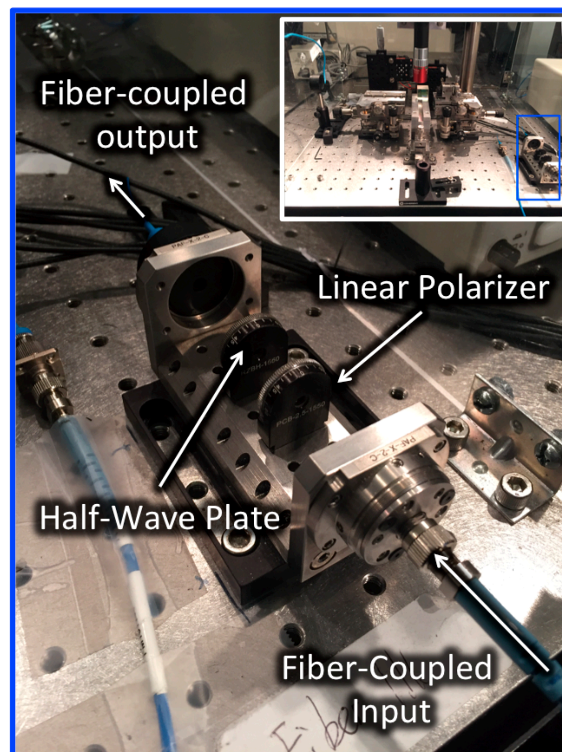

Figure A.2. Image showing free-space polarization control using a linear polarizer and half-wave plate. The top right inset shows the full fiber-coupled system, highlighting the region in this image with a blue box.

To this point, which half-wave plate orientation is associated with which polarization (*i.e.*, TE or TM) has not been defined. This is because the orientation of the polarization maintaining (meaning linear polarization is maintained as light propagates through the fiber) lensed tapered fiber, which is adjusted using the fiber rotator, determines the polarization injected into the photonic device. Figure A.3 shows a zoomed-in image of the area of the measurement setup that includes the fiber rotator, lensed tapered fiber, and polarization beam splitter cube (sitting on the stage where the photonic sample would be located). The inset in the top left shows the entire setup, highlighting the zoomed-in area with an orange box. With the linear polarizer and half-wave plate fixed (*e.g.*, linear polarizer at 0° and half-wave plate at 45°), the fiber should be rotated to maximize the intensity of light for either TE or TM polarization. To do this, the fiber should be placed close to the edge of the polarization beam splitter cube. Care should be taken to avoid damaging the fiber tip and polarization beam splitter cube. After ensuring the fiber rotator is fastened tightly to the copper casing holding the fiber, the copper casing should be loosened from the Newport 561-GM fiber chuck positioner. This can be achieved by lightly unscrewing the screw securing it at the top of the fiber chuck positioner.

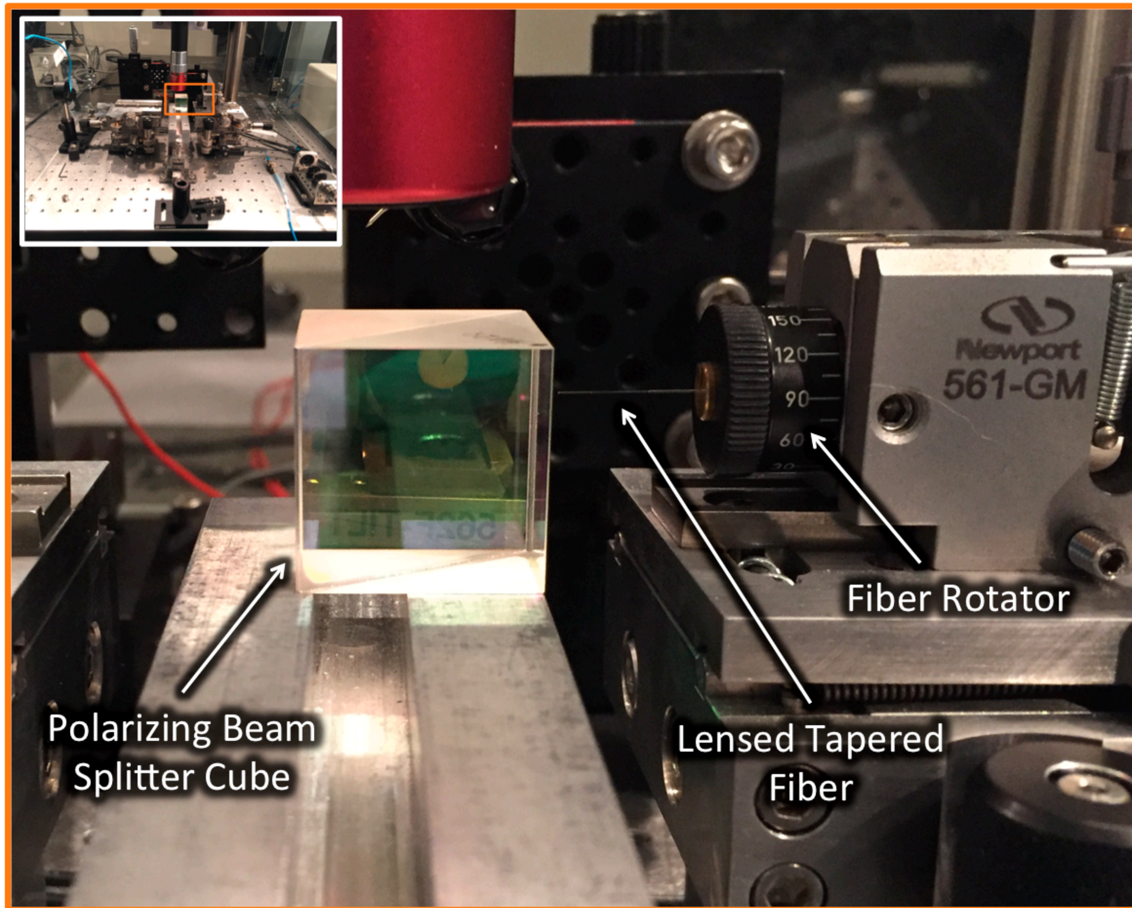

Figure A.3. Image of lensed tapered fiber adjacent to the polarization beam splitter cube. The fiber rotator shown controls the orientation of the fiber and therefore the polarization incident on a photonic sample during measurement. The top left inset shows the full fiber-coupled system, highlighting the region in this image with an orange box.

To characterize the polarization, the transmitted power through or the reflected power (at 90°) off the polarization beam splitter cube should be monitored with the germanium photodetector while rotating the fiber orientation. Figure A.4 shows the germanium photodetector in these two positions [*i.e.*, parallel to the direction of the optical fiber in Figure A.4(a) and 90° relative to the direction of the optical fiber in Figure A.4(b)] and includes cartoon schematics of how light incident on the polarization beam splitter cube will be transmitted and

reflected. As mentioned before, the cube transmits TE (shown in red in Figure A.4) and reflects TM (shown in yellow in Figure A.4) at 90°. With the germanium photodetector in one position, the detector should be adjusted in the two dimensions perpendicular to the beam propagation direction to achieve maximum photocurrent. Once maximized, the fiber should be rotated to maximize transmission for the desired polarization (determined by where the germanium detector is located). Periodically after rotating the fiber, it should be verified the germanium detector is still positioned in a location that maximizes photocurrent. As an example, to get TE polarization (*e.g.*, with the linear polarizer at 0° and half-wave plate at 45°), the fiber should be rotated to get maximum photocurrent with the germanium detector at 0° (measuring light transmitted through the polarization beam splitter cube). To verify the result, this process can be repeated with the linear polarizer at 0° and half-wave plate at 0° (or removed), and photocurrent for the germanium detector at 90° (measuring light reflected at 90° off the polarization beam splitter cube) should read a maximum for the same fiber orientation. The same process can also be used to verify minimum transmissions are achieved for the opposite polarizations, and this method can be used to characterize the polarization purity if the spacing between the germanium detector and the polarization beam splitter cube is made to be identical for the two cases shown in Figure A.4.

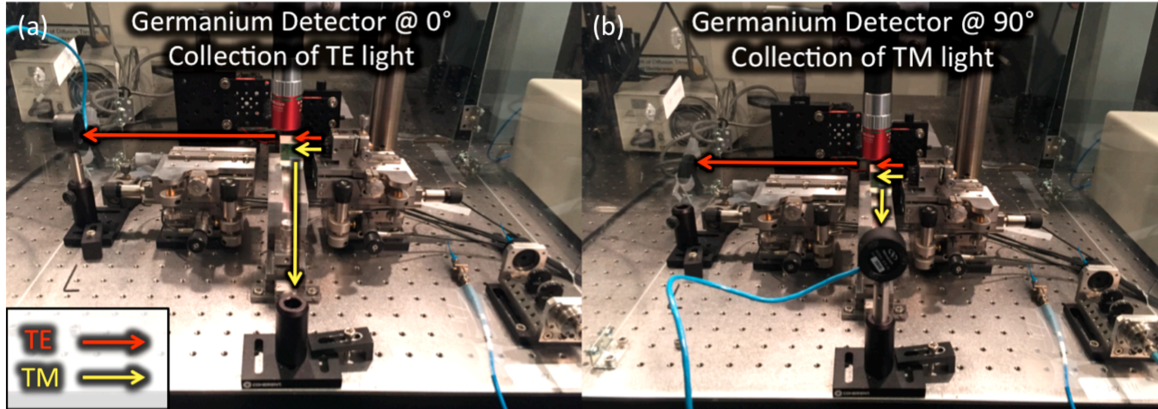

Figure A.4. Images of the fiber-coupled setup with the germanium detector in locations for TE (parallel to the direction of the optical fiber, shown in the left image) and TM (90° to the direction of the optical fiber, shown in the right image) polarizations. TE and TM polarizations are shown in red and yellow, respectively.

REFERENCES

1. "First telegraphic message - 24 May 1844." (Library of Congress), retrieved November 19, 2016, http://www.loc.gov/item/mmorse000107/.

2. K. C. Kao and G. A. Hockham, "Dielectric-fibre surface waveguides for optical frequencies," P. I. Electr. Eng. **113**, 1151-1158 (1966).

3. "Submarine Cable Map - Telegeography", retrieved February 6, 2018, http://www.submarinecablemap.com/?__hstc=267387025.af2ca993ee0df3a8bf0996f8d2c5f36b.1517948475830.1517948475830.1517948475830.1&__hssc=267387025.1.1517948475830&__hsfp=2425394384&hsCtaTracking=08aaced5-c258-44c7-908e-42cfc3efaf46%7Cffa04223-12df-4896-8360-72483f3291f5.

4. D. A. B. Miller, "Device Requirements for Optical Interconnects to Silicon Chips," Proc. IEEE **97**, 1166-1185 (2009).

5. D. A. B. Miller, "Are optical transistors the logical next step?," Nat. Photonics **4**, 3-5 (2010).

6. M. Wuttig, H. Bhaskaran, and T. Taubner, "Phase-change materials for non-volatile photonic applications," Nat. Photonics **11**, 465 (2017).

7. E. Kuramochi and M. Notomi, "Phase-change memory," Nat. Photonics **9**, 712 (2015).

8. K. K. Lee, D. R. Lim, H.-C. Luan, A. Agarwal, J. Foresi, and L. C. Kimerling, "Effect of size and roughness on light transmission in a Si/SiO_2 waveguide: Experiments and model," Appl. Phys. Lett. **77**, 1617-1619 (2000).
9. D. Liang and J. E. Bowers, "Recent progress in lasers on silicon," Nat. Photonics **4**, 511-517 (2010).

10. G. T. Reed, G. Mashanovich, F. Y. Gardes, and D. J. Thomson, "Silicon optical modulators," Nat. Photonics **4**, 518-526 (2010).

11. X. Gan, R.-J. Shiue, Y. Gao, I. Meric, T. F. Heinz, K. Shepard, J. Hone, S. Assefa, and D. Englund, "Chip-integrated ultrafast graphene photodetector with high responsivity," Nat. Photonics **7**, 883-887 (2013).

12. D. Feng, S. Liao, P. Dong, N.-N. Feng, H. Liang, D. Zheng, C.-C. Kung, J. Fong, R. Shafiiha, J. Cunningham, A. V. Krishnamoorthy, and M. Asghari, "High-speed Ge photodetector monolithically integrated with large cross-section silicon-on-insulator waveguide," Appl. Phys. Lett. **95**, 261105 (2009).

13. Q. Xu, B. Schmidt, S. Pradhan, and M. Lipson, "Micrometre-scale silicon electro-optic modulator," Nature **435**, 325-327 (2005).

14. D. Feng, S. Liao, H. Liang, J. Fong, B. Bijlani, R. Shafiiha, B. J. Luff, Y. Luo, J. Cunningham, A. V. Krishnamoorthy, and M. Asghari, "High speed GeSi electro-absorption modulator at 1550 nm wavelength on SOI waveguide," Opt. Express **20**, 22224-22232 (2012).

15. R. A. Soref and B. R. Bennett, "Electrooptical effects in silicon," IEEE J. Quantum Elect. **23**, 123-129 (1987).

16. A. Liu, R. Jones, L. Liao, D. Samara-Rubio, D. Rubin, O. Cohen, R. Nicolaescu, and M. Paniccia, "A high-speed silicon optical modulator based on a metal–oxide–semiconductor capacitor," Nature **427**, 615 (2004).

17. G. T. Reed, G. Z. Mashanovich, F. Y. Gardes, M. Nedeljkovic, Y. Hu, D. J. Thomson, K. Li, P. R. Wilson, S.-W. Chen, and S. S. Hsu, "Recent breakthroughs in carrier depletion based silicon optical modulators," Nanophotonics **3**, 229 (2014).

18. P. Dong, L. Chen, and Y.-k. Chen, "High-speed low-voltage single-drive push-pull silicon Mach-Zehnder modulators," Opt. Express **20**, 6163-6169 (2012).

19. M. Streshinsky, R. Ding, Y. Liu, A. Novack, Y. Yang, Y. Ma, X. Tu, E. K. S. Chee, A. E.-J. Lim, P. G.-Q. Lo, T. Baehr-Jones, and M. Hochberg, "Low power 50 Gb/s silicon traveling wave Mach-Zehnder modulator near 1300 nm," Opt. Express **21**, 30350-30357 (2013).

20. X. Xi, L. Xianyao, X. Hao, H. Yingtao, X. Kang, L. Zhiyong, C. Tao, Y. Jinzhong, and Y. Yude, "44-Gb/s silicon microring modulators based on zigzag pn junctions," IEEE Photonic Tech. L. **24**, 1712-1714 (2012).

21. Y. Jiang, W. Jiang, L. Gu, X. Chen, and R. T. Chen, "80-micron interaction length silicon photonic crystal waveguide modulator," Appl. Phys. Lett. **87**, 221105 (2005).

22. E. Timurdogan, C. M. Sorace-Agaskar, J. Sun, E. Shah Hosseini, A. Biberman, and M. R. Watts, "An ultralow power athermal silicon modulator," Nat. Comm. **5**, 4008 (2014).

23. T. Tanabe, M. Notomi, S. Mitsugi, A. Shinya, and E. Kuramochi, "All-optical switches on a silicon chip realized using photonic crystal nanocavities," Appl. Phys. Lett. **87**, 151112 (2005).

24. C. Haffner, W. Heni, Y. Fedoryshyn, J. Niegemann, A. Melikyan, D. L. Elder, B. Baeuerle, Y. Salamin, A. Josten, U. Koch, C. Hoessbacher, F. Ducry, L. Juchli, A. Emboras, D. Hillerkuss, M. Kohl, L. R. Dalton, C. Hafner, and J. Leuthold, "All-plasmonic mach–zehnder modulator enabling optical high-speed communication at the microscale," Nat. Photonics **9**, 525-528 (2015).

25. L. Alloatti, R. Palmer, S. Diebold, K. P. Pahl, B. Chen, R. Dinu, M. Fournier, J.-M. Fedeli, T. Zwick, W. Freude, C. Koos, and J. Leuthold, "100 GHz silicon-organic hybrid modulator," Light-Sci. Appl. **3**, e173 (2014).

26. D. Korn, R. Palmer, H. Yu, P. C. Schindler, L. Alloatti, M. Baier, R. Schmogrow, W. Bogaerts, S. K. Selvaraja, G. Lepage, M. Pantouvaki, J. M. D. Wouters, P. Verheyen, J. Van Campenhout, B. Chen, R. Baets, P. Absil, R. Dinu, C. Koos, W. Freude, and J. Leuthold, "Silicon-organic hybrid (SOH) IQ modulator using the linear electro-optic effect for transmitting 16QAM at 112 Gbit/s," Opt. Express **21**, 13219-13227 (2013).

27. S. Koeber, R. Palmer, M. Lauermann, W. Heni, D. L. Elder, D. Korn, M. Woessner, L. Alloatti, S. Koenig, P. C. Schindler, H. Yu, W. Bogaerts, L. R. Dalton, W. Freude, J. Leuthold, and C. Koos, "Femtojoule electro-optic modulation using a silicon-organic hybrid device," Light-Sci. Appl. **4**, e255 (2015).

28. A. V. Krishnamoorthy, X. Zheng, D. Feng, J. Lexau, J. F. Buckwalter, H. D. Thacker, F. Liu, Y. Luo, E. Chang, P. Amberg, I. Shubin, S. S. Djordjevic, J. H. Lee, S. Lin, H. Liang, A. Abed, R. Shafiiha, K. Raj, R. Ho, M. Asghari, and J. E. Cunningham, "A low-power, high-speed, 9-channel germanium-silicon electro-absorption modulator array integrated with digital CMOS driver and wavelength multiplexer," Opt. Express **22**, 12289-12295 (2014).

29. P. Chaisakul, D. Marris-Morini, M.-S. Rouifed, G. Isella, D. Chrastina, J. Frigerio, X. Le Roux, S. Edmond, J.-R. Coudevylle, and L. Vivien, "23 GHz Ge/SiGe multiple quantum well electro-absorption modulator," Opt. Express **20**, 3219-3224 (2012).

30. Y. Hu, M. Pantouvaki, J. Van Campenhout, S. Brems, I. Asselberghs, C. Huyghebaert, P. Absil, and D. Van Thourhout, "Broadband 10 Gb/s operation of graphene electro-absorption modulator on silicon," Laser Photonics Rev. **10**, 307-316 (2016).

31. C. T. Phare, Y.-H. Daniel Lee, J. Cardenas, and M. Lipson, "Graphene electro-optic modulator with 30 GHz bandwidth," Nat. Photonics **9**, 511-514 (2015).

32. M. Liu, X. Yin, E. Ulin-Avila, B. Geng, T. Zentgraf, L. Ju, F. Wang, and X. Zhang, "A graphene-based broadband optical modulator," Nature **474**, 64-67 (2011).

33. V. J. Sorger, N. D. Lanzillotti-Kimura, R.-M. Ma, and X. Zhang, "Ultra-compact silicon nanophotonic modulator with broadband response," Nanophotonics **1**, 17 (2012).

34. N. Youngblood, Y. Anugrah, R. Ma, S. J. Koester, and M. Li, "Multifunctional graphene optical modulator and photodetector integrated on silicon waveguides," Nano Lett. **14**, 2741-2746 (2014).

35. C. Koos, P. Vorreau, T. Vallaitis, P. Dumon, W. Bogaerts, R. Baets, B. Esembeson, I. Biaggio, T. Michinobu, F. Diederich, W. Freude, and J. Leuthold, "All-optical high-speed

signal processing with silicon-organic hybrid slot waveguides," Nat. Photonics **3**, 216-219 (2009).

36. K. Nozaki, T. Tanabe, A. Shinya, S. Matsuo, T. Sato, H. Taniyama, and M. Notomi, "Sub-femtojoule all-optical switching using a photonic-crystal nanocavity," Nat. Photonics **4**, 477-483 (2010).

37. W. Bogaerts, P. De Heyn, T. Van Vaerenbergh, K. De Vos, S. Kumar Selvaraja, T. Claes, P. Dumon, P. Bienstman, D. Van Thourhout, and R. Baets, "Silicon microring resonators," Laser Photonics Rev. **6**, 47-73 (2012).

38. M. Imada, A. Fujimori, and Y. Tokura, "Metal-insulator transitions," Rev. Mod. Phys. **70**, 1039-1263 (1998).

39. S. Raoux and M. Wuttig, *Phase Change Materials: Science and Applications* (Springer US, 2009).

40. Z. Yang, C. Ko, and S. Ramanathan, "Oxide electronics utilizing ultrafast metal-insulator transitions," Annu. Rev. Mater. Res. **41**, 337-367 (2011).

41. D. Lencer, M. Salinga, B. Grabowski, T. Hickel, J. Neugebauer, and M. Wuttig, "A map for phase-change materials," Nat. Mater. **7**, 972 (2008).

42. F. J. Morin, "Oxides which show a metal-to-insulator transition at the Neel temperature," Phys. Rev. Lett. **3**, 34-36 (1959).

43. J. B. Kana Kana, J. M. Ndjaka, G. Vignaud, A. Gibaud, and M. Maaza, "Thermally tunable optical constants of vanadium dioxide thin films measured by spectroscopic ellipsometry," Opt. Commun. **284**, 807-812 (2011).

44. T. L. Cocker, L. V. Titova, S. Fourmaux, G. Holloway, H. C. Bandulet, D. Brassard, J. C. Kieffer, M. A. El Khakani, and F. A. Hegmann, "Phase diagram of the ultrafast photoinduced insulator-metal transition in vanadium dioxide," Phys. Rev. B **85**, 155120 (2012).

45. H. T. Kim, Y. W. Lee, B. J. Kim, B. G. Chae, S. J. Yun, K. Y. Kang, K. J. Han, K. J. Yee, and Y. S. Lim, "Monoclinic and correlated metal phase in VO_2 as evidence of the Mott transition: coherent phonon analysis," Phys. Rev. Lett. **97**, 266401 (2006).

46. A. Pashkin, C. Kübler, H. Ehrke, R. Lopez, A. Halabica, R. F. Haglund, R. Huber, and A. Leitenstorfer, "Ultrafast insulator-metal phase transition in VO_2 studied by multiterahertz spectroscopy," Phys. Rev. B **83**, 195120 (2011).

47. Z. Tao, T. R. T. Han, S. D. Mahanti, P. M. Duxbury, F. Yuan, C. Y. Ruan, K. Wang, and J. Wu, "Decoupling of structural and electronic phase transitions in VO_2," Phys. Rev. Lett. **109**, 166406 (2012).

48. S. Wall, D. Wegkamp, L. Foglia, K. Appavoo, J. Nag, R. F. Haglund, J. Stähler, and M. Wolf, "Ultrafast changes in lattice symmetry probed by coherent phonons," Nat. Comm. **3**, 721 (2012).

49. V. R. Morrison, R. P. Chatelain, K. L. Tiwari, A. Hendaoui, A. Bruhács, M. Chaker, and B. J. Siwick, "A photoinduced metal-like phase of monoclinic VO_2 revealed by ultrafast electron diffraction," Science **346**, 445-448 (2014).

50. D. Wegkamp, M. Herzog, L. Xian, M. Gatti, P. Cudazzo, C. L. McGahan, R. E. Marvel, R. F. Haglund, Jr., A. Rubio, M. Wolf, and J. Stähler, "Instantaneous band gap collapse in photoexcited monoclinic VO_2 due to photocarrier doping," Phys. Rev. Lett. **113**, 216401 (2014).

51. N. F. Brady, K. Appavoo, M. Seo, J. Nag, R. P. Prasankumar, R. F. Haglund, and D. J. Hilton, "Heterogeneous nucleation and growth dynamics in the light-induced phase transition in vanadium dioxide," J. Phys-Condens. Mat. **28**, 125603 (2016).

52. P. Markov, R. E. Marvel, H. J. Conley, K. J. Miller, R. F. Haglund, and S. M. Weiss, "Optically monitored electrical switching in VO_2," ACS Photonics **2**, 1175-1182 (2015).

53. Z. You, C. Xiaonan, K. Changhyun, Y. Zheng, C. Mouli, and S. Ramanathan, "Voltage-triggered ultrafast phase transition in vanadium dioxide switches," IEEE Electr. Device L. **34**, 220-222 (2013).

54. R. M. Briggs, I. M. Pryce, and H. A. Atwater, "Compact silicon photonic waveguide modulator based on the vanadium dioxide metal-insulator phase transition," Opt. Express **18**, 11192-11201 (2010).

55. J. Nag, J. D. Ryckman, M. T. Hertkorn, B. K. Choi, R. F. Haglund, and S. M. Weiss, "Ultrafast compact silicon-based ring resonator modulators using metal-insulator switching of vanadium dioxide," in *SPIE OPTO*, (SPIE, 2010), 759710.

56. J. D. Ryckman, V. Diez-Blanco, J. Nag, R. E. Marvel, B. K. Choi, R. F. Haglund, and S. M. Weiss, "Photothermal optical modulation of ultra-compact hybrid Si-VO_2 ring resonators," Opt. Express **20**, 13215-13225 (2012).

57. L. Sánchez, S. Lechago, A. Gutierrez, and P. Sanchis, "Analysis and design optimization of a hybrid VO_2/silicon 2x2 microring switch," IEEE Photonics J. **8**, 1-9 (2016).

58. L. Sánchez, S. Lechago, and P. Sanchis, "Ultra-compact TE and TM pass polarizers based on vanadium dioxide on silicon," Opt. Lett. **40**, 1452-1455 (2015).

59. A. Joushaghani, J. Jeong, S. Paradis, D. Alain, J. Stewart Aitchison, and J. K. S. Poon, "Wavelength-size hybrid Si-VO_2 waveguide electroabsorption optical switches and photodetectors," Opt. Express **23**, 3657-3668 (2015).

60. J. T. Kim, "CMOS-compatible hybrid plasmonic modulator based on vanadium dioxide insulator-metal phase transition," Opt. Lett. **39**, 3997-4000 (2014).

61. J. H. Choe and J. T. Kim, "Design of vanadium dioxide-based plasmonic modulator for both TE and TM modes," IEEE Photonic Tech. L. **27**, 514-517 (2015).

62. B. Janjan, M. Miri, A. Zarifkar, and M. Heidari, "Design and simulation of compact optical modulators and switches based on Si-VO_2-Si horizontal slot waveguides," J. Lightwave Technol. **35**, 3020-3028 (2017).

63. P. Markov, K. Appavoo, R. F. Haglund, and S. M. Weiss, "Hybrid Si-VO_2-Au optical modulator based on near-field plasmonic coupling," Opt. Express **23**, 6878-6887 (2015).

64. J. D. Ryckman, K. A. Hallman, R. E. Marvel, R. F. Haglund, and S. M. Weiss, "Ultra-compact silicon photonic devices reconfigured by an optically induced semiconductor-to-metal transition," Opt. Express **21**, 10753-10763 (2013).

65. J. K. Clark, Y. L. Ho, H. Matsui, and J. J. Delaunay, "Optically pumped hybrid plasmonic-photonic waveguide modulator using the VO_2 metal-insulator phase transition," IEEE Photonics J. **10**, 1-9 (2018).

66. D. A. Miller, "Physical reasons for optical interconnection," Int. J. Optoelectron. **11**, 155-168 (1997).

67. K. J. Miller, P. Markov, R. E. Marvel, R. F. Haglund, and S. M. Weiss, "Hybrid silicon-vanadium dioxide electro-optic modulators," in *SPIE OPTO*, (SPIE, 2016), 975203-975207.

68. J. Leroy, A. Crunteanu, A. Bessaudou, F. Cosset, C. Champeaux, and J.-C. Orlianges, "High-speed metal-insulator transition in vanadium dioxide films induced by an electrical pulsed voltage over nano-gap electrodes," Appl. Phys. Lett. **100**, 213507 (2012).

69. S. Cueff, D. Li, Y. Zhou, F. J. Wong, J. A. Kurvits, S. Ramanathan, and R. Zia, "Dynamic control of light emission faster than the lifetime limit using VO_2 phase-change," Nat. Comm. **6**, 8636 (2015).

70. T. Barwicz, M. R. Watts, M. A. Popović, P. T. Rakich, L. Socci, F. X. Kärtner, E. P. Ippen, and H. I. Smith, "Polarization-transparent microphotonic devices in the strong confinement limit," Nat. Photonics **1**, 57 (2006).

71. Z. Li, M.-H. Kim, C. Wang, Z. Han, S. Shrestha, A. C. Overvig, M. Lu, A. Stein, A. M. Agarwal, M. Lončar, and N. Yu, "Controlling propagation and coupling of waveguide modes using phase-gradient metasurfaces," Nat. Nanotechnol. **12**, 675-683 (2017).

72. M. Rini, Z. Hao, R. W. Schoenlein, C. Giannetti, F. Parmigiani, S. Fourmaux, J. C. Kieffer, A. Fujimori, M. Onoda, S. Wall, and A. Cavalleri, "Optical switching in VO_2 films by below-gap excitation," Appl. Phys. Lett. **92**, 181904 (2008).

73. E. D. Palik, *Handbook of Optical Constants of Solids* (Academic Press, 1998).

74. K. J. Miller, K. A. Hallman, R. F. Haglund, and S. M. Weiss, "Silicon waveguide optical switch with embedded phase change material," Opt. Express **25**, 26527-26536 (2017).

75. K. J. Miller, K. A. Hallman, R. F. Haglund, and S. M. Weiss, "Optical modulation in silicon-vanadium dioxide photonic structures," in *SPIE Nanoscience + Engineering*, (SPIE, 2017), 103451D.

76. Y. Ikuma, Y. Shoji, M. Kuwahara, X. Wang, K. Kintaka, H. Kawashima, D. Tanaka, and H. Tsuda, "Small-sized optical gate switch using $Ge_2Sb_2Te_5$ phase-change material integrated with silicon waveguide," Electron. Lett. **46**, 368-369 (2010).

77. Y. Zhang, J. Li, J. Chou, Z. Fang, A. Yadav, H. Lin, Q. Du, J. Michon, Z. Han, Y. Huang, H. Zheng, T. Gu, V. Liberman, K. Richardson, and J. Hu, "Broadband transparent optical phase change materials," in *Conference on Lasers and Electro-Optics*, OSA Technical Digest (online) (Optical Society of America, 2017), JTh5C.4.

78. P. B. Johnson and R. W. Christy, "Optical constants of the noble metals," Phys. Rev. B. **6**, 4370-4379 (1972).

79. N. D. Arora, J. R. Hauser, and D. J. Roulston, "Electron and hole mobilities in silicon as a function of concentration and temperature," IEEE T. Electron Dev. **29**, 292-295 (1982).

80. J. F. Shackelford and W. Alexander, *CRC materials science and engineering handbook. Third edition* (CRC Press, 1999).

81. C. Husko, A. De Rossi, S. Combrié, Q. V. Tran, F. Raineri, and C. W. Wong, "Ultrafast all-optical modulation in GaAs photonic crystal cavities," Appl. Phys. Lett. **94**, 021111 (2009).

82. A. Martínez, J. Blasco, P. Sanchis, J. V. Galán, J. García-Rupérez, E. Jordana, P. Gautier, Y. Lebour, S. Hernández, R. Spano, R. Guider, N. Daldosso, B. Garrido, J. M. Fedeli, L. Pavesi, and J. Martí, "Ultrafast all-optical switching in a silicon-nanocrystal-based silicon slot waveguide at telecom wavelengths," Nano Lett. **10**, 1506-1511 (2010).

83. S. Hu and S. M. Weiss, "Design of photonic crystal cavities for extreme light concentration," ACS Photonics **3**, 1647-1653 (2016).

84. Z. Cheng, C. Ríos, W. H. P. Pernice, C. D. Wright, and H. Bhaskaran, "On-chip photonic synapse," Sci. Adv. **3**(2017).

85. M. Currie, M. A. Mastro, and V. D. Wheeler, "Characterizing the tunable refractive index of vanadium dioxide," Opt. Mater. Express **7**, 1697-1707 (2017).

86. A. P. Peter, K. Martens, G. Rampelberg, M. Toeller, J. M. Ablett, J. Meersschaut, D. Cuypers, A. Franquet, C. Detavernier, J.-P. Rueff, M. Schaekers, S. Van Elshocht, M. Jurczak, C. Adelmann, and I. P. Radu, "Metal-Insulator Transition in ALD VO_2 Ultrathin Films and Nanoparticles: Morphological Control," Adv. Funct. Mater. **25**, 679-686 (2015).

87. I. M. Povey, M. Bardosova, F. Chalvet, M. E. Pemble, and H. M. Yates, "Atomic layer deposition for the fabrication of 3D photonic crystals structures: Growth of Al_2O_3 and VO_2 photonic crystal systems," Surf. Coat. Tech. **201**, 9345-9348 (2007).

88. L. Xingxing, W. Shao-Wei, C. Feiliang, Y. Liming, and C. Xiaoshuang, "Tuning phase transition temperature of VO_2 thin films by annealing atmosphere," J. Phys. D. Appl. Phys. **48**, 265104 (2015).

89. A. Romanyuk, R. Steiner, L. Marot, and P. Oelhafen, "Temperature-induced metal–semiconductor transition in W-doped VO_2 films studied by photoelectron spectroscopy," Sol. Energ. Mat. Sol. C. **91**, 1831-1835 (2007).

90. S. Y. Li, G. A. Niklasson, and C. G. Granqvist, "Nanothermochromics: Calculations for VO_2 nanoparticles in dielectric hosts show much improved luminous transmittance and solar energy transmittance modulation," J. Appl. Phys. **108**, 063525 (2010).